

# Optical Potentials for the Realization of Dissipative Fermi-Hubbard Models with Ultracold Ytterbium Atoms

Dissertation

zur Erlangung des Doktorgrades  
des Department Physik  
der Universität Hamburg

vorgelegt von

Bastian Hundt

aus Hamburg

Hamburg

2016

## **Gutachter**

Gutachter der Dissertation:	Prof. Dr. Klaus Sengstock Prof. Dr. Andreas Hemmerich
Gutachter der Disputation:	Prof. Dr. Markus Drescher Prof. Dr. Andreas Hemmerich Prof. Dr. Ludwig Mathey Prof. Dr. Henning Moritz Prof. Dr. Klaus Sengstock
Datum der Disputation:	08. November 2016
Vorsitzender der Prüfungskommission:	Prof. Dr. Ludwig Mathey
Vorsitzender des Promotionsausschusses:	Prof. Dr. Wolfgang Hansen
Dekan der Fakultät für Mathematik, Informatik und Naturwissenschaften:	Prof. Dr. Heinrich Graener

## **Erklärung zur Eigenständigkeit**

Hiermit erkläre ich an Eides statt, dass ich die vorliegende Dissertationsschrift selbst verfasst und keine anderen als die angegebenen Quellen und Hilfsmittel benutzt habe.

*Bastian Hundt*

*Hamburg – 31.08.2016*

# Abstract

Quantum gases of Alkaline-Earth like (AEL) atoms like Ytterbium provide novel and intricate new features which make them particularly interesting for the investigation of quantum many-body physics. Their rich level structure gives rise to long-lived meta-stable states and the possibility to create state-selective optical lattice potentials. Ytterbium is a particular well-suited species because it offers all benefits of AELs including multiple stable fermionic as well as bosonic isotopes.

In this thesis, the setup of a quantum gas machine capable of producing ultracold samples of different isotopes of Ytterbium is presented. A new bichromatic, three beams optical dipole trap which realizes deep initial trapping with high trap frequencies, while still able to create an ultracold sample with low average trap frequencies of  $\bar{\omega} = 2\pi \times 36$  Hz is implemented. Pure Bose-Einstein condensates with up to  $N = 2 \cdot 10^5$  and degenerate Fermi gases with six spin components with up to  $1 \cdot 10^5$  atoms at  $T/T_F = 0.18$  are realized.

For the study of strongly correlated many-body systems a new optical lattice setup is presented which consists of two substructures: a one-dimensional lattice used for addressing the meta-stable state and a two-dimensional lattice formed by three interfering laser beams creating a triangular lattice structure. The lattice is operated at the magic wavelength thereby suppressing intensity dependent broadening and shifting of the clock transition. The beam shaping optics of the lattice are carefully characterized and found to provide a very homogeneous phase front with phase front deviations significantly below  $\Delta\phi = \lambda/4$ . Parametric heating, as well as lattice modulation spectroscopy, is used to determine the depth of the lattice.

A new scheme based on a rapid-adiabatic passage on the meta-stable state transition allows efficient and reliable meta-stable state preparation. Due to two-body losses a significant difference in the adiabatic passage particle number dynamics for a spin polarized fermionic sample and a sample consisting of atoms in six spin-states is found. The polarized gas shows a high transfer efficiency while the spin state mixture shows a particle number dependent efficiency loss. This loss is explained in terms of doubly occupied lattice sites and compared to the theoretical ground state atomic distribution. To independently detect the number of excited state atoms a new detection system for the meta stable state atoms based on a repumping is implemented.

By loading atoms in the meta-stable state into 1D-lattice tubes a dissipative Fermi-Hubbard model is realized. By observing the time evolution of the particle number for a spin mixture a significant deviation from a simple two-body loss model is observed. This is attributed to an effective decrease in nearest neighbor particle correlation function  $g^{(2)}$  on the order of a factor of five.

The here presented quantum gas machine and the developed techniques for preparation and detection of excited state Ytterbium atoms is an ideal starting point for the investigation of strongly correlated quantum many-body models and the study of dissipative Fermi-Hubbard systems.



# Zusammenfassung

Quantengase aus Erdalkali-ähnlichen Atomen, wie z.B. Ytterbium, besitzen komplexe atomare Eigenschaften. Sie sind hervorragend geeignet, neuartige quanten viel-teilchen Systeme zu untersuchen. Die komplexe Energie-Niveau Struktur führt zu metastabilen Zuständen und der Möglichkeit zustandsabhängige Optische Gitter zu erzeugen.

Diese Arbeit beschäftigt sich mit der Erzeugung und Untersuchung von Ytterbium Quantengasen, sowohl fermionischer als auch bosonischer Spezies. Dafür wird neben dem Aufbau zur Kühlung von kalten Ytterbium-Gasen insbesondere die optische Dipolfalle beschrieben. Diese Falle erlaubt das effiziente fangen der Atome aus der Magneto-Optischen-Falle während gleichzeitig niedrige mittlere Fallenfrequenzen von  $\bar{\omega} = 2\pi \times 36 \text{ Hz}$  realisiert werden. Mit dieser Falle werden Bose-Einstein Kondensate mit  $N = 2 \cdot 10^5$  Teilchen und Entartete Fermi-Gase mit bis zu  $1 \cdot 10^5$  bei einer Temperatur von  $T/T_F = 0.18$  erzeugt.

Das neu aufgebaute optische Gitter besteht aus zwei Substrukturen: ein ein-dimensionales Gitter welches insbesondere zur Anregung des metastabilen Zustands benötigt wird, sowie ein zwei-dimensionales welches aus drei interferierenden Strahlen besteht und eine dreieckige oder heaxagonale Gitterstruktur erzeugt. Das Gitter wird durch einen Laser erzeugt der nahe der magischen Wellenlänge operiert. Dies unterdrückt Intensitäts abhängige verschiebung und verbreiterung des ultraschmalen optischen Übergangs. Die Phasenfronten die von der Strahlformungsoptik für das Gitter mit dreieckiger Struktur erzeugt werden, werden mittels eines Interferometrischen Aufbaus untersucht und Verzerrungen kleiner  $\Delta\phi = \lambda/4$  ermittelt. Parametrisches Heizen als auch Gitter Modulations Spektroskopie wird genutzt um die Gittertiefe zu bestimmen.

Die Erzeugung von Ytterbium Gasen im Metastabilen Zustand ist ein zentrales anliegen dieser Arbeit. Dazu wurde ein neues Verfahren entwickelt, welches auf einem schnellen adiabatischen Transfer mittels des optischen Übergangs in den Metastabilen Zustand realisiert wurde. Durch Zwei-Körper Verluste wird ein signifikanter unterschied in der Transfereffizienz zwischen einem Spin-Polarisierten Gas und einer Spin-Mischung festgestellt. Dieser Unterschied wird durch doppelt besetzte Gitterplätze erklärt. Die experimentellen Daten passen qualitativ gut zu einem theoretischen Grundzustandsdichte-Modell. Um die Teilchenzahl im angeregten Zustand zu bestimmen wurde ein neues Detektions-System für die metastabilen Atome auf Basis eines Rückpumpers entwickelt und charakterisiert.

Durch das Laden von metastabilen Atomen in ein ein-dimensionales optisches Gitter und unter Ausnutzung der Zweikörper-Verluste, wird ein dissipatives Fermi-Hubbard Modell untersucht. Die beobachtete Teilchenzahldynamik einer Spin-Mischung weicht deutlich von einem einfach Zwei-Körper-Verlustmodell ab. Dies wird durch eine Abnahme der nächsten-nachbarn Korrelations-Funktion  $g^{(2)}$  um einen Faktor fünf erklärt.

Der hier dargestellte experimentelle Aufbau zum Realisieren von ultrakalten Ytterbium Gasen sowie die entwickelten Methoden zur Erzeugung und Detektion von Gasen aus metastabilen Ytterbium Atomen sind ein idealer Ausgangspunkt um stark korrelierte Quanten Viel-Teilchen Systeme und dissipative Fermi-Hubbard modelle zu untersuchen.

# Contents

<b>1. Introduction</b>	<b>1</b>
<b>2. A Short Ytterbium Introduction</b>	<b>7</b>
2.1. General Ytterbium Properties and Isotopes . . . . .	7
2.2. Optical Transitions and their Properties . . . . .	8
2.2.1. Broad Blue Transition . . . . .	9
2.2.2. Narrow Green Intercombination-Transition . . . . .	10
2.2.3. Ultranarrow Clock-Transition . . . . .	10
2.3. Properties of Ground- and Excited-State . . . . .	11
2.3.1. Magnetic Properties . . . . .	11
2.3.2. Scattering Properties . . . . .	12
2.3.3. Polarizabilities . . . . .	15
2.4. Conclusion . . . . .	16
<b>3. Degenerate Quantum Gases of Yb</b>	<b>17</b>
3.1. Laser Cooling and General Experimental Setup . . . . .	18
3.1.1. Vacuum System and Laser Cooling . . . . .	19
3.1.2. Detection . . . . .	20
3.1.3. 2D- & 3D-Magneto Optical Trap Performance . . . . .	21
3.2. Bichromatic Dipole Trap Setup . . . . .	22
3.2.1. Fundamental Relations . . . . .	23
3.2.2. Design Considerations for the Bichromatic Dipole Trap . . . . .	25
3.2.3. Beam Alignment and Evaporation Scheme . . . . .	27
3.3. Bose-Einstein Condensation with the Bichromatic Dipole Trap . . . . .	28
3.3.1. Temperature and Particle Number during the Evaporation . . . . .	28
3.3.2. Trap Frequency Measurement . . . . .	31
3.3.3. Lifetime . . . . .	32
3.4. Ultracold Fermi Gases . . . . .	33
3.4.1. Spin Preparation and Spin Detection . . . . .	33
3.4.2. Degenerate Fermi Gas . . . . .	34
3.5. Conclusion . . . . .	35

<b>4. A Magic Optical Lattice for Yb</b>	<b>37</b>
4.1. Design of the Optical Lattice	37
4.1.1. Geometry	38
4.1.2. Wavelength and Laser	40
4.1.3. Achievable Lattice Depth, Trap Frequencies, and Recoil Suppression	40
4.1.4. Final Design	41
4.2. Laser System	42
4.3. Beam Shaping Optics	44
4.3.1. 1D-Beam Shaping	44
4.3.2. 2D-Beam Shaping	46
4.4. Integration and Characterization of the Optical Lattice	48
4.4.1. Beam Alignment and Polarization	50
4.4.2. Momentum Distribution of Bosons and Fermions out of the 2D-lattice	50
4.4.3. Lattice Depth Calibration	51
4.4.4. Characterization of the Fiber Noise Cancellation System	54
4.5. Conclusion	56
<b>5. Excited State Preparation and Detection</b>	<b>59</b>
5.1. Addressing the Clock-State	60
5.1.1. High-Finesse Resonator and High-Bandwidth Control Loop	60
5.1.2. Switching-Setup and Frequency-Sweeping	62
5.2. Excited State Detection	63
5.2.1. Repumping Setup	64
5.2.2. Imaging sequence	65
5.2.3. Repumper Efficiency	65
5.3. Rapid Adiabatic Passage on Clock Transition	66
5.3.1. Principle of Adiabatic Passages	66
5.3.2. Experimental RAP Sequence	69
5.3.3. RAP using a Polarized Gas	70
5.3.4. RAP using a Spin-Mixture	71
5.3.5. Differential Rabi Frequencies	72
5.3.6. Influence of Double-Occupancies on the RAP	73
5.3.7. Initial Higher-Band Population	77
5.3.8. Summary of Spin Mixture RAP	77
5.4. RAP for the Study of the Kondo Lattice Model	78
5.4.1. Broadening of the Clock Transition in a Non-Magic Lattice	78
5.4.2. Experimental Parameters for a RAP in the Non-Magic Optical Lattice	80
5.5. Summary	80
<b>6. Dissipative Dynamics with Ultracold <math>^{173}\text{Yb}</math></b>	<b>81</b>
6.1. Dissipative 1D-Fermi-Hubbard Model	82
6.1.1. Theoretical Description of Open Quantum Systems	82



6.1.2.	Effective Loss-Rate and Rate-Equation . . . . .	83
6.1.3.	Mott-Insulator vs. Zeno-Insulator . . . . .	86
6.2.	Experimental Realization of a Dissipative-Fermi Hubbard Model . . . . .	86
6.2.1.	Experimental Procedure . . . . .	87
6.2.2.	Lifetime of a Polarized-Fermi-Gas in the Excited-State . . . . .	88
6.2.3.	Lifetime of Spin-Mixtures in Shallow 1D-Lattices . . . . .	92
6.2.4.	Data Analysis . . . . .	92
6.2.5.	Discussion . . . . .	97
6.3.	Possibility of Loss-Measurements as a Probe for the Initial State . . . . .	98
6.4.	Summary . . . . .	99
<b>7.</b>	<b>Summary and Outlook</b>	<b>101</b>
<b>A.</b>	<b>Comparison of Lifetime Models</b>	<b>103</b>
<b>B.</b>	<b>Rapid Adiabatic Passage Interaction Hamiltonian</b>	<b>107</b>
	<b>Bibliography</b>	<b>109</b>



# 1. Introduction

One of the major challenges in physics is the understanding and description of interacting quantum many-body systems. Even though the fundamental interactions of atoms among each other are well understood, physical systems consisting of a large amounts of atoms embedded in complex spatial structures are very difficult to describe because of the exponential growth of the Hilbert space [1]. This holds especially true for the case of strong interactions where static as well as dynamical properties are heavily influenced by correlations. A prime example of this are high-temperature superconductors whose behavior is attributed to strong correlations [2]. Heavy-Fermion materials are another example of a solid-state material where the emerging macroscopic behavior is attributed to correlations and interactions [3]. One path to mitigate the problem of growing complexity is reducing the studied systems to its fundamental building blocks. The continuous development of new tools and techniques to exert control over the quantum state and search for new ways of extracting informations about the correlations of the system is a major effort undertaken by experimental and theoretical physicists around the world.

One very successful approach to study quantum many-body systems in great detail is the field of ultracold quantum gases. When such a gas is loaded into an optical lattice [4, 5], these systems provide a reliable and highly controllable structure which allows the realization of a simplified, yet powerful and important model of solid-state systems: the Hubbard-model [6]. This model incorporates the fundamental processes which are present in solid-state materials, namely inter-atomic interactions and tunneling from one lattice site to the next. When this is realized in a quantum gas experiment with bosonic atoms, the result is a simulation of the Bose-Hubbard model. Within this model, the Mott-insulator state was realized and the associated phase transition detected [7]. The implementation of the Fermi-Hubbard model followed shortly thereafter [8, 9] and provided another fundamental cornerstone for the simulation of complex materials by adding the additional complexity of Fermi-Dirac statistics.

Since these experimental milestones, a lot of experimental work has been performed to increase the understanding and control of these systems. The single-site resolved detection of atoms in optical lattices for bosons [10, 11] and recently fermions [12–15] opened up not only new possibilities to observe dynamics but enabled completely new ways for quantum state engineering [16]. These advances lead to the detection of anti-ferromagnetic correlations in a Fermi-Hubbard model [17] and the study of entanglement in many-body systems [18] to name only a few very recent examples.

Another similarly successful route to simulate more complex, but still easily controllable artificial materials is the implementation of driven and non-cubic lattice structures [19–21]. The non-cubic structure not only creates intricate ground state band structures but is most often accompanied with the possibility to fundamentally alter the band structure and ground state by lattice shaking techniques. These techniques opened up the possibilities to study topological bands and even access the Berry curvature [22] with momentum resolution [23]. The emulation of artificial gauge fields and the simulation of an Ising-XY spin model [24] or the observation of chiral superfluidity [25] are equally impressive demonstrations of the versatility of driven or non-cubic optical lattices.

A third actively pursued direction in expanding the possibilities of quantum gas experiments is the use of atoms with new atomic properties. Besides atoms with a large dipole moment like Erbium [26] or Dysprosium [27] a prominent example of this effort is the trapping and cooling of Ytterbium which was pioneered by the Kyoto group [28] and is now pursued in different research facilities around the world. Alkaline-earth like (AEL) atoms like Ytterbium but also Strontium [29] and Calcium [30] have two outer electrons which lead to the existence of long-lived meta-stable electronic states. This allows AELs to be used as a reference oscillator for the most stable optical lattice clock in the world [31]. Further, the meta-stable states allow the implementation of model systems with additional orbital degrees of freedom, one of the most prominent being the Kondo-Lattice model (KLM) [32, 33]. The KLM describes a system of mobile and immobile spins on a lattice which interacts via a spin-exchange interaction [34, 35]. Heavy fermion materials are expected to be described by the KLM. These materials are characterized by a huge increase in electron mass and show a variety of exotic ground state phases governed by correlations [3]. Using a state-selective lattice producing a shallow trapping potential for ground state and a deep optical lattice of the meta-stable excited state atoms the KLM can be realized using a Ytterbium quantum gas. These are only two examples of the huge success and potential of quantum gases consisting of Ytterbium atoms. The prediction and observation of a novel kind of orbital Feshbach resonances [36–38], realized spin-orbit-coupling [39, 40], the possibility to realize quadrupole interactions [41], the observation of chiral edge states [42] and schemes for implementing quantum computation [43] are further examples for the versatility of an AEL atom like Ytterbium in the context of quantum many-body physics.

The realization and success of quantum gases as a means to study complex many-body phenomena was largely enabled by the large degree of control and strong decoupling from the environment. While the decoupling is absolutely necessary to realize a quantum gas, decoherence and dissipative processes are a fundamental aspect of real-world quantum systems. The understanding of decoherence, particle loss and in general the influence of a *bath* coupled to a quantum system on the buildup or destruction of correlations is not only of interest for fundamental research but has very practical purposes in the fields of quantum information processing and quantum cryptography [44–46]. In the context of quantum gases in optical lattices, most often dissipation is present in some form of particle loss. The rate at which a loss occurs can influence the dynamics of the studied system heavily. Two-body

losses, which occur when two atoms occupy the same lattice site, are a type of loss which is highly correlated because it occurs only when two atoms interact with each other. The loss acts as a continuous measurement of the double occupancy of a lattice site. Due to the quantum Zeno effect [47, 48] this can lead to a suppression of tunneling to occupied lattice sites. The strength of this suppression depends on the loss-rate, tunneling rate and elastic interaction strength. A scenario with strong two-body losses in an optical lattice was studied experimentally in [49] and theoretically in [50]. In these studies, bosonic molecules are loaded into 1D-lattices and allowed to tunnel. These molecules possess a strong two-body onsite loss-rate. From the time evolution of the number of particles, the creation of a highly correlated many-body state was deduced. A comparable experiment using fermionic molecules was performed in [51] and theoretically discussed in [52]. The experiment used the loss measurement to determine a filling fraction of the atoms in the optical lattice while theoretical studies revealed the importance of multiband calculations when the loss-rate is large. The crossover from the weak to strong measurement regime was observed in [53]. Using photo-association of atom pairs the two-body loss rate could be tuned over a wide range and an effective localization of atoms in the strong measurement regime was observed. Quantum Zeno-like dynamics can also be observed by a single particle loss. This path was taken by an experiment using a *scanning electron microscope* (SEM) [54]. This setup used an electron beam and its superior spatial resolution to induce a localized loss in a BEC and the onset of Quantum-Zeno dynamics could be observed. Recently the creation of a highly entangled many-body state through dissipation was proposed when an AEL atom is loaded into 1D-lattice tubes [55] and it was theoretically shown how dissipation can be used for quantum state engineering [56]. These experimental realizations, as well as the proposed experiments, show the huge opportunities for studying fundamental questions in quantum many-body physics with dissipative interactions.

In this thesis two of the frontiers outlined above are addressed: a quantum gas machine capable of producing ultracold samples of bosonic as well as fermionic Ytterbium samples is realized and a non-cubic lattice with a triangular or honeycomb structure. Additionally, a new preparation scheme to create ultracold samples of excited state atoms based on a rapid adiabatic passage is presented. These ingredients are then combined to study a dissipative Fermi-Hubbard model which allows the observation of a reduction in the nearest-neighbor correlation function  $g^{(2)}$ .

## Structure of this Thesis

The thesis begins with a short introduction to the most important properties of Ytterbium in chapter 2. The focus lies on the features most relevant for the remainder of the text. The quantum gas machine itself is based on the all-optical creation of Ytterbium Bose-Einstein condensates (BEC) or degenerate Fermi gases (DFG) using a three-beam optical dipole trap. The dipole trap is loaded directly from a Magneto-Optical trap (MOT). The setup

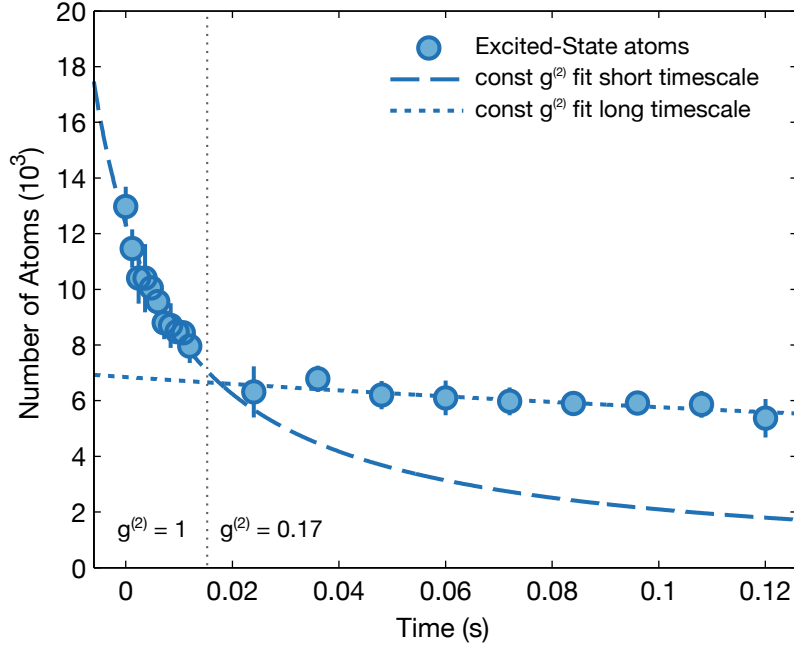


**Figure 1.1.** | Lifetime of a two-spin  $^{173}\text{Yb}$  mixture in  $6E_R$  deep 1D-lattice tubes. Shown is a lifetime measurements for a two-spin state mixture with loss-rate fits for short and long times of the data. The fits show two-particle losses  $N(t) \sim N^2$  with constant nearest-neighbor correlation function  $g^{(2)}$  for short and long timescales.

used to create and detect quantum gases is the focus of chapter 3. A previous dipole trap setup [57, 58] was able to create ultracold samples of Ytterbium but had the drawback of high average trap frequencies. The new setup based on two distinct evaporation phases with three different trapping beams reduces the trap frequencies by almost a factor of three. The new evaporation scheme is characterized in terms of phase-space density and evaporation efficiency as well as lifetime and trap frequency measurements. The new dipole trap is an ideal starting point for loading atoms in the optical lattice which will be the focus of chapter 4. This chapter presents the implementation of a non-cubic, triangular lattice and the control of the lattice depth. A major concern while setting up the lattice system was the quality of the beam shaping optics and thus is an important topic of this chapter. In chapter 5 the optical lattice and a fermionic Ytterbium quantum gas is used to develop and characterize a preparation method to create fermionic Ytterbium samples in the meta-stable state. The method is based on a rapid adiabatic passage (RAP) using the ultranarrow *clock* transition which allows highly stable and repeatable creation of meta-stable Ytterbium samples. In particular, the difference between samples consisting of atoms in one spin-state and samples consisting of atoms in more than one spin-state will be discussed in

depth. Further, a new detection system for direct atom counting of atoms in the excited-state is presented. Chapter 6 bridges all topics discussed in the chapters before. Here a Fermi-Hubbard model in 1D-lattice-tubes with a dissipative component is realized. The dissipation is the result of two-body losses between interacting atoms in the meta-stable state. A typical lifetime measurement for a sample consisting of atoms in two different spin-states in this system is shown in figure 1.1. From this measurement, it already can be seen that distinctive timescales are present in the data and a simple two-body loss rate equation model is not enough to capture the observed dynamics. The reduction in loss-rate is attributed to a decrease in nearest-neighbor particle correlations as will be discussed in the chapter. Chapter 7 summarizes the experimental results obtained in this thesis and will show future research possibilities along the lines of the loss-measurements presented here but also in terms of the possibility to implement the KLM.

## Publication

### Publikationen

Im Rahmen der vorliegenden Arbeit ist die folgende wissenschaftliche Veröffentlichung entstanden.

### Publications

The following research article has been published in the course of this thesis.

- [P1] S. Dörscher, A. Thobe, B. Hundt, A. Kochanke, R. LeTargat, P. Windpassinger, C. Becker, and K. Sengstock, *Creation of quantum-degenerate gases of ytterbium in a compact 2D-/3D-magneto-optical trap setup*, *Review of Scientific Instruments* **84**, 043109 (2013)



## 2. A Short Ytterbium Introduction

In recent years *alkaline earth like* (AEL) atoms attracted a lot of attention in the field of ultracold quantum gases. Their rich level structure, governed by two electrons in the outermost shell, open up new and exciting possibilities for metrological as well as quantum many-body research. This chapter serves as an introduction as well as a reference for the most important atomic properties of Yb, focussing on the aspects relevant to this thesis. For more and complementary information see e.g. [57–60].

Starting with a general introduction to Ytterbium in section 2.1 the remainder of this chapter focusses on optical transitions and their properties (section 2.2) as well as the magnetic and scattering properties of the two most relevant atomic states (section 2.3).

### 2.1. General Ytterbium Properties and Isotopes

Ytterbium belongs to the group of *Alkaline-Earth-like* (AEL) atoms with completely filled inner shells and two outer s-shell electrons. The two s-shell electrons not only allow Ytterbium to be used as an optical clock but gives rise to many fascinating, in terms of quantum gases new and sometimes limiting atomic properties, like state-selective trapping potentials [61], *optical Feshbach resonances* [62] or strong two-body losses.

In terms of ultracold quantum gases and laser cooling, the properties of AEL atoms are governed by the low lying energy states. In the  $^1S_0$  (also labeled  $|g\rangle$ ) ground state the two valence electrons form a spin-singlet with total spin  $S = 0$ . Transitions to and from the ground state which changes the spin state are electric-dipole forbidden ( $\Delta S = 0$  selection rule) and thus suppressed. This gives rise to a Helium-like structure. Transitions which change from a spin-singlet into a spin-triplet are called *intercombination*-transitions. Because of perturbations of pure *LS*-coupling (Russel-Saunders coupling) a small admixing of allowed states (especially the dipole allowed transition to  $^1P_1$ ) opens up the possibility for transitions into the  $^3P_{0,1,2}$  manifold [63] ( $^3P_0$  also labeled  $|e\rangle$  and called *excited state* or clock state). The Helium-like splitting into singlet and triplet-states gives rise to one of the most interesting features of Ytterbium which is the existence of narrow-linewidth states allowing e.g. efficient cooling and trapping in a magneto-optical trap (MOT) and to transfer atoms into states which can be regarded as stable on experimental timescales. These states can be used as another degree of freedom in the system. A sketch of the transitions discussed

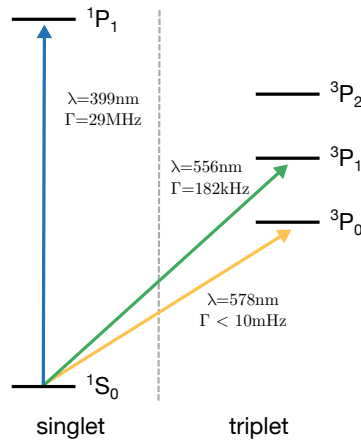


**Figure 2.1. | Lowest lying energy levels and optical transitions of Ytterbium.** Shown are the lowest energy levels of Ytterbium and the most relevant optical transitions. The level structure is governed by a Helium-like splitting in spin-singlet and spin-triplet states. Intercombination transitions connecting singlet- and triplet-states are suppressed as indicated by their narrow linewidth. The states  $3P_{0,2}$  are called clock states because of their long lifetime in the multiple second regime. The transition into the  $3P_2$  state is omitted here.

here is shown in figure 2.1. There exists a multitude of other transitions which are omitted here. Some of them will be discussed in the course of this thesis when needed.

Beside the existence of long-lived meta-stable excited states a second striking feature of Ytterbium is the existence of seven radiative stable isotopes. Two of these isotopes are fermions and five are bosons. All of them are naturally available but with significantly different abundances. All stable isotopes with their percentage of abundance and nuclear spin are shown in table 2.1.

From these seven isotopes, Bose-Einstein condensation (BEC) has first been achieved by the Kyoto group using  $^{174}\text{Yb}$  [65].  $^{174}\text{Yb}$  has very favorable properties regarding abundance (see table 2.1) and scattering properties (discussed below) which make it an ideal choice for the production of bosonic Ytterbium quantum gases. Next a degenerate Fermi-gas (DFG) of  $^{173}\text{Yb}$  was reported [66]. Most other isotopes have been cooled to degeneracy and various isotope mixtures were realized [67, 68].

## 2.2. Optical Transitions and their Properties

In the following the optical transitions and their properties in terms of laser-cooling and their usage in the experimental cycle are discussed.

$A$	Abundance (%)	$I$	Statistic
168	0.12	0	boson
170	2.98	0	boson
171	14.09	1/2	fermion
172	21.68	0	boson
173	16.10	5/2	fermion
174	32.03	0	boson
176	13.00	0	boson

**Table 2.1. | Ytterbium isotopes and their natural abundance.** This table lists all stable isotopes of Ytterbium. Shown is their atomic mass number, relative abundance, total nuclear spin and whether the isotope is a fermion or boson. Data taken from [64].

### 2.2.1. Broad Blue Transition

The 399 nm blue transition connects the  $^1S_0$  and the  $^1P_1$  spin-singlet state. The transition is dipole allowed which results in a broad linewidth of [69]

$$\Gamma_{399\text{nm}} = 2\pi \times 29 \text{ MHz}. \quad (2.1)$$

This large linewidth (approx. a factor of five larger compared to the Rubidium  $D1$  or  $D2$  transition [70]) results in a high Doppler temperature [71] of

$$T_D = \frac{\hbar\Gamma_{399\text{nm}}}{2k_B} \approx 696 \mu\text{K}. \quad (2.2)$$

The large linewidth allows efficient capture of thermal atoms. The blue transition is thus a very well suited candidate for precapture and precooling of atoms with a thermal velocity distribution, e.g. cooling in a 2D-MOT or slowing an atomic beam from an atomic oven in a Zeeman-slower configuration. Additionally the  $^1S_0 \rightarrow ^1P_1$  transition is well suited for absorption imaging of atomic clouds [72]. Typical imaging laser systems have linewidths of few 100 kHz which is two orders of magnitude smaller than the natural linewidths of the blue transitions making the imaging somewhat insensitive to frequency fluctuations. Additionally, the large linewidth results in a high saturation intensity of  $I_{\text{sat}} \approx 60 \text{ mW/cm}^2$  and thus the low-intensity regime for absorption imaging is easily reached.

All bosonic isotopes of Ytterbium have  $F = 0$  in the ground state and  $F' = 1$  in the  $^1P_1$  state. This means that there is only one transition  $F = 0 \rightarrow F' = 1$  available for cooling. For the fermionic isotope  $^{173}\text{Yb}$   $F = 5/2$  and in the  $^1P_1$  state  $F' = 7/2$ ,  $F' = 5/2$  and  $F' = 3/2$ . Cooling is typically performed on the  $F = 5/2 \rightarrow F' = 7/2$  transition. Details of the transitions, energy shift etc. can be found in [57, 58].

For the bosonic isotopes with  $F = 0$  Subdoppler-cooling is not possible and thus the Doppler-temperature is the limit in achievable cooling performance.  $700 \mu\text{K}$  is too hot

for starting an efficient evaporative cooling and thus another optical transition is needed for achieving a colder temperature for efficient transfer from a MOT into the dipole trap.

### 2.2.2. Narrow Green Intercombination-Transition

The green intercombination transition  $^1S_0 \rightarrow ^3P_1$  is the solution to the problem of the high Doppler-temperature of the blue transition.

For pure  $LS$ -coupling transitions with  $\Delta S \neq 0$  are electric-dipole forbidden [73] and thus no transitions between  $^1S_0$  and  $^3P_1$  should exist. However in the case of heavy nuclei the spin-orbit interaction can not be treated as a perturbation to the  $LS$ -coupling scheme [73, p. 88]. The state  $^3P_1$  is in reality a mixture of the pure  $LS$ -states  $^3P_1^0$  and  $^1P_1^0$  [63]. The pure state  $^1P_1^0$  is electric-dipole coupled to the ground-state and thus a small coupling between  $^1S_0$  and  $^3P_1$  exists. See the aforementioned references and [59] for details. This coupling is still small resulting in a narrow linewidth of [74]

$$\Gamma_{556\text{nm}} = 2\pi \times 182 \text{ kHz}. \quad (2.3)$$

This linewidth corresponds to a Doppler-temperature of

$$T_D = \frac{\hbar\Gamma_{556\text{nm}}}{2k_B} \approx 4.4\mu\text{K}. \quad (2.4)$$

This temperature is again a limit for atoms without magnetic substructure as for the bosonic Ytterbium isotopes. The narrow linewidth allows creating cool samples which can be loaded and evaporatively cooled in e.g. optical dipole traps. It is thus very well suited as a second cooling stage after precooling on the broad blue transition.

### 2.2.3. Ultranarrow Clock-Transition

For the physics to be studied with Ytterbium the clock transition is arguably the most important optical transition. The transition from the ground state to the clock state  $^3P_0$  in  $LS$ -coupling is doubly forbidden ( $\Delta S = 0$  and  $J = 0 \not\leftrightarrow J' = 0$ ).

The spin-orbit interaction weakens the selection rule  $\Delta S = 0$  as before but  $J = 0 \not\leftrightarrow J' = 0$  is still valid. This can only be circumvented by hyperfine interactions effectively coupling  $^3P_0$  to  $^1S_0$  [63]. Because only the fermionic isotopes have a nuclear spin only the fermions have a small but finite transition probability and thus only with  $^{173}\text{Yb}$  or  $^{171}\text{Yb}$  a direct excitation of the clock transition is possible. To transfer atoms into  $^3P_0$  in one of the bosonic isotopes a technique called *magnetic field-induced spectroscopy* [75] can be employed. The linewidth of  $^{173}\text{Yb}$  and  $^{171}\text{Yb}$  was determined to [76]

$$\Gamma_{578\text{nm}} < 10 \text{ mHz}. \quad (2.5)$$

As for the ground-state, the electronic angular momentum  $J$  is zero.

## 2.3. Properties of Ground- and Excited-State

For the creation of ultracold gases of Ytterbium and for the study of many-body dynamics the elastic and inelastic scattering properties of Ytterbium are very important. Together with the magnetic properties of the ground and excited state, they are discussed in this section.

### 2.3.1. Magnetic Properties

$^1S_0$  as well as the  $^3P_0$  have both electronic angular momentum of  $J = 0$ . The total angular momentum is therefore given by the nuclear spin  $I$ . In the case of the bosonic isotopes  $I = 0$ . The fermions possess a nuclear spin ( $I = 5/2$  and  $I = 1/2$  respectively) so the atoms are susceptible to external magnetic fields. The *Zeeman-effect* shifts the energy  $E$  of a atomic level in a magnetic field  $B$  according to [77]:

$$\Delta E_Z = g_F \mu_B m_F B \quad (2.6)$$

with  $m_F$  being the Hyperfine substate and  $\mu_B$  the Bohr-magneton.  $g_F$  is the Landé-factor which in the case of  $J = 0$  is

$$g_F = \frac{\mu_N}{\mu_B} g_I \quad (2.7)$$

where  $\mu_N$  is the nuclear magneton and  $g_I$  is the nuclear Landé-factor. The nuclear-magneton is approximately 1800 times smaller compared to the Bohr-magneton and thus the sensitivity to magnetic fields is suppressed accordingly. As a downside, this means that practically magnetic trapping of all isotopes of Ytterbium is very difficult because of the large magnetic fields needed. Furthermore, a spatial separation of atoms in different spin-states during time-of-flight (TOF) using magnetic gradients is also impractical (*Stern-Gerlach* separation). On the upside, the insensitive to magnetic fields allows high precision metrology applications where insensitivity to external stray fields is paramount.

**Differential Zeeman Shift** In principle, both states  $^1S_0$  and  $^3P_0$  should be equally sensitive to magnetic fields. However due to the mixing of other states into  $^3P_0$  as discussed in the previous chapter the excited-state has a slightly different nuclear Landé-factor. This results in a *differential Zeeman shift* between the two states. The two states have Zeeman shifts of [78]:

$$\begin{aligned} \Delta E_{Z,|g\rangle} &\approx -207.15 \text{ Hz/G} \times m_f B \\ \Delta E_{Z,|e\rangle} &\approx -93.77 \text{ Hz/G} \times m_f B \end{aligned} \quad (2.8)$$

and with this numbers a total differential Zeeman shift of:

$$\delta_Z = 113.4 \text{ Hz/G} \times m_f B \quad (2.9)$$

Isotope	$^{168}\text{Yb}$	$^{170}\text{Yb}$	$^{171}\text{Yb}$	$^{172}\text{Yb}$	$^{173}\text{Yb}$	$^{174}\text{Yb}$	$^{176}\text{Yb}$
$^{168}\text{Yb}$	252	117	89	65	38	2	-358
$^{170}\text{Yb}$		64	36	-2	-81	-517	209
$^{171}\text{Yb}$			-3	-8	-577	428	141
$^{172}\text{Yb}$				-598	417	200	106
$^{173}\text{Yb}$					199	138	80
$^{174}\text{Yb}$						105	54
$^{176}\text{Yb}$							-24

**Table 2.2. | Scattering lengths between all Yb isotopes in the ground state.** Given are the elastic s-wave scattering lengths between all combinations of Yb isotopes in the  $^1\text{S}_0$  in units of  $a_0$ . Data from [80].

### 2.3.2. Scattering Properties

#### Elastic Scattering

At low enough temperatures (below  $\sim \mu\text{K}$  [79]) collisions between atoms are governed by s-wave scattering which is characterized by the sign and the magnitude of the *s-wave scattering length*  $a$ . The scattering length  $a$  for Ytterbium atoms in the  $^1\text{S}_0$  or  $^3\text{P}_0$  state is independent of the particular nuclear spin setting. Furthermore, the spin states are conserved during elastic scattering events. This can be seen when considering the direct coupling of the nuclear spins between two colliding atoms is expected to be extremely weak [32]. The only way a collision could change the nuclear spin is via the electronic cloud. Both states  $^1\text{S}_0$  and  $^3\text{P}_0$  have no net electronic angular momentum and therefore the nuclear spin does not couple to the electronic cloud [32]. Therefore collisions between atoms in the  $^1\text{S}_0$  and/or  $^3\text{P}_0$  state conserve the nuclear spin setting during scattering events. The spin conserving interaction between  $|g\rangle \leftrightarrow |g\rangle$ ,  $|e\rangle \leftrightarrow |e\rangle$  and  $|g\rangle \leftrightarrow |e\rangle$  atoms is said to be  $\text{SU}(N)$  symmetric (with  $N$  the number of spin states) and it is predicted that this symmetry leads to novel magnetic phases [32]. The ground state scattering lengths between all Ytterbium isotopes have been measured and are presented in table 2.2.

Notably the intraspecies scattering lengths of  $^{173}\text{Yb}$  and  $^{174}\text{Yb}$  are very well suited for direct evaporative cooling (compare with the  $^{87}\text{Rb}$  s-wave scattering lengths of about  $100a_0$  [81] which is known for efficient evaporative cooling). Due to the almost vanishing scattering length for  $^{171}\text{Yb}$  it is not possible to perform homo-nuclear evaporative cooling. However sympathetic cooling with  $^{173}\text{Yb}$  is possible [68] and thus opens up the possibility to study systems with negligible atom-atom interactions which will become relevant in the future as discussed in chapter 6.

Note that while the scattering lengths are independent of  $m_f$  they are dependent on the

Isotope	$^{173}\text{Yb}$	$^{171}\text{Yb}$
$a_{gg}$	199	-3
$a_{ee}$	306	-
$a_{eg}^+$	3300	-25
$a_{eg}^-$	220	-

**Table 2.3. | Scattering lengths for the fermionic isotopes.** Given are the elastic s-wave scattering lengths for both fermionic isotopes for scattering between ground- and excited-states. Data given in  $a_0$ . Table from [59] with data from [34, 35, 80, 82].

electronic state of the atoms. Beside  $|g\rangle \leftrightarrow |g\rangle$  and  $|e\rangle \leftrightarrow |e\rangle$  the symmetric as well as anti-symmetric collision channels between  $|g\rangle \leftrightarrow |e\rangle$  need to be taken into account. This leads to four different scattering lengths:

$$\begin{aligned}
|gg\rangle \otimes |s\rangle &\rightarrow a_{gg} \\
|ee\rangle \otimes |s\rangle &\rightarrow a_{ee} \\
(|eg\rangle + |ge\rangle) \otimes |s\rangle &\rightarrow a_{eg}^+ \\
(|eg\rangle - |ge\rangle) \otimes |t\rangle &\rightarrow a_{eg}^-
\end{aligned} \tag{2.10}$$

Here  $|s\rangle$  labels the spin-singlet state and  $|t\rangle$  labels the spin-triplet and are included to correctly anti-symmetrize the wavefunction. The four scattering lengths have been measured for  $^{173}\text{Yb}$  but are only partially known for  $^{171}\text{Yb}$ . The known values are presented in table 2.3. Note the vastly different scattering lengths for  $a_{eg}^+$  and  $a_{eg}^-$  which is a result of the particular molecular potential of  $^{173}\text{Yb}$ .

### Inelastic Scattering

While the  $^3\text{P}_0$  state has long radiative lifetimes it is not the energetic ground state of the atom. Interactions with other atoms can induce relaxation processes. During these collisions, the energy stored in the atom is released and converted to kinetic energy [83, 84] while the atoms undergo transitions into the  $^1\text{S}_0$  state. Typically the energy released is so large that the atoms are lost from all trapping potentials. The details of these collisions are complicated and depend on the molecular potential of the involved isotopes and their respective electronic state. The shape and properties of these potentials are only partially known. For Strontium some theoretical, as well as experimental work in this area, has been done [83, 85–89]. Experimental loss measurements for Ca are found in [90]. For Ytterbium fewer theoretical studies on the molecular potentials are available. See [91] for calculations of the lowest molecular energy states in  $\text{Yb}_2$ . Experimental work regarding loss measurements can be found in [34, 79, 82, 92].

In the context of this thesis two loss processes involving the  $^3\text{P}_0$  state are of interest:

Isotope	$^{173}\text{Yb}$	$^{171}\text{Yb}$
$\beta_{ee}$	$2.2 \times 10^{-11}$	$5 \times 10^{-11}$
$\beta_{eg}^+$	$3.9 \times 10^{-13}$	
$\beta_{eg}^-$	$< 3 \times 10^{-15}$	
$\overline{\beta_{eg}}$		$5 \times 10^{-11}$

**Table 2.4. | Inelastic scattering coefficients for the fermionic isotopes.** Loss coefficients for the two fermionic isotopes. For  $^{171}\text{Yb}$  the loss coefficient was measured at  $\mu\text{K}$  temperatures thus p-wave scattering is included in the values given. For lower temperatures a slight decrease of the values are expected [79]. The authors in [34] note that  $\beta_{eg}^+$  for  $^{173}\text{Yb}$  was measured in a quasi 2D system and expect a significant increase of the values for 3D-systems [59]. All numerical values given in  $\text{cm}^3/\text{s}$ . Table from [59].

- $^1\text{S}_0 \leftrightarrow ^3\text{P}_0$  inelastic scattering.
- $^3\text{P}_0 \leftrightarrow ^3\text{P}_0$  inelastic scattering.

These scattering processes are *two-body losses* and are characterized by a *loss coefficient*  $\beta$ . The loss coefficient relates the time evolution of the density of an atomic sample to the density of the two involved scattering partners:

$$\frac{dn_e}{dt} = -\beta_{ee}n_e^2 \quad (2.11)$$

$\beta_{ee}$  is the loss-coefficient for  $^3\text{P}_0 \leftrightarrow ^3\text{P}_0$  inelastic scattering while  $^1\text{S}_0 \leftrightarrow ^3\text{P}_0$  losses are denoted with  $\beta_{eg}^+$  and  $\beta_{eg}^-$ . The total time evolution of a mixture of unpolarized  $|g\rangle$  and  $|e\rangle$  atoms is described by [79]:

$$\begin{aligned} \dot{n}_g &= -\Gamma_g n_g - \beta_{eg} n_g n_e \\ \dot{n}_e &= -\beta_{ee} n_e^2 - \Gamma_e n_e - \beta_{eg} n_g n_e \end{aligned} \quad (2.12)$$

where single particle losses  $\Gamma_g$  and  $\Gamma_e$  are included but the difference in  $\beta_{eg}^+$  and  $\beta_{eg}^-$  is neglected for brevity. Numerical values for  $\beta_{ee}$  and  $\beta_{eg}^\pm$  for the fermionic isotopes are available and are shown in table 2.4.

In the experiments described in this thesis typical atomic densities in optical lattices are in the order of  $10^{14}/\text{cm}^3$ . Using the data for  $^{173}\text{Yb}$  from table 2.4 loss-rates of

$$\begin{aligned} \Gamma_{ee} &= \beta_{ee} \times 10^{14} \text{ cm}^3/\text{s} \approx 1000/\text{s} \\ \Gamma_{eg} &= \beta_{eg} \times 10^{14} \text{ cm}^3/\text{s} \approx 10/\text{s} \end{aligned} \quad (2.13)$$

are expected.



### 2.3.3. Polarizabilities

Laser light interacting with an atom induces an atomic dipole moment [93]. The induced dipole moment interacts with the electromagnetic field. The interaction energy in a laser field with intensity  $I$  is:

$$U_{\text{dip}} \propto \text{Re}(\alpha) I \quad (2.14)$$

The strength of the interaction is given by the complex polarizability  $\alpha$ . Due to the different electronic structure of  $^1S_0$  and  $^3P_0$  these polarizabilities are different for the two states and depend on the laser wavelength. By summing up the contributions of the individual optical transition connecting the two states with higher energy levels  $\alpha_{e/g}$  is calculated. The result is shown in figure 2.2.

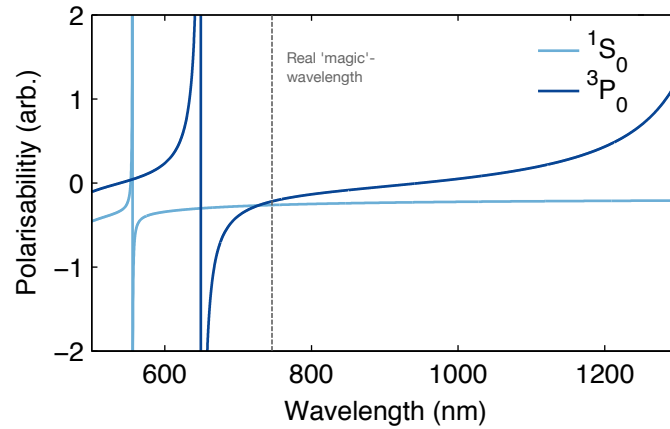


**Figure 2.2. | Real part of complex polarisability of Yb.** Shown is the real part of the complex polarisability of the the ground and excited state of Ytterbium.  $\text{Re}(\alpha)$  is calculated by summing up relevant optical transitions connecting the two states to other energy levels. The 556 nm intercombination transition as well as the  $^3P_0 \leftrightarrow ^3S_1$  transition at 649 nm are clearly visible. To the right side the beginning of the  $^3P_0 \leftrightarrow ^3D_1$  transition at 1388 nm can be identified. The points of equal polarisability (“magic” wavelength) is experimentally and theoretically determined to be 759 nm. The discrepancy between the here presented calculation can be resolved by a relativistic many body calculation [94].

The dominant transition for the ground state is the principal 399 nm transition which results in an attractive dipole potential for almost all wavelengths above 399 nm with the exception of the region around 556 nm. For the excited state the dominant contribution is  $^3P_0 \leftrightarrow ^3S_1$  at  $\lambda = 649$  nm which results in an attractive potential from  $\lambda = 649$  nm up to about  $\lambda = 950$  nm. Beyond  $\lambda = 950$  nm the influence of the  $^3P_0 \leftrightarrow ^3D_1$  transition at 1388 nm dominates resulting in a repulsive interaction for the excited state while the ground state still experiences an attractive potential. The wavelength where  $\alpha_e = \alpha_g$  is called “magic”

wavelength and is important to suppress intensity induced broadening and shifting of the clock-transition (see section 4.1.2 and section 5.4). The magic wavelength was measured to  $\lambda_m = 759$  nm [95]. This differs by more than  $\Delta\lambda > 30$  nm from the polarisability crossing calculated here. The difference is resolved by a relativistic many-body calculation performed in [94].

The possibilities offered by the differential polarisabilities will be discussed further in chapter 5.4 but it is already apparent that the electronic structure of Yb allows working with mixtures of  $^1S_0$  and  $^3P_0$  in trapping potentials which are trapping, anti-trapping or do not influence atoms in the ground or excited state at all.

## 2.4. Conclusion

In this chapter, the most fundamental properties of Ytterbium were presented. Most importantly is the fact that next to elastic scattering there exists significant inelastic scattering channels when atoms in the excited state scatter with other atoms, either in the ground or excited state. While losses are often seen as an obstacle to performing meaningful measurements later in this thesis it is shown how these losses can be used to study many-body dynamics and extract useful information about Fermi-Hubbard systems.

### 3. Degenerate Quantum Gases of Yb

The cooling of Alkaline-Earth like (AEL) atoms like Ytterbium or Strontium is a very active field of research because of their unique atomic features. While quantum degenerate gases of Ytterbium [66] as well as Strontium [29] have already been realized a couple of years ago, laser cooling and trapping and successive evaporative cooling is a challenging task. The negligible ground state magnetic moment makes trapping using standard magnetic traps impossible. To reach the quantum degenerate regime, trapping and cooling using optical dipole traps [93] is the solution to this problem. While a standard in the field of ultracold quantum gases after precooling in a magnetic trap, the *all optical* creation of degenerate gases brings its own set of challenges: the initial temperature of the atoms need to be as low as possible while the initial depth of the dipole trap needs to be deep enough, the trap frequencies need to be high to be able to evaporate quickly and on the other hand low final trapping frequencies at the end of the evaporative cooling cycle are required to create a homogeneous sample which can be effectively loaded into the optical lattice. These requirements can contradict itself because of finite laser power which can make it impossible to find a single, crossed dipole trap which is able to fulfill all requirements.

The solution to this problem presented here is a three beam crossed dipole trap. The system is based on three focussed laser beams operated at different wavelengths, beam waists, and intensities. Initial loading from the magneto-optic trap (MOT) is carried out by a tightly focused, high power beam. The gas is cooled near quantum degeneracy and is then loaded into two crossed beams with significantly larger beam waists. Final evaporative cooling yields a quantum degenerate gas for bosons as well as for fermions.

In this chapter first an overview of the experimental setup is given and precooling and cooling in the 2D-/3D-MOT setup is briefly described and characterized (section 3.1). Thereafter the dipole trap system and evaporative cooling scheme is presented (section 3.2) and characterized in detail using a quantumgas of bosons (section 3.3). The same evaporation scheme as for the bosons is used in section 3.4 to create a Fermi gas with arbitrary spin-states.

The MOT cooling scheme and MOT performance characteristics have been described in detail in the PhD thesis of Sören Dörscher [58] and Alexander Thobe [57] and published in [96]. The vacuum system, as well as laser cooling laser systems, have been planned and setup by A. Thobe and S. Dörscher. The laser cooling systems and evaporative cooling schemes using a single color dipole trap (the “old” setup) have been implemented by A. Thobe, S.

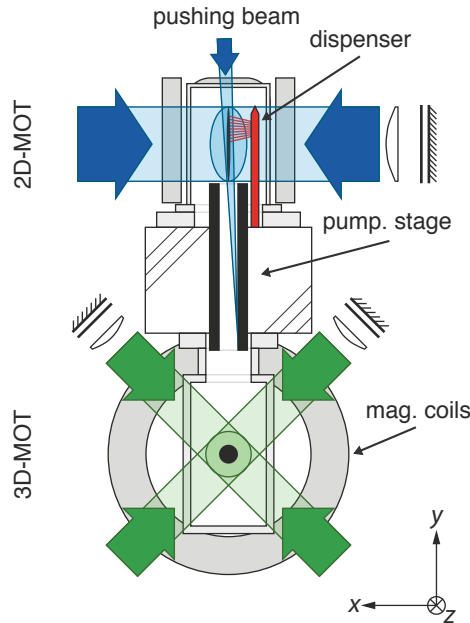


**Figure 3.1. | Scheme of the experimental setup.** Shown is the vacuum system and the laser beams for cooling Ytterbium to  $\mu\text{K}$  temperatures. The atoms are released from a dispenser which is heated by a current flow. After capture and precooling in the 2D-MOT on the blue transition the atoms are pushed from the upper glass cell to the lower cell by a pushing beam. There the atoms are captured by the green 3D-MOT.

Dörscher, and the author. The new bichromatic dipole trap setup described in this thesis was planned by A. Thobe and setup by A. Thobe, André Kochanke, Thomas Ponath and the author. Trapping and cooling schemes have been developed by A. Kochanke and the author. The high-resolution detection was planned and characterized by Torben Sobottke and implemented by A. Kochanke and the author. Data analysis was performed by the author.

### 3.1. Laser Cooling and General Experimental Setup

This section will give a brief overview of the experimental setup used to create quantum degenerate gases of Ytterbium. Details are found in [57, 58]. The first part describes the general layout and the 2D-/3D-MOT system. It is kept brief. The second part describes the detection system in more detail. This system was implemented mainly by Torben Sobottke and the author. Afterwards, the performance of the 2D-MOT is characterized.

### 3.1.1. Vacuum System and Laser Cooling

#### General Layout and Vacuum System

The heart of the setup is a vacuum system consisting of two glass cells connected by a differential pumping stage. Located on top of each other the system is relatively compact and allows good optical access from almost all directions. The setup is schematically shown in figure 3.1.

#### 2D-MOT

The upper glass cell and vacuum system is used as a source for Ytterbium atoms. A commercially available dispenser is heated by a constant current and emits a beam of thermal atoms with an isotope distribution given by the natural abundance. These atoms are captured in a 2D-MOT operated on the principal  $\lambda = 399$  nm transition. The 2D-MOT consists of two retroreflected, elongated beams as shown in the top of figure 3.1. The result is a cigar-shaped cloud of atoms. The atoms are cooled in two dimensions thus leaving the 2D-MOT volume along the  $y$ -direction. A pushing beam (approx  $\Delta = 1 \times \Gamma_{399}$  red detuned) is used to increase the flux of atoms from the upper cell to the lower cell by transferring momentum along the differential pumping stage. To suppress resonant scattering of  $\lambda = 399$  nm photons in the 3D-MOT, the pushing beam is carefully aligned to hit the inner part of the pumping stage.

#### 3D-MOT

In the lower glass cell, all experiments are performed. The starting point is a retroreflected 3D-MOT operated on the  $\lambda = 556$  nm intercombination transition. While the narrow intercombination transition allows a low Doppler temperature of  $T_D \approx 4 \mu\text{K}$  the velocity class of atoms captured by the 3D-MOT is equally narrow, effectively reducing the loading rate of the 3D-MOT. The problem was circumvented by an artificial broadening of the light to a width of 7 MHz using an acousto-optic modulator (AOM). The broadening is subsequently reduced and finally switched off to reach the lowest possible temperatures (for MOT performance see section 3.1.3). The magnetic field for the 3D-MOT is created by a pair of water-cooled coils. These coils can be used to generate field gradients as well as homogeneous fields.

### Magnetic Compensation Coils

For compensation of stray magnetic fields, another set of coils surrounds the 3D-MOT cell (not shown in figure 3.1). These stray fields are for example generated by ion-getter-pumps of the vacuum system. Beside of stray field compensation, these coils are used to apply fields in arbitrary directions which is not possible by the main coils used for the 3D-MOT. This enables applying a defined quantization axis when specific optical spin transitions need to be addressed.

#### 3.1.2. Detection

The detection system is based on standard cold-atom absorption imaging [72]. Imaging is performed on the spectrally broad blue transition (see section 2.2.1). This transition offers two advantages in terms of absorption imaging: first because of the large linewidth the detected number of atoms is robust against small laser frequency fluctuations. Second, the large linewidth causes a large saturation intensity  $I_{\text{sat}} \approx 60 \text{ mW/cm}^2$  which means that it is easy to fulfill the requirement of undersaturated imaging [97] with a good signal to noise ratio on the cameras.

Absorption imaging is possible along the z-axis and x-axis of the experiment. The principle of detection is the same in both axes: two images are taken, one with the atomic cloud and another without the atomic cloud. The first image is called *absorption image A*, the second *reference image R*. Additionally, two *dark*  $D_{R,A}$  images without the imaging laser are taken shortly after the absorption or reference image. This allows the calculation of the atomic 2D-density distribution  $n(x, y)$  according to [97]:

$$-n(x, y)\sigma = \ln \frac{R - D_R}{A - D_A} \quad (3.1)$$

Here  $\sigma$  is the absorption cross section and is calculated from known atomic properties. The two axis have vastly different imaging properties because of optical elements obstructing the optical path or distortion of the wavefront by transmission through non-planar optical elements.

#### Detection 1 along the x-axis

The detection along the x-axis has mostly unobstructed view on the atomic cloud and is therefore the significantly better axis in terms of achievable resolution. Details of the detection on this axis can be found in the bachelor thesis of Torben Sobottke [98] which was supervised by the author.

The heart of the detection along the x-axis is a commercially manufactured diffraction limited objective. It was designed for maximal numerical aperture while being compact enough to allow easy alignment in between the 3D-MOT coils. The objective has a numerical aperture of  $NA = 0.27$  and a working distance of  $d_w = 37.55$  mm. In figure 3.2 the objective is schematically shown. It is compensated for the optical aberrations introduced by the walls of the glass cell. Using the imaging wavelength of  $\lambda = 399$  nm this allows a resolution of  $d = 1.07 \mu\text{m}$  with coherent light calculated according to the *Sparrow resolution criterion* [99]. Experimentally the resolution was determined to be at least  $d = 1.35 \mu\text{m}$  but was limited by the availability of a structure small enough: the diameter of the pinhole used to determine the resolution is the same size as the resolution itself, violating the requirement of a point source. The resolution is not enough to resolve atoms individually in the optical lattice which would require a resolution on the order of 500 nm but is still very good compared to typical quantum gas machines and allows in-situ imaging of the atoms in the dipole trap.

The objective collimates the image of the atomic cloud. The collimated image is subsequently focussed onto a camera. The ratios of front focal length and back focal length determine the magnification of the imaging system. The camera on this axis has a pixel size of  $d_{px} \approx 13 \mu\text{m}$ . This means for magnifications below  $m \approx 13$  the imaging system is limited by the pixel size and not by the resolution of the objective. However, larger magnifications limit the available *field of view* (FOV). During the course of this thesis, all measurements were performed with an intermediate magnification of  $m = 4.71$ .

## Detection 2 along the z-axis

The second detection axis is limited by multiple mirrors transmitting the imaging beam through a glass substrate with an angle of incidence of  $45^\circ$ . These nonplanar surfaces are extremely bad for the wavefront and introduce large optical aberrations. Imaging on this axis is only usable for large expanded clouds. The camera used on this axis has a pixel size of  $d_{px} \approx 6.7 \mu\text{m}$  and a magnification of  $m \approx 2.2$  is used. Because of the bad optical properties of the beam, it was decided to use a simple achromatic lens to collimate the image of the atomic cloud and another achromatic lens to focus the image onto the camera. The whole imaging system was again analyzed in detail in [98].

### 3.1.3. 2D- & 3D-Magneto Optical Trap Performance

The setup of a blue 2D-MOT and green 3D-MOT for the creation of Ytterbium quantum gases has never been implemented before. Thus a comprehensive characterization of the whole system has been performed [57, 58] and published [96]. The central result of this characterization is shown in figure 3.3. Here the loading rate from the 2D-MOT into the 3D-MOT has been studied for different detunings  $\Gamma$  and magnetic fields gradients. The number of atoms was determined by absorption imaging.

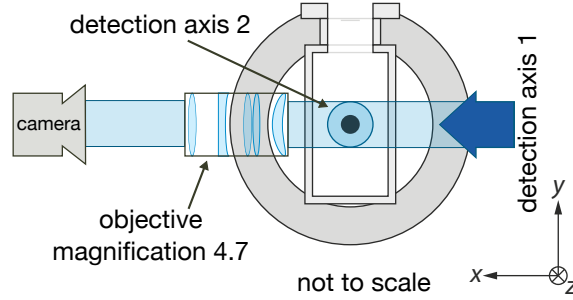


**Figure 3.2. | Layout of absorption detection setup.** Absorption imaging for counting atoms and imaging the atomic density or momentum distribution (mostly after *time-of-flight* (TOF)) is performed on two perpendicular axis shown in the schematic above.

An optimal 3D-MOT loading rate at a magnetic field gradient of around 60 G/cm and a detuning of  $\Delta \approx -1.2\Gamma$  is found for  $^{174}\text{Yb}$  and  $^{173}\text{Yb}$ . For the fermionic isotope, a sharp decline of the loading rate at  $\Delta \approx -1.7\Gamma$  is observed. This loss of loading rate is attributed to the disadvantageous hyperfine structure of  $^{173}\text{Yb}$  in the  $^1\text{P}_1$  state which is shown in figure 3.4. The 2D-MOT is operated red detuned to the  $F = 5/2 \leftrightarrow F' = 7/2$  transition. Unfortunately the transition  $F = 5/2 \leftrightarrow F' = 3/2$  is red detuned to the  $F = 5/2 \leftrightarrow F' = 7/2$  with a splitting of 72 MHz. With a linewidth of the blue transition of  $\Gamma_{399} = 2\pi \times 29$  MHz the  $F' = 3/2$  transition is about  $-2.5\Gamma_{399}$  red detuned to the 2D-MOT transition. This means that the laser beams, when red detuned to the 2D-MOT transition, are blue detuned to the  $F' = 3/2$  transition and thus hinder efficient MOT operation. The loading rates of the two isotopes differ by almost one order of magnitude. A factor of two is explained by the difference in abundance of the two isotopes (see section 2.1). The remaining factor four is attributed to the level structure explained above. As it turns out the effect of the  $F' = 3/2$  level is so severe that the polarization of the 2D-MOT beams has to be actively misaligned to achieve the loading rates presented above. This is currently not well understood. A comprehensive discussion of this problem can be found in [57].

### 3.2. Bichromatic Dipole Trap Setup

After the brief overview of the experimental setup for laser cooling and detection the all-optical creation of quantum degenerate gases of fermionic and bosonic Ytterbium is now discussed. The setup presented here is mostly new and was planned after the realization that the old dipole trap system had significantly too large final trapping frequencies ( $\bar{\omega}_{\text{old}} = 91$  Hz) to load significant amounts of fermionic atoms into the lowest Bloch band. The main goal was thus to retain the transfer efficiencies of atoms from the MOT into the dipole trap but reduce the final trapping frequencies considerably. The setup described here is based on a three-beam optical dipole trap. The laser system and the beam shaping optics will be



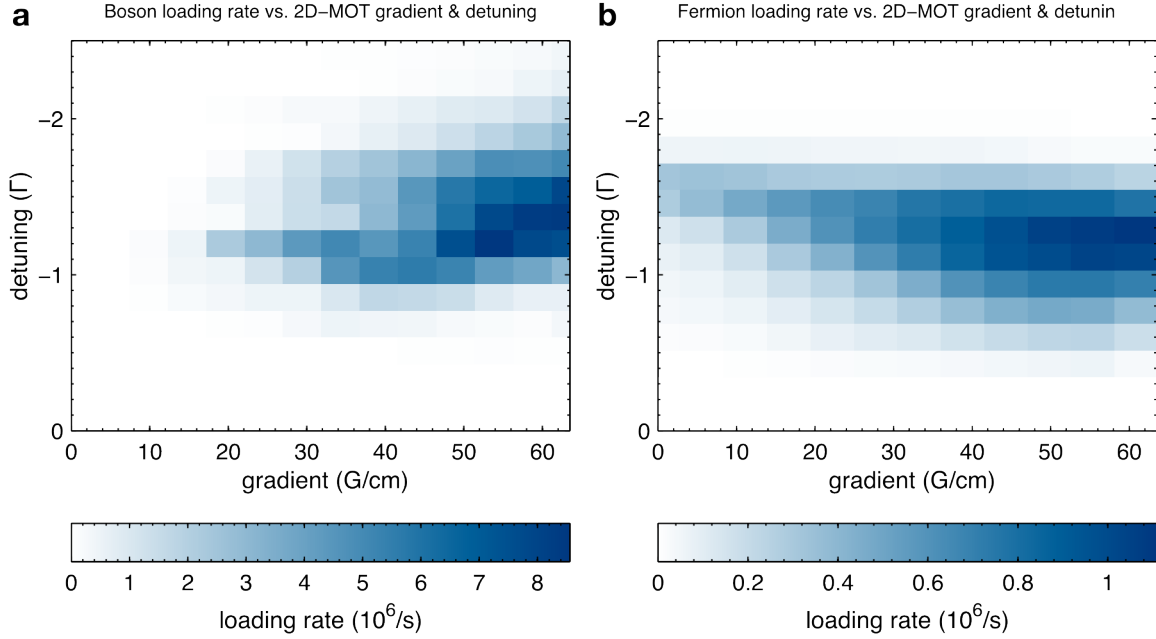


**Figure 3.3. | 3D-MOT Loading rate depending on 2D-MOT detuning and gradient.** The loading rate from the 2D-MOT into the 3D-MOT is shown depending on the 2D-MOT gradient and frequency detuning for  $^{174}\text{Yb}$  in **a** and for  $^{173}\text{Yb}$  in **b**. The fermionic isotope shows a significant decrease in loading rate at  $\Delta \approx -1.7\Gamma$ . This decrease is attributed to the  $F = 5/2 \leftrightarrow F' = 3/2$  transition at around  $-2.5\Gamma$ .

explained in the Ph.D. thesis of André Kochanek. The characterization and implementation at the experiment is described in the following.

### 3.2.1. Fundamental Relations

The basis for optical dipole traps is the interaction between atoms and laser beams operated off resonance. The oscillating electric field of the laser beam induces an electric dipole moment in the atoms which interacts with the electromagnetic field of the light. The result is an induced potential described by [93]:

$$U_{\text{dip}} = -\frac{1}{2\epsilon_0 c} \text{Re}(\alpha) I(\mathbf{r}) \quad (3.2)$$

Note that in section 2.3.3 the plotted polarisability includes the factor  $-1/(2\epsilon_0 c)$ . By approximating the real potential with a harmonic potential a trap frequency can be assigned to each spatial direction. The trap frequency scales as:

$$\omega \sim \sqrt{U_{\text{dip}}} \sim \sqrt{I} \quad (3.3)$$

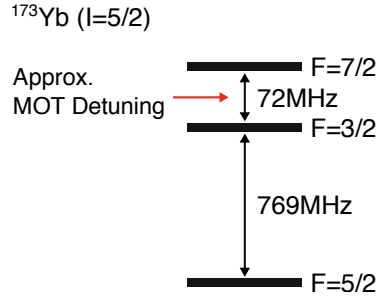


**Figure 3.4. | Hyperfine structure of  $^{173}\text{Yb}$  for blue  $^1\text{S}_0 \leftrightarrow ^1\text{P}_1$  transition.** Shown is the hyperfine structure of  $^{173}\text{Yb}$  for the transition from  $^1\text{S}_0$  into the  $^1\text{P}_1$  state. The 2D-MOT is operated approximately one linewidth red detuned to  $F = 7/2$ :  $\Delta = -\Gamma_{399}$ . The  $F = 3/2$  state is only  $2.5\Gamma_{399}$  red detuned to  $F = 7/2$  and thus 2D-MOT operation is severely impacted.

Typically optical dipole traps are formed by laser beams focussed to *waists*  $w_0$  in the order of some ten to a couple of hundred of  $\mu\text{m}$ . In most cases, the beams are Gaussian  $\text{TEM}_{00}$  modes. These beams have Gaussian shaped transversal intensity distributions and their transversal width  $w(z)$  along the propagation axis is given by [93]:

$$w(z) = w_0 \sqrt{1 + \left(\frac{z}{z_R}\right)^2} \quad (3.4)$$

Here  $w_0$  is the minimal waist of the beam,  $z$  the position along the propagation vector and  $z_R$  the Rayleigh range. Due to gravity the atoms will not be trapped at the center of the gaussian beam but at the point where the gravitational force is balanced by the dipole force. This *sag* is calculated by:

$$\begin{aligned} \frac{1}{2}m\omega_y^2 z_y^2 &= mgz_y \\ z_y &= \frac{2g}{\omega_y^2} \end{aligned} \quad (3.5)$$

To find whether a dipole trap is able to hold the atoms against gravity one has to consider the total potential consisting of the dipole potential and the gravitational potential and check whether a potential barrier deep enough compared to the kinetic energy of the atoms exists. Thus for very shallow dipole traps the scaling of the trapping frequencies differ significantly from  $\sim \sqrt{I}$  and will be much lower than expected.

For ultracold quantum gas experiments where the atoms are supposed to be loaded into an optical lattice, low trap frequencies are desired. In general, a dipole trap superimposed to an optical lattice creates an additional energy scale resulting for example in *Mott insulator shells* [100]. For a spin-polarized fermionic gas the atoms are not able to form doubly

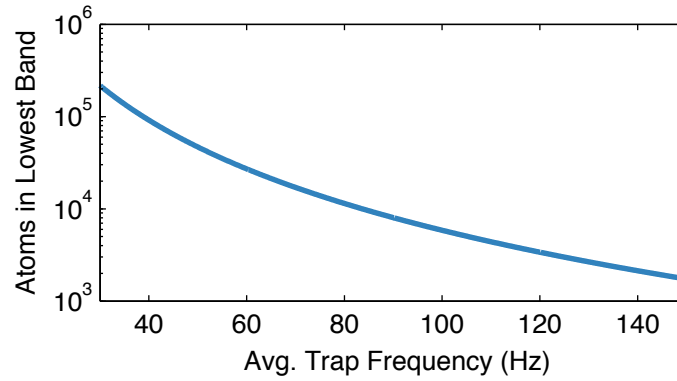


**Figure 3.5. | Number of atoms loaded into the lowest Bloch band.** Shown is the number of fermionic atoms loaded into the lowest Bloch band of a cubic 3D-optical lattice depending on the average trap frequency of the optical dipole trap.

occupied states in the lowest band and therefore there exists an upper limit for the number of atoms loaded into the lowest band. The number of fermions which are loaded from a dipole trap into the lowest band of a cubic optical lattice with average trap frequency  $\bar{\omega}$  is [101]:

$$N \approx \left( \frac{\pi^2 \hbar}{2m\bar{\omega}d^2} \right)^3 \sim \frac{1}{\bar{\omega}^3} \quad (3.6)$$

Here  $d$  is the lattice spacing.  $N$  is plotted for various trap frequencies in figure 3.5 for a lattice spacing of  $d = 400$  nm. The old dipole trap had an average trap frequency of 91 Hz which yields a maximum number of atoms  $N = 7700$ . The new setup described here increases this number by two orders of magnitude.

### 3.2.2. Design Considerations for the Bichromatic Dipole Trap

A dipole trap suitable for experiments with ultracold atoms intended to be loaded into the lowest Bloch-band of an optical lattice need to fulfill a couple of requirements: first, the initial trap depth and volume needs to be as large as possible to allow efficient capture of atoms from the 3D-MOT. As a rule of thumb, the initial trap depth needs to be a factor of ten larger than the temperature of the MOT [102]. High trap frequencies are desired to allow fast evaporative cooling. Moreover, low trap frequencies at the end of the evaporative cooling cycle are desirable to minimize the distortion of the optical lattice band structure. Mostly because of finite available laser power these requirements are at odds with each other and thus it is complicated or impossible to find a compromise which fulfills all those requirements. Here the problem was mitigated by implementing a crossed dipole trap based on three laser beams. One beam with a tight focus is used for transfer from the 3D-MOT

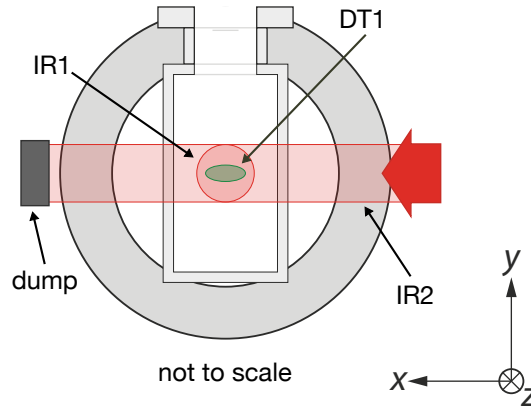


**Figure 3.6. | Schematic of the three beam bichromatic dipole trap.** The dipole trap setup consists of three beams. The beams DT1 and IR1 are propagating on the same axis while the confinement along the z-axis is created by IR2. DT1 is tightly focussed and only used at the beginning of the evaporative cycle to increase the amounts of atoms transferred from the 3D-MOT into the dipole traps. After ramping down and switching off DT1 the atoms are held in IR1 and IR2. Further evaporation yield gases with temperatures below  $T_C$  or  $T_F$  respectively.

and initial evaporation while the other two have significantly larger waists and are used for final evaporation and transfer to the optical lattice. A schematic of the three dipole trap beams is shown in figure 3.6 and described in detail in the next few sections.

### DT1

The first beam (called *DT1*) was described in [57, 58]. It is based on a high intensity  $\lambda = 532\text{ nm}$  laser. The beam is shaped elliptically and propagates along the z-axis. The  $1/e^2$  radii are  $w_{0,x} = 29\ \mu\text{m}$  and  $w_{0,y} = 18\ \mu\text{m}$ . The beam has a maximal power of around  $P_{DT1} = 9\text{ W}$ . These parameters yield a initial trap depth of  $616\ \mu\text{K}$  along the gravity direction.

### IR1

The second beam is called *IR1*. It propagates along the same axis as DT1. Operated at a wavelength of  $\lambda = 1064\text{ nm}$  with a round shape with mean radius of  $w_{0,IR1} = 54\ \mu\text{m}$  and a maximal power of  $P_{IR1} = 1\text{ W}$  at the position of the atoms. With this parameters an maximal trap depth of  $4.9\ \mu\text{K}$  is possible. The beam by itself is not able to hold the atoms against gravity thus the depth is given in terms of the theoretical dipole potential without the influence of gravity.

## IR2

The third beam is called *IR2* and propagates along the x-axis. It is elliptically shaped with waists of  $w_{0,y} = 65 \mu\text{m}$  and  $w_{0,z} = 225 \mu\text{m}$  and, like IR1, operated at a wavelength of  $\lambda = 1064 \text{ nm}$  with  $P = 10.5 \text{ W}$ . This trap is able to hold the atoms against gravity with a depth of  $2.6 \mu\text{K}$ .

### 3.2.3. Beam Alignment and Evaporation Scheme

The three beam dipole trap needs to be carefully aligned to increase atom transfer efficiency and thereby evaporation performance. The first step is aligning DT1. By changing the beam alignment and the focus position at full power the number of atoms transferred from the 3D-MOT is optimized. Next IR1 is aligned to propagate along DT1. At full power of IR1 the power of DT1 is decreased to a point where the combined trap of DT1 and IR1 hold the atoms. Then by finetuning the position of IR1 the final alignment is performed. Next IR2 is switched to full power and DT1 is switched off. The atoms are now located in the crossed region of IR1 and IR2. By changing the position of IR2 the number of atoms in the crossed region is maximized. Finally, the complete evaporation ramp (described below) is used to perform fine adjustments of the beam position of IR2.

The complete evaporation ramp is sketched in figure 3.7. It is based on two phases. At the beginning of the first phase, all dipole trap beams are switched on to full power. DT1 is subsequently lowered to 200 mW during a 5 s exponential ramp. In the next two seconds, DT1 is ramped to its minimal value of about 10 mW and then switched off. During this first phase, both IR beams remain at full power. While DT1 cools the ensemble the atoms are captured in the crossed region of the two infrared (IR) beams. The temperature at the end of phase one is still above the critical temperature for bosonic isotopes and above the Fermi-temperature for the fermionic isotope. In the second evaporation phase, the power of IR1 is reduced to 55 mW while IR2 is ramped to 7.7 W. The ramp for both IR beams is exponential and its duration is 8 s. This last step results in quantum degenerate gases. To stop the evaporation and ensure constant particle numbers, the two IR trapping beams are linearly ramped up to about 5% above their lowest value at the end of the complete evaporation process. The complete ramp has been developed experimentally and all parameters were optimized for particle numbers and temperatures.

The ramp presented here is for the bosonic isotope  $^{174}\text{Yb}$ . For the fermionic isotope  $^{173}\text{Yb}$  the second phase is extended to 12 s which was again determined experimentally and slightly improved the number of particles in the final trap. The necessary increase in the time of the last phase is attributed to the reduction of evaporation efficiency as the gas gets cooled into the quantum degenerate regime [103, 104] and the overall worse performance of the experimental setup for the fermionic isotope.

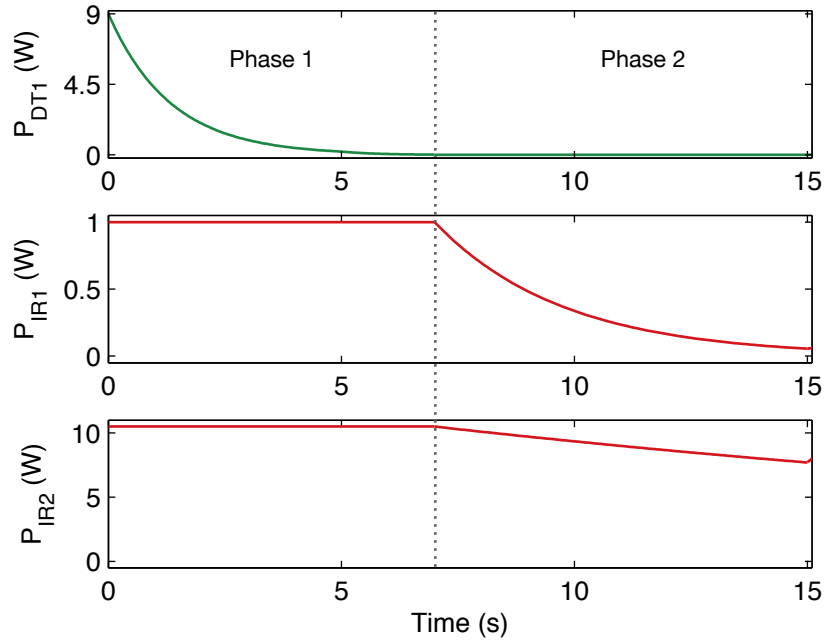


**Figure 3.7. | Evaporation Scheme for the bosonic isotope in the bichromatic crossed dipole trap.** The evaporation is based on two phases. In the first phase, the tightly focussed green dipole trap beam is exponentially ramped down and switched off. The ramp has two-time constants with the slower evaporation during the last two seconds of the first phase. During the second phase the IR traps are ramped down and at the end quantum degenerate gases are created. A small increase of the power of both beams ensures stopping of the evaporation and constant particle numbers.

### 3.3. Bose-Einstein Condensation with the Bichromatic Dipole Trap

Using the evaporation ramp described above the bosonic isotope  $^{174}\text{Yb}$  was used to optimize and characterize the new trapping potential.

#### 3.3.1. Temperature and Particle Number during the Evaporation

The number of atoms and the temperature during the evaporation ramp is shown in figure 3.8 where the temperature of the thermal cloud was determined by the rate of expansion of the atoms after time-of-flight (TOF). The number of atoms is counted by standard absorption imaging. The transfer from the green dipole trap DT1 into IR1 and IR2 is clearly visible in the temperature measurement starting at around  $t = 6$  s (figure 3.8a). The

temperature reduction is slowed because the atoms are mainly trapped by IR1 and IR2. The further reduction of the power of DT1 is not significantly lowering the trap barrier and thus evaporation is slowed. After starting the ramp for IR1 and IR2 cooling is resumed. First signs of BEC are observed at around  $T = 100$  nK. This number is significantly lower compared to the dipole trap setup used before [57] which showed first signs of BEC at  $T = 500$  nK. The reduction in critical temperature is attributed to the lower trapping frequencies of the new IR trap which is almost a factor of three lower (see next section). The decrease in temperature at  $t = 14$  s is attributed to fit problems because of the very small thermal cloud. At  $t = 15$  s a pure BEC is created and therefore no temperature is given.

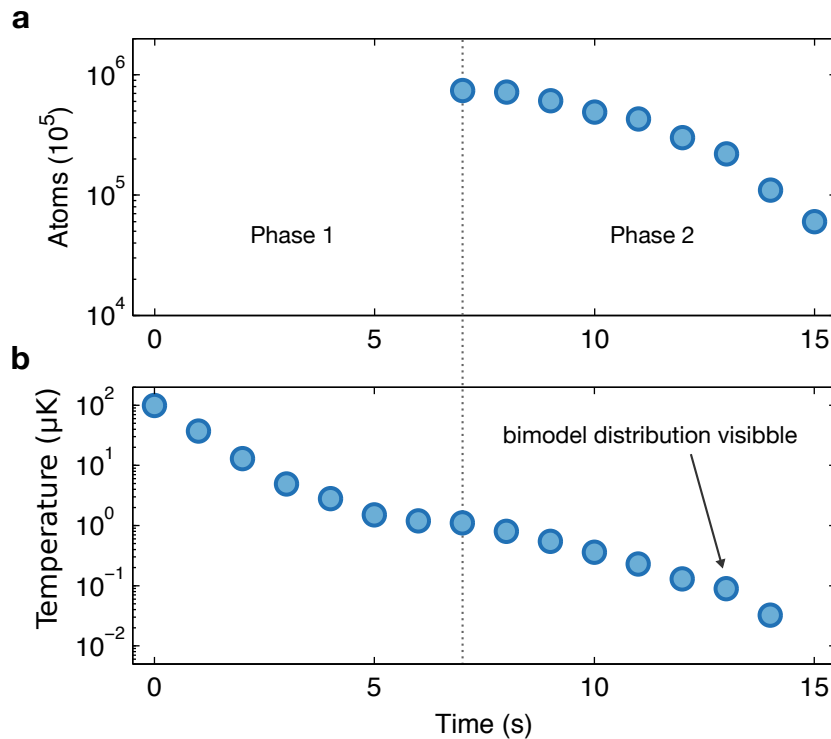


**Figure 3.8.** | **Characterization of evaporation ramp in bichromatic dipole trap.** Shown are the number of atoms (a) and the temperature (b) during the evaporation ramp. The temperature is deduced from individual measurements of the cloud expansion rate. The first signs of a bimodal distribution indicating the presence of a BEC is observed at around 100 nK. Atom numbers could not be determined for the first part of the ramp because the cloud is too large to be imaged on the camera. The grey line separates the two evaporation phases. At  $t = 15$  s a pure BEC is created and therefore no temperature is given.

From the measurement of the number of atoms (see figure 3.8a) an increase in the rate

of atom loss is observed near the transition to the BEC phase. This efficiency decrease was also observed in the old dipole trap setup and is explained in terms of a reduced dimensionality of the effective evaporation. When the dipole traps is lowered the influence of gravity increases. Thus at lower powers, the trapping potential is more and more deformed with the lowest barrier of escape at the (geometrically) lowest point in the trap. The atoms are predominantly lost at this point. The evaporation becomes more and more one dimensional. This effective decrease in dimensionality reduces the efficiency of evaporative cooling [105, 106].

A phase transition to a BEC is only possible if the *phase-space density*  $\rho$  can be increased sufficiently so that  $\rho \approx 2.612$  [107]. From the temperature, particle number and the trapping frequencies the phase-space density is determined according to [107]:

$$\rho = n(\bar{\omega}, T) \lambda_{\text{DB}}(T)^3 \quad (3.7)$$

where  $n(\bar{\omega}, T)$  is the density of the gas depending on the average trap frequency and temperature and  $\lambda_{\text{DB}}(T)$  is the thermal DeBroglie-wavelength which is again temperature dependent. In figure 3.9a the phase-space density is shown for phase two of the evaporation ramp. The last two points are omitted here because of the aforementioned problems in determining the temperature. At the beginning of the second phase of the evaporation at  $t = 7$  s a decrease in phase-space density is observed. It is currently not well understood why the phase-space density decreases but it seems that the transfer from DT1 into IR1 and IR2 slightly heats the sample. Figure 3.9a additionally shows the raw images of the atomic cloud at  $t = 12$  s and  $t = 13$  s. At  $t = 12$  s a pure thermal cloud is observed while at  $t = 13$  s a bimodal distribution is present. This observation fits very well with the theoretically predicted phase-space density at which the BEC transition should occur.

The efficiency of evaporative cooling is characterized by the *evaporation efficiency*  $\gamma_{\text{eff}}$  which is defined by [102]:

$$\gamma_{\text{eff}} = - \frac{\ln(\rho_f/\rho_i)}{\ln(N_f/N_i)} \quad (3.8)$$

The evaporation efficiency is a measure for the gained phase space density per lost particle. Here  $\rho_f$  is the final phase space density,  $\rho_i$  is the initial phase space density,  $N_f$  the final atom number and  $N_i$  the initial number of atoms. The second step of the evaporation scheme yields (see figure 3.9b):

$$\gamma_{\text{eff}} \approx 3.42 \quad (3.9)$$

This efficiency fits well to efficiencies listed in [102] which lie in the range of  $\gamma_{\text{eff}} = 2.5 - 3.5$ , measured at various experimental setups.

At the end of the dipole trap evaporation cycle, a pure BEC with about  $6 \times 10^4$  atoms is created. Note that after this measurement had been performed it was possible to increase the size of the BEC by a factor of 3 by iterating the alignment process outlined in 3.2.3 and overall improvements in the experimental performance. The measurements shown here should, therefore, be regarded as a relative measure of the evaporative cooling efficiency.



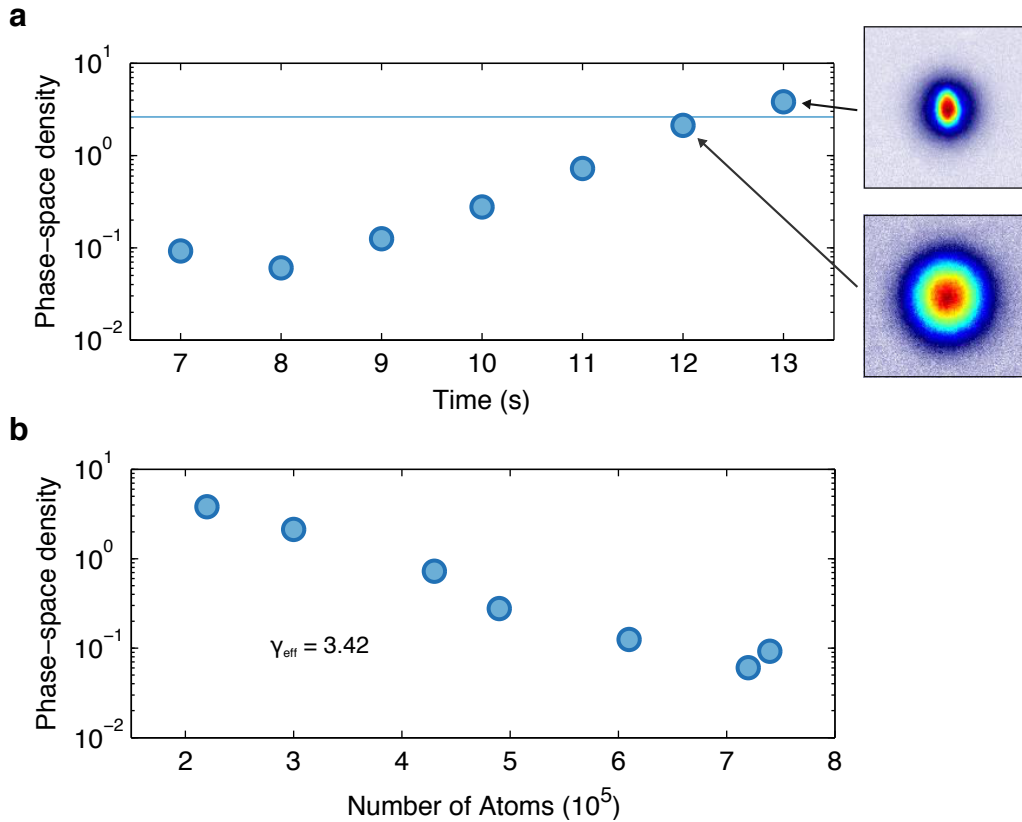


**Figure 3.9. | Phase-space density for the second evaporation phase.** **a** shows the phase-space density during the second evaporation phase. The two last steps of the ramp are omitted here because no thermal distribution could reliably be fitted to the data. The horizontal line indicates the theoretical value of  $\rho = 2.612$  where the BEC phase transition should occur. In the raw images, the first sign of a bimodal distribution indicating the presence of a BEC is observed at  $t = 13$ s. In **b** the phase space density is plotted against the number of atoms. From the final and initial phase space density and the initial and final number of atoms the evaporation efficiency  $\gamma_{\text{eff}}$  is calculated.

### 3.3.2. Trap Frequency Measurement

For all later measurements, the precise knowledge of the trapping frequencies in the final trap configuration is of vital importance. To determine the actual trapping frequencies oscillations along all three axes of the trapping potential were induced. Successive measurement of the position allows the determination of the trap frequencies. To induce oscillations misaligned lattice beams are used. A short light pulse displaces the atoms and oscillations can be observed. The result of this measurement is presented in figure 3.10.

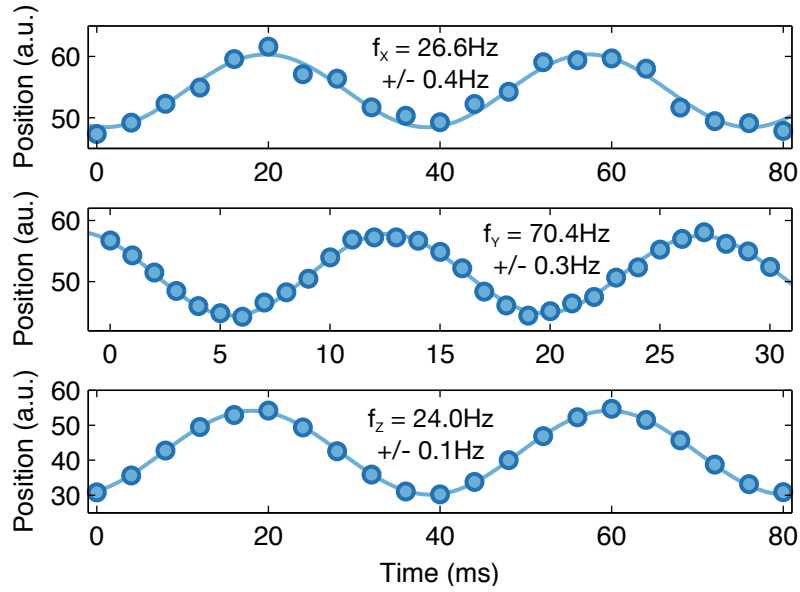


**Figure 3.10. | Trap frequency measurement along all trapping directions.** Shown are trap frequency measurements of a BEC in the final trap depth. Trap oscillation is induced by displacing the BEC using a misaligned lattice beam and observing the resulting oscillations. A sine fit is shown as a blue line extracts the trapping frequency. The errors of the determined trap frequencies are the fit errors. Data is averaged over three ( $x$ -axis) and five experimental runs ( $y$ - and  $z$ -axis).

The trap frequencies are determined to  $\omega_{x,y,z} = 2\pi \times (27, 70, 24) \text{ Hz}$ . From the knowledge of the beam waists and power, the trap frequencies are expected to be  $(30, 78, 28) \text{ Hz}$ . Thus our actual trapping frequencies are about 10% lower than expected. This is in reasonable agreement when considering the multitude of mirrors with different coatings which are in the beam path between the point at which the power of the beams can be measured and the point of the atoms. The average trap frequency for our actual dipole trap is  $\bar{\omega} = 2\pi \times 36 \text{ Hz}$  which is almost a factor of three lower compared to the old setup.

### 3.3.3. Lifetime

During the course of this thesis lifetime and loss measurements for ultracold fermi gases in the excited state of Ytterbium will be presented. As a baseline for these measurements, the lifetime of the BEC particle number in the IR trap was measured. The corresponding data is presented in figure 3.11.

The very good agreement between the simple exponential fit and the data suggests pure

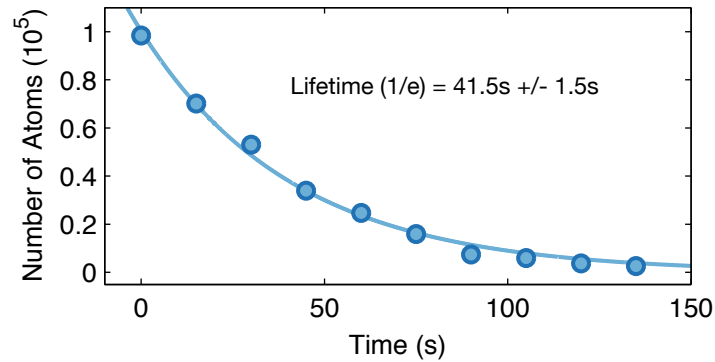


**Figure 3.11. | Particle number lifetime of a BEC in the IR traps.** Shown are the particle numbers in the IR dipole trap after different waiting times. The solid line shows an exponential decay fit to the data. The uncertainty is the error of the regression. The data is averaged over three experimental runs.

single particle loss on the observed timescale. The measured lifetime is  $\tau_{exp} \approx 42$  s and is compared to the photon scattering rate by the two IR beams. The expected lifetime due to photon scattering is  $\tau_{sc} \approx 119$  s which is significantly longer compared to the measured value of  $\tau_{exp} \approx 42$  s. This indicates that the occurring loss can not be fully attributed to dipole trap photon scattering. Other relevant processes are collisions with background gas (the measurement was performed at a pressure of  $p \approx 2.5 \times 10^{-11}$  mBar) and also thermal lensing in the dipole trap beams because of the long experimental cycle times. Still, the observed lifetime is long enough to perform experiments on typical quantum gas timescales.

## 3.4. Ultracold Fermi Gases

After the characterization of the BEC in the new dipole trap setup, the next step is the creation of degenerate fermi gases. The evaporation scheme remains the same. Only the time of the second phase was increased from 8 s to 12 s which showed a slightly improved performance. Because of the similar evaporation technique, only the quantum degenerate Fermi gas and the detection and preparation scheme for different spin mixtures is presented here. An extensive characterization will be found in the Ph.D. thesis of André Kochanke.

### 3.4.1. Spin Preparation and Spin Detection

The scheme for spin preparation and spin detection is the same as described before in [57]. Spin preparation is based on spin-resolved optical pumping before the beginning of evaporative cooling. For this purpose, the green intercombination transition is suitable

because the scattering rate is high enough while it is easily possible to induce a Zeeman splitting which is large enough to address individual spins using magnetic fields. A field of  $B = 67 \text{ G}$  is used to separate the individual spin components by a differential Zeeman shift of 40 MHz. The magnetic field is applied along DT1. Subsequently, resonant light with  $\sigma^+$  polarization along the DT1 axis is used to pump atoms into the desired state. Pumping is performed on the  $F' = 7/2$  transition.

A spin-polarized gas is created by pumping most of the atoms into the desired spin state leaving a couple of percent of atoms in all the other states. Cooling is then carried out as before and a few other spin components are used as a mediator for thermalization. Gases with more than one spin state are pumped into the desired spin states and afterward normal evaporation is carried out.

In Alkali quantum gas experiments the spin distribution is measured using a magnetic field gradient applied during time-of-flight. This kind of spin detection is impractical because of the small magnetic moment (see section 2.3.1). Another technique called *Optical Stern Gerlach* (OSG) [108, 109] is employed which uses a  $\sigma^\pm$  polarized laser beam close to the  $F' = 7/2$  resonance of the  $^1S_0 \leftrightarrow ^3P_1$  transition. This beam induces a  $m_F$  dependent dipole force. The beam is aligned such that the slope of the Gaussian intensity distribution lies on the atomic sample. Immediately after releasing the atomic cloud from all trapping potentials the beam is switched on for 1 ms. During successive time-of-flight expansion, the different spin states are spatially separated. Due to the inhomogeneous intensity of the OSG beam and photon scattering the cloud of atoms gets distorted. Thus OSG spin detection allows only counting of atoms. For temperature measurements, the OSG beam is not applied.

### 3.4.2. Degenerate Fermi Gas

For the fermionic isotope  $^{173}\text{Yb}$  the second phase of the evaporation ramp is prolonged by 4 s to a total evaporation time of 19 s. This results in degenerate fermi gases (DFG) with different temperatures depending on the spin mixture. In figure 3.12 three different combinations of spin states are shown with temperature and number of particles. The temperature was determined by fitting a Thomas-Fermi distribution to the data.

In 3.12a the gas was evaporated to quantum degeneracy without prior spin preparation resulting in  $N = 10^5$  atoms at a temperature of  $T = 0.18T_F$ . At the expense of particles, it is possible to decrease the temperature to about  $10\%T_F$ . When optical pumping is applied prior to evaporative cooling a significant decrease in cooling performance is observed. The temperature rises to  $T > 0.2T_F$  and only  $N = 5 \times 10^4$  atoms remain after the evaporation process. Interestingly the performance for the two spin components and spin-polarized gas is comparable. Two reasons for this behavior can be identified: first, the optical pumping which is used to perform spin preparation heats the atoms and thus more energy has to

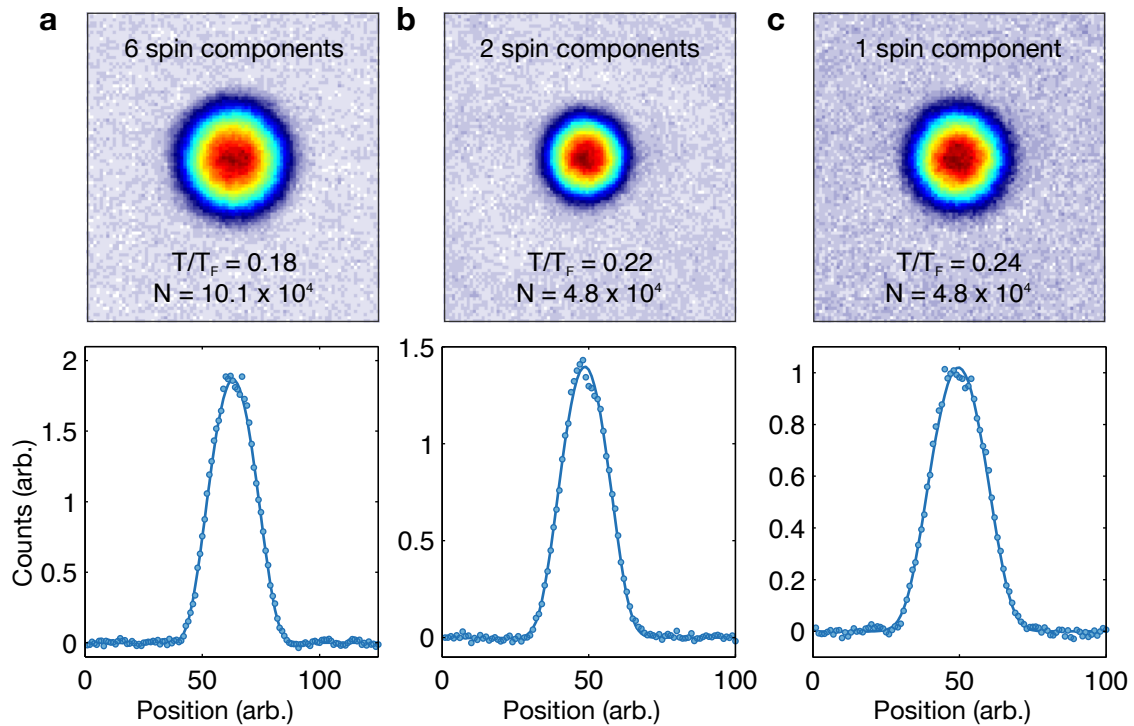


**Figure 3.12. | Temperature and particle number for different ultracold fermionic spin mixtures.** Shown are three different spin mixtures at ultracold temperatures with their corresponding temperatures and particle numbers. The upper part shows the absorption image while in the lower panel a linecut through the center of the cloud with the corresponding fitted Thomas-Fermi distribution is plotted. In **b** prior to evaporative cooling a laser resonant with the green transition was used to pump all atoms in the  $m_F = 5/2$  and  $m_F = 3/2$  state. In **c** most atoms are pumped into the  $m_F = 5/2$  state. No pumping was performed in **a**. Note that **a** was imaged at a longer time-of-flight.

be dissipated by the evaporative cooling. Second, for lower number of spin components at low temperatures, the number of available states to scatter into during thermalization gets smaller because of Pauli blocking. A reduced efficiency is thus expected and was also observed in our setup with the previous dipole trap setup. Similar behavior is presented in [110].

### 3.5. Conclusion

This chapter gave a brief overview of the experimental setup and the techniques used for laser cooling of bosonic as well as fermionic isotopes. A new dipole trap was implemented

and presented here. The main goal was a reduction in average trap frequency. The new bichromatic dipole trap shows good performance for both isotopes. The measured average trap frequency could be reduced by almost a factor of three compared to the previous setup. The evaporation scheme, as well as the optical setup, is robust on a day to day basis and thus is a good starting point for lattice quantum many-body studies.

## 4. A Magic Optical Lattice for Yb

Optical lattices have developed into the standard tool for ultracold quantum gas experiments to reach the regime of strong correlations [4, 7, 111, 112]. They allow precise control over tunneling rates and interaction energies and opened up a dynamic research field. Based on the interference of laser beams the most straightforward design for an optical lattice is a Gaussian laser beam reflected back onto itself. Whereas such lattices are easy to implement and have enabled many successful experiments [7], more complex lattice structures open up new possibilities. A prime example for this is the triangular structured lattice formed by three laser beams intersecting at  $120^\circ$ . This structure, as well as the phase control of the individual lattice beams, allows easy manipulation of the lattice band structure by moving the lattice in real space. It was used successfully to simulate frustrated classical magnetism [113] and reconstructing the Berry curvature in a Floquet Bloch bands [23].

This chapter describes the implementation of a 3D-optical lattice for the specific needs of Ytterbium. It consists of a 1D-lattice formed by a standing wave pattern and a 2D-lattice with triangular structure. Besides its primary function as a lattice structure, the 1D-lattice needs to be deep enough to suppress any recoil momentum transfer by the clock laser (*Lamb-Dicke regime*). These and other considerations are taken into account when choosing the waists and powers of the lattice beams (section 4.1). The laser system used to distribute and control the lattice beams is described in section 4.2. The quality of the lattice beams is a prime concern because distorted wavefronts lead to distorted lattice structures. Therefore the beam shaping optics as well as their characterization is described in section 4.3. Finally, the depth of the lattice is determined using fermions as well as bosons (section 4.4) and the question whether an active fiber noise cancellation system is needed is evaluated.

The laser system, as well as the 1D-lattice beam shaping optics, were built by the author. The 2D-lattice beam shaping optics were planned by the author and built and characterized by Niels Petersen [114] and the author. The lattice was setup and characterized at the experiment by Alexander Thobe, André Kochanke, Niels Petersen and the author.

### 4.1. Design of the Optical Lattice

An optical lattice is based on interference of laser beams [112]. The interference creates spatial intensity variations on the order of the wavelength of the light. Due to the dipole

force, the atoms experience a conservative potential either localizing the atoms at the intensity maxima or minima (depending on the polarizability). The tunneling amplitude and the onsite interaction determine the dynamics of the atoms in the lattice and are controlled by the intensity of the laser beams. Additionally, the Gaussian intensity distribution of typical laser beams used for the creation of optical lattices induces an inhomogeneity of the band structure. This effect is enhanced by the optical dipole trap from which the lattice is loaded. Typically the goal for the design of an optical lattice setup is to be able to access regimes of strong interactions while simultaneously a homogeneous lattice structure is desired. Because of finite laser power these requirements contradict each other and a reasonable compromise has to be found. The effect of the inhomogeneity of the band structure against achievable depth are only two design considerations one has to consider. For the use of the excited state of Ytterbium additional considerations need to be addressed. This section will describe all of the design considerations which were considered during the planning of the optical lattice and will present the resulting lattice beam specifications.

#### 4.1.1. Geometry

Because of its versatility and the considerable experience of different experimental projects in the group [19], it was early on decided to use a combination of a retroreflected 1D-lattice and a 2D-lattice formed by three-phase coherent beams with an angle of  $120^\circ$  with respect to each other. The plane formed by the 2D-lattice beams forms a  $90^\circ$  angle with the beams for the 1D-lattice. A sketch of the setup and the resulting potential is shown in figure 4.1.

By adjustment of the polarizations of 2D-lattice beams a triangular or honeycomb lattice structure in the 2D-plane is realized. The 1D-lattice is frequency offset by 160 MHz with respect to the 2D-beams to prevent interference between the 1D- and 2D-lattice. The phase between the three 2D-lattice beams is in principle controllable and thereby a *shaking* of the lattice is possible. This can be used to induce an effective tunneling matrix element allowing to completely alter the ground state of the atoms in the lattice.

The 1D-lattice intensity around the point of minimal size of the beam and on the axis of the lattice is described by:

$$V_{1D}(z) \approx V_0 \cos^2(k_L z) \quad (4.1)$$

Here  $k_L = 2\pi/\lambda_L$  with  $\lambda_L$  is the wavelength of the lattice laser,  $z$  the position along  $k_L$ . The depth of the lattice is denoted  $V_0$  and is related to the maximal dipole potential  $U_{\text{dip,max}}$  created by the laser beam:

$$V_0 = 4U_{\text{dip,max}} \quad (4.2)$$

Thus the individual potential wells are four times deeper than the depth of the dipole potential created by a lattice laser beam without reflecting it back into itself. A factor of



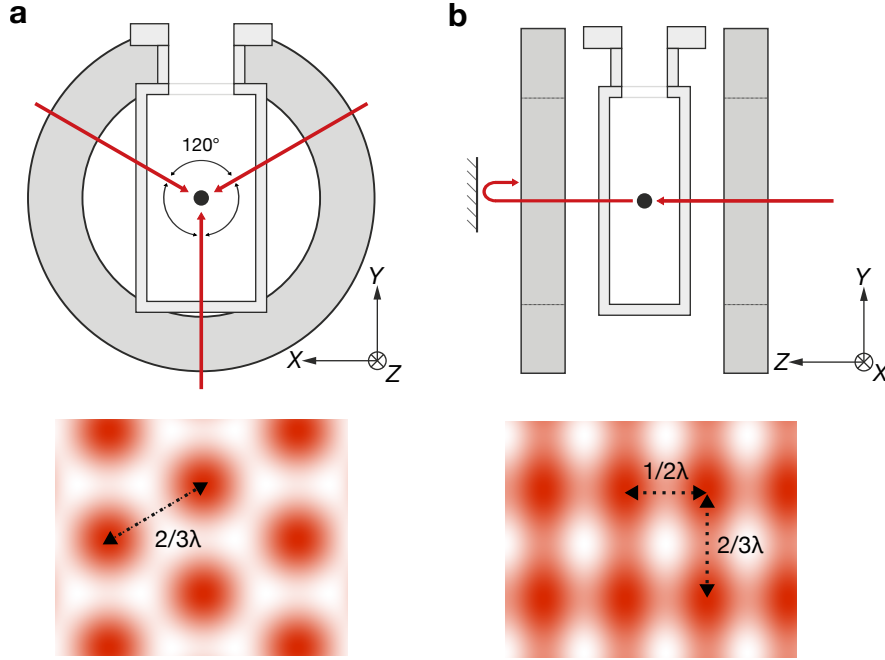


**Figure 4.1. | Schematic of the lattice geometry.** **a** The 2D-lattice is formed by three phase coherent beams intersecting at an angle of  $120^\circ$  resulting in either a triangular or honeycomb lattice structure depending on polarization of the beams. **b** The 1D-lattice is formed by one retroreflected beam. A cut through the resulting lattice structure is shown below for the 1D-lattice as well as the 2D-lattice. Image mostly taken partly from [57].

two is due to the interference and the other factor of two due to the retroreflected beam. The depth is measured in terms of the *recoil energy* and for  $\lambda_L = 759 \text{ nm}$ :

$$E_R = \frac{(\hbar k_L)^2}{2m} \approx h \times 2 \text{ kHz} \quad (4.3)$$

The 2D-lattice potential in triangular configuration (polarization perpendicular to the plane of the lattice) is described by [115]:

$$V_{2D}^\Delta(\mathbf{r}) = V_0 \left( \frac{3}{4} + \frac{1}{2} (\cos(\mathbf{b}_1 \cdot \mathbf{r}) + \cos(\mathbf{b}_2 \cdot \mathbf{r}) + \cos((\mathbf{b}_1 - \mathbf{b}_2) \cdot \mathbf{r})) \right) \quad (4.4)$$

Here  $\mathbf{b}_1$  and  $\mathbf{b}_2$  are the reciprocal lattice vectors.  $V_0$  is the depth of the lattice and is measured in  $E_R$  and is again based on the dipole potential depth of one single lattice beam. Note that the three beam lattice creates  $9/4$  deeper potential wells compared to a 1D-lattice with the same power.

### 4.1.2. Wavelength and Laser

While the wavelength of the optical lattice for Alkali experiments is mainly determined by the available laser power, the wavelength plays a crucial role when high spectral resolution of the clock transition is desired. This is easily seen when considering the differential light shift due to the difference in polarizability of the states  $^1S_0$  and  $^3P_0$ . The difference in polarizability of the clock transition leads to an intensity dependent spectral broadening according to (see section 5.4.1):

$$\delta f = -\frac{1}{h} \frac{1}{2\epsilon_0 c} \Delta\alpha_{eg} \Delta I \quad (4.5)$$

Here  $\Delta I$  is an intensity difference and  $\Delta\alpha_{eg} = \alpha_e - \alpha_g$  is the differential polarisability. When two atoms are located on different lattice sites they experience a differential intensity due to the transversal gaussian intensity distribution of the lattice beams. The differential intensity is always present in optical lattices formed by non-“flat-top” beams. Thus the broadening can only be circumvented by decreasing the differential polarisability. The wavelength where  $\alpha_e = \alpha_g$  is called *magic wavelength* and is at  $\lambda_m = 759$  nm [95] (see also section 2.3.3). It is thus desirable to operate the optical lattice at this wavelength if high precision clock spectroscopy is needed. On the other hand, the different polarizability can be actively used to generate potentials which allow the two states to experience different tunneling and interactions in the lattice (see section 5.4). For example, a lattice at a wavelength of  $\lambda > 1000$  nm could be used to induce artificial gauge fields [39].

It was therefore decided to use a laser which is able to be tuned over a large wavelength in the visible red and near infrared. An optically pumped Ti:Sa is an ideal choice because it delivers high power (here at least 3.5 W, depending on the wavelength up to 5 W) with output wavelength of 700 nm to 1030 nm.

### 4.1.3. Achievable Lattice Depth, Trap Frequencies, and Recoil Suppression

The available laser power and the waist of the lattice beams determine the achievable lattice depth. The depth is a very important quantity determining the tunneling strength as well as the strength of the interatomic interaction. The depth thus determines if it is possible to access the regime where interaction dominates the energy scales. Deep lattices are most easily achieved by creating beams with small waists. As for the optical dipole trap, this has the downside of increased average trap frequencies which will hinder loading atoms into the lowest Bloch band and distort the band structure.

While the possibility of achieving large lattice depths is desirable in general, our experimental setup demands large lattice depths for a second reason. For experiments using resonant light for atomic excitation, the strength of the confinement plays another important role. A photon exciting an atom from the ground into the excited state (e.g. excitation of the

clock state) not only transfers energy but also momentum. This could transfer the atom in an excited motional state (i.e. a higher band). The momentum transfer can be suppressed when the band spacing is significantly larger than the recoil energy [116]:

$$\hbar\omega_R \ll \hbar\omega_{nn'} \quad (4.6)$$

Here  $\hbar\omega_R$  is the recoil energy of a clock laser photon and  $\omega_{nn'}$  is the energy spacing between band  $n$  and  $n'$ . The parameters for which this condition is fulfilled is called *Lamb-Dicke* regime. It is characterized by the parameter  $\eta$

$$\eta = \sqrt{\frac{\omega_R}{\omega_{nn'}}} \quad (4.7)$$

and the Lamb-Dicke regime is reached when:

$$\eta^2 \ll 1 \quad (4.8)$$

The probability to transfer the atom into another “neighboring” motional states is suppressed by a factor of  $\eta^2$  compared to the strength of the *carrier* transition, i.e. the transition where the motional state remains unchanged. To summarize: the Lamb-Dicke regime allows the decoupling of external and internal degrees of freedom and to reach it sufficient deep trapping potentials are needed. In the setup presented in this thesis, the clock laser beam will be aligned colinear with the 1D-lattice. Thus the 1D-lattice needs to be able to reach the Lamb-Dicke regime. Above it was argued that the lattices need to be deep enough to reach strongly correlated states like the *Mott-Insulator* state. Typically for cubic optical lattices, a depth of  $20E_R$  is enough to reach this regime. A depth for the 1D-lattice of  $V_{1D} = 150E_R$  would result in  $\eta = 0.20$  while at  $V_{1D} = 50E_R$  the Lamb-Dicke parameter would still be  $\eta = 0.27$ .

#### 4.1.4. Final Design

The final design was reached by an iterative process where it was tried to incorporate all the considerations above but also respect optomechanical constraints at the experimental setup as well as available lenses for the beam shaping optics. The following design was chosen:

##### Power

In total four beams need to be supplied with laser power. Using the available power from the laser and the losses due to fiber coupling, AOM diffraction efficiency and non-perfect reflective surfaces, an estimate for the available laser power at the position of the atoms per beam is made:

$$P_{\text{tot, laser}} = 3 \times \frac{1}{\eta_{2D}} P_{2D} + \frac{1}{\eta_{1D}} P_{1D} \quad (4.9)$$

Here  $\eta_{2D} \approx 0.52$  and  $\eta_{1D} \approx 0.45$  are the efficiencies of the beam paths. A reasonable Lamb-Dicke parameter is achieved for a 1D-lattice depth of  $150E_R$ . With a beam waist of approximately  $80 \mu\text{m}$  this results in  $P_{1D} = 1 \text{ W}$  of laser power. With a total laser power of  $P_{\text{tot, laser}} = 4.5 \text{ W}$  the available power for the 2D-lattice is  $400 \text{ mW}$  per beam at the position of the atoms.

### Beam Waists

With the power estimate from above, the following waists for the four lattice beams are chosen: The 1D-lattice will be formed by a retroreflected beam with a waist of  $w_{0,1D} = 83 \mu\text{m}$ . The 2D-lattice is formed by three beams with waists of  $w_{0,2D} = 96 \mu\text{m}$ . With these powers and waists a Lamb-Dicke parameter of  $\eta \approx 0.2$  at a depth of  $V_{1D} \approx 150E_R$  is reached. The 2D-lattice in triangular configuration reaches depths of up to  $V_{2D, \text{tri}} = 50E_R$  where  $V_{2D, \text{tri}}$  is the total potential well depth.

## 4.2. Laser System

The laser used to produce the laser beams is a commercial Ti:Sa laser. The output power has to be split into the four beams for the different lattices. The optical setup for this is shown in figure 4.2. Behind the laser, the light is split into the four beam paths by polarizing beam splitters (PBS). Because of the high intensities optically contacted PBSs are used at these points in the setup.

### 1D-Beam Path

The first beam path is used for the 1D-lattice. An AOM is used for switching and active intensity regulation. The light is coupled into an optical fiber and distributed to the experiment. Because the lattice is retroreflected the beam is coupled back into the optical fiber an optical isolator is necessary to avoid back reflection into the laser cavity.

### 2D-Beam Path

The next three paths are similar and are used for the three beams of the 2D-lattice. The 2D-lattice beams need to be phase coherent with respect to each other. To suppress phase fluctuations introduced due to acoustic noise acting on the optical fibers an active *fiber noise cancellation* (FNC) system is used. It stabilizes the phase of each beam onto a local oscillator (LO). For the LO a small amount of light is picked before the light is passed through the AOM and coupled into the optical fiber. The fiber is polished flat at the end

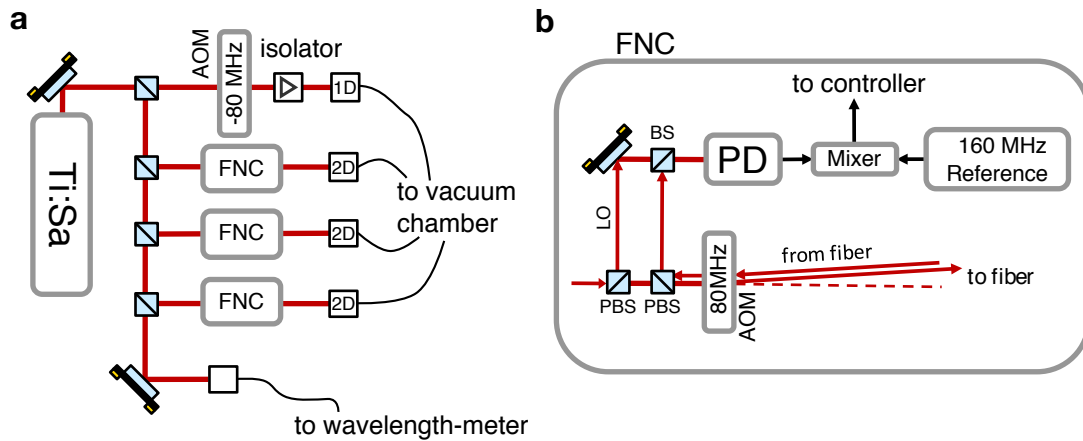


**Figure 4.2.** | **Schematic of the lattice laser system.** In **a** the principal setup of the laser system used to generate the light for the optical lattice is shown. The light is split up into the four paths for the four lattice beams and coupled into optical fibers. The 2D-lattice beams need to be phase coherent with respect to each other so an active Fiber Noise Cancellation (FNC) (shown in **b**) is used to stabilize the phase of each beam to a local oscillator. See main text for details. Image taken partly from [57].

so a small amount of light is reflected back through the fiber. It is ensured that the fiber acts as a  $\lambda/4$  waveplate thus the light reflected from the end of the fiber has a polarization turned by  $90^\circ$  with respect to the light coupled into the fiber. A PBS is used to separate the back reflected light from the incoming beam. Afterward, the LO and the back reflected light are superimposed on a photodiode. Because the back reflected light has passed the AOM two times a beat signal of two times the AOM frequency is detected by the photodiode. By using a stable reference frequency and mixing the beat signal with this reference an error signal is created. This signal is then used to change the AOM frequency accordingly. Any noise picked up by the light on the way through the fiber is thereby canceled. For more details on the FNC see [115].

### Wavemeter Beam Path

A small part of the light from the Ti:Sa is coupled into a fiber and sent to a wavelength meter. This is necessary to check whether the lattice runs as close to the desired wavelength (here the magic wavelength) as possible. It is further possible to actively stabilize the wavelength of the laser using a controller system build into the wavemeter. This control loop has only a low bandwidth (on the order of Hertz) so it is mainly used to keep the laser roughly at the same frequency. The laser by itself is specified with a linewidth of 75 kHz and is locked to single-frequency operation.

## 4.3. Beam Shaping Optics

After the light leaves the optical fibers each lattice beam needs its own set of beam shaping optics to achieve the respective waists at the correct working distance.

### 4.3.1. 1D-Beam Shaping

#### Optical Assembly

The target waist of  $w_{0,1D} = 83 \mu\text{m}$  needs to be reached at a working distance of 500 mm. The optical setup of the beam shaping telescope is shown in figure 4.3.

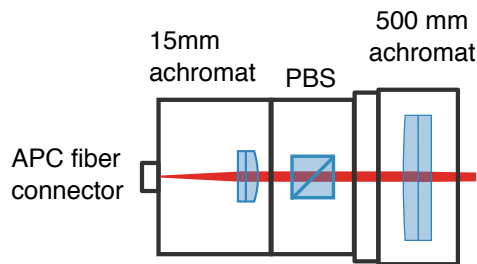


**Figure 4.3. | Beam shaping optics for the 1D-lattice.** The light is emitted from an optical fiber with an angled physical contact (APC) connector. The beam is collimated by a short wave-length achromatic lens. A PBS ensures only linearly polarized light is transmitted. A 500 mm achromatic lens focusses the beam to the desired working distance. The use of achromatic lenses minimizes spherical aberrations.

The beam shaping optics was built using a tubus system. Only two achromatic lenses were used which results in a very compact design. The first achromatic lens collimates the beam. This collimation is where the light gets diffracted the most and thus this lens will be the major source of optical aberrations. Spherical aberrations are a major concern for rotational symmetric and single wavelength beams. After the collimation, the light is passed through a PBS. The PBS ensures only linearly polarized light at the right angle is used for the creation of the 1D-lattice. The last achromat focusses the beam to the desired waist and working distance.

#### Beam Profile

After building the optical system the quality of the telescope was characterized by measuring the beam profile along the optical axis. For this, the transversal size of the beam was

determined at various points along the optical axis. For a perfect zero order gaussian mode the transversal width of the beam should evolve like

$$w(z) = w_0 \sqrt{1 + \left(\frac{M^2 z}{z_R}\right)^2} \quad (4.10)$$

where  $z$  is the position along the optical axis,  $z_R$  is the Rayleigh range,  $w_0$  the waist and  $M^2$  the beam quality factor. The beam quality factor is  $M^2 = 1$  for a perfect Gaussian TEM<sub>00</sub> mode. The measured beam profile with a fit to the equation above is shown in figure 4.4.

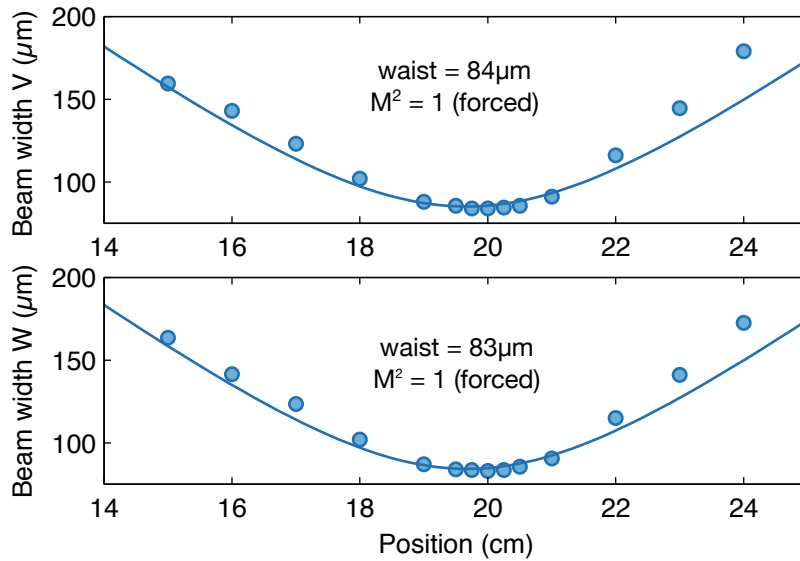


**Figure 4.4.** | **Beam profile of the 1D-lattice beam shaping optics.** Shown is the beam radius along the optical axis for the two principle directions (denoted V/W). A best fit of the profile is plotted as a solid line. A discrepancy between the theoretically expected opening of the beam left and right of the focus positions is observed. The deviation is attributed to spherical aberrations. See main text for details.

The profile shows an average waist of  $84 \mu\text{m}$  at the correct working distance. In both transversal directions, a very similar decrease and increase of the beam waist is observed which means the beam is very round over the whole measured region. This indicates very few optical aberrations due to misalignments of the beam propagation axis with respect to the optical axis of the lenses. However also a nonsymmetric opening in front and behind the focus position is observed. At the time of the characterization, it was not apparent that these deviations are a sign of spherical aberrations [117]. Because the individual transversal profiles looked very good and the waist was almost as planned the telescope was therefore built into the experiment. In retrospective, a short focal length achromat is not the best choice to collimate a high numerical aperture beam. It is apparent that the achromat used

here is working at its limit in terms of optical aberrations and should, therefore, be replaced by an aspheric lens or a multiplet with lower spherical aberrations.

### 4.3.2. 2D-Beam Shaping

#### Optical Assembly

Three beam shaping assemblies are needed for the 2D-lattice. Because of geometric constraints, one of them needs to have a slightly longer working distance (500 mm vs. 400 mm). Therefore two variants were built. Both are in principle the same optical setup but are using slightly different lenses. The setup is shown in figure 4.5.

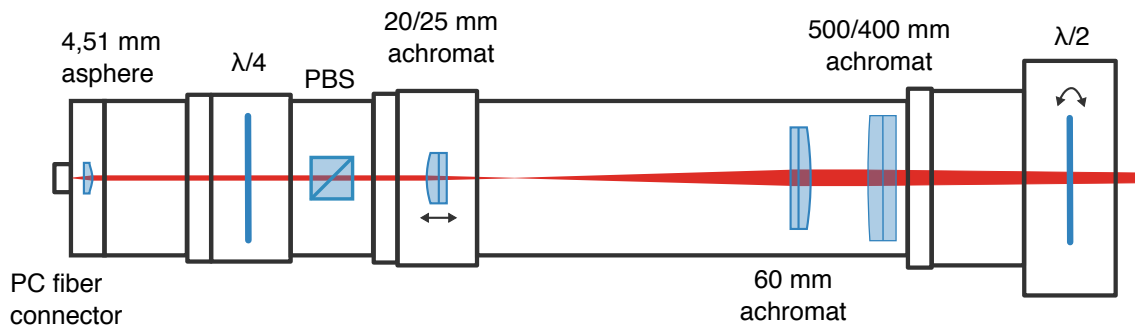


**Figure 4.5. | Beam shaping optics for the 2D-lattice.** The light from the fiber is collimated by a short focal length aspheric lens. Two achromats expand the beam which is focussed by a long focal length achromat. The light emitted by the fiber is circularly polarized which is needed for the FNC (see main text above). A quarter waveplate is placed behind the asphere to linearize the polarization. The PBS cleans any nonlinear polarized light. The last element of the whole setup is a halfwave plate which is used to set the polarization and thereby enables changing the lattice structure from triangular to honeycomb. One of the three beam shaping optic assemblies needs to be placed slightly farther away. Therefore a slightly different combination of lenses is needed. Image taken from [114].

As discussed in the previous section it was decided to use a short focal length aspheric lens to collimate the beam. This requires an additional set of lenses to expand the beam before focussing it onto the atoms. As explained before the fiber noise cancellation (FNC) system requires that the fiber acts as a quarter waveplate. A quarter waveplate is therefore put in place to linearize the polarization. A PBS cleans the light from any residual circular polarization. Next two achromats form a beam expansion telescope. Depending on which working distance is needed two different lens combinations are used. One combination expands the beam by a factor of three, the other by a factor of 2.5. A final lens focusses



the light onto the atoms. Last a rotateable half waveplate is used to change the geometry of the 2D-lattice.

### Transversal Beam Profile

As for the 1D-lattice objective, the axial beam profile as analyzed. Extensive details are found in the master's thesis of Niels Petersen [114] and here only a brief overview of the results are given.

One of the beam profiles is shown exemplary in figure 4.6. The transversal beam profile for each of the three assemblies looks fine along the optical axis. The profile along the optical axis in the region around the focus shows a good agreement between a fit of equation 3.4 and the measured profile. However, a decreasing opening angle is observed in front of the focus and behind of the focus. In contrast to the 1D-lattice objective, there is barely any asymmetry visible. It is unclear what the reason for this decrease is but spherical aberrations are the most probable cause. No off-axis errors are observed and the individual transversal beam profiles look good along the complete optical axis.

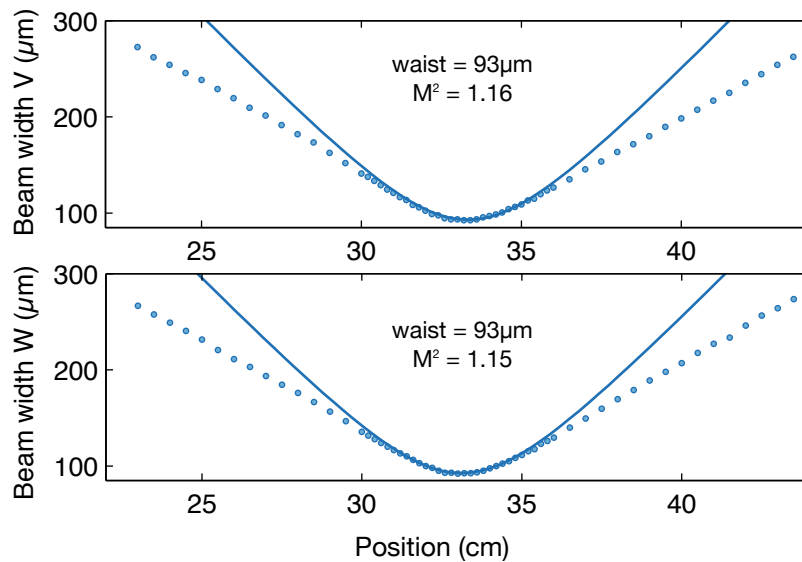


**Figure 4.6. | Beam profile of one of the 2D-lattice beam shaping optics.** Shown is the transversal beam radius along the optical axis for the two directions (denoted V/W). The waist is slightly smaller than expected. The profile around the waist agrees well with the theoretical profile. Further away from the waist the opening angle decreases.

### Phase-Front Analysis

Because of the decreased opening angle, the quality of the optics is checked by an interferometric analysis of the phase fronts.

Figure 4.7a shows the optical setup for the interferometer. After clean up of the polarization, the two beams are overlapped at a beam splitter (BS). Afterward the two ports of the interferometer are imaged onto a camera. The camera is positioned a couple of Rayleigh ranges behind the focus. One beam is passed directly onto the camera (intensity distribution called  $I_3$ ). The second port is reflected by a mirror and then passed onto the camera chip as intensity pattern  $I_4$ . A typical image obtained from this setup is shown in figure 4.7b. From this measurement it is possible to calculate the phase difference of the two beams by [114]

$$\Delta\phi(x, y) = \arcsin\left(\frac{I_3(x, y) - I_4(x, y)}{2rt(I_3(x, y) + I_4(x, y))}\right) \quad (4.11)$$

where  $r$  and  $t$  are the reflection and transmission coefficients for the beam splitter.

In figure 4.7c  $\Delta\phi$  is shown for a cut through the middle of the intensity profile along the two principal directions. The data shows strong fluctuations at the edges of the beam profile. This is attributed to the low intensities at the wings of the gaussian-shaped beams. The overall profile shows a global, slowly varying, gaussian-shaped phase difference between the two beams. This overall phase difference is explained by the different path lengths of the two beams from the BS to the camera. The beam reflected by the mirror (creating intensity profile  $I_4$ ) expanded slightly more compared to the other beam. This global phase difference can be described by applying a far-field approximation and calculating the resulting intensity distribution [114]. The dashed line shows a best fit regression of this model to the data. It is apparent that no strong phase front distortions at the center of the beam are present. Even the largest deviations at the edge of the beam remain significantly below  $\lambda/4$ .

### Conclusion of Beam Optics Characterization

This section showed the setup and the mechanical optics assembly of the 2D-lattice beam shaping optics. The transversal beam profiles are satisfactory, the longitudinal profiles show deviations from the expected trend. Subsequent analysis of the phase front of the Gaussian beams shows little distortion of the phase front at the center of the beam where most of the atoms will be trapped.

## 4.4. Integration and Characterization of the Optical Lattice

After the successful construction and external characterization of the beam shaping optics, the complete lattice was integrated into the experimental setup.

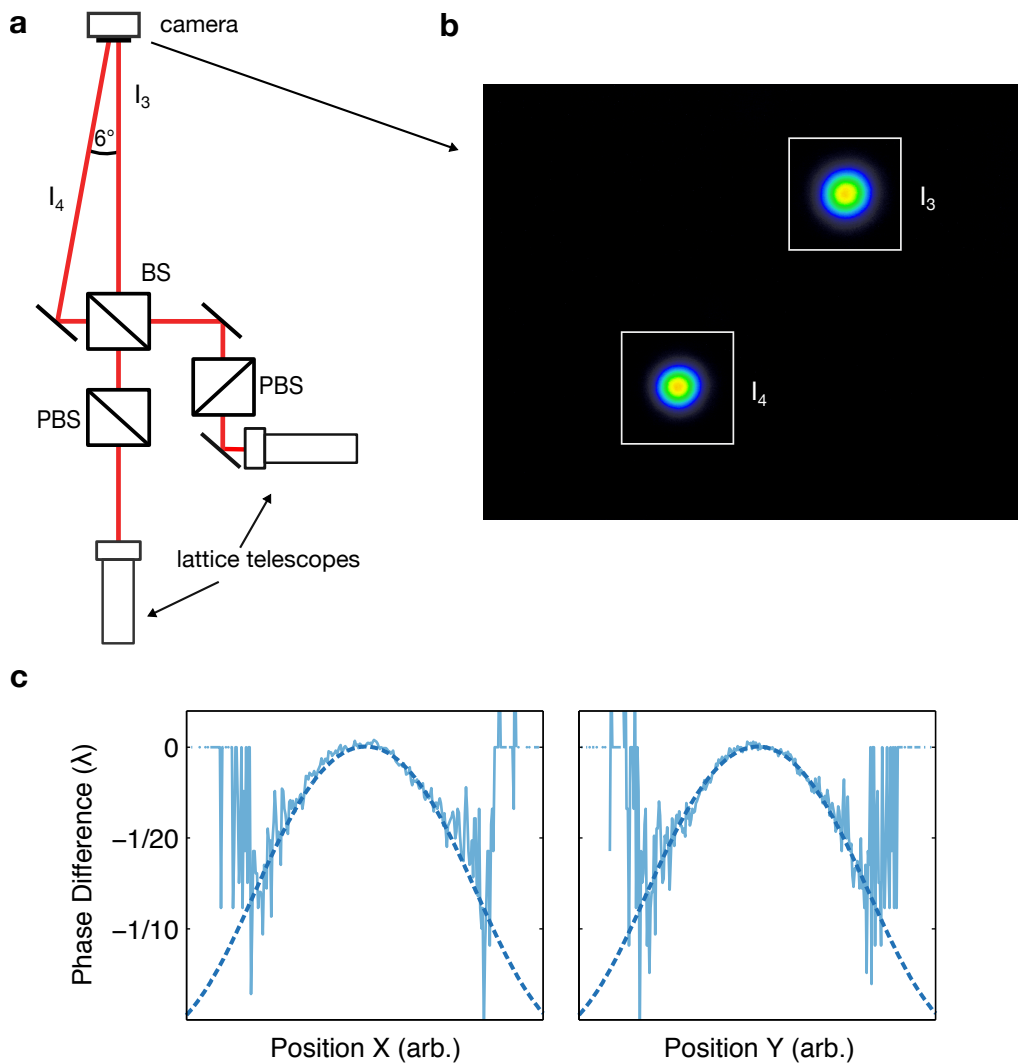


**Figure 4.7. | Interferometric analysis of the 2D-lattice phase front distortion.** The phase front distortion of the 2D-lattice beam shaping optics is analyzed using the interferometer setup shown in **a**. The two beams are overlapped at a beam splitter (BS). Both ports of the interferometer are imaged on a CCD camera (denoted  $I_3$  and  $I_4$ ). A typical image obtained from the setup is shown in **b**. By using both ports of the interferometer the overall intensity can be normalized and a phase difference between the two incident beams is calculated which is shown in **c** as a solid line. An overall phase curvature is observed which can be attributed to the different path length of the two observed beams (dashed lines). Especially the fluctuations of the phase around the center of the beam are below  $1/20\lambda$  which indicates a low distortion of the phase front. For more details see main text.

### 4.4.1. Beam Alignment and Polarization

#### Beam Alignment

All lattice beams are aligned by creating an ultracold gas (either a degenerate Fermi gas (DFG) or a Bose-Einstein condensate (BEC)) and using the lattice beam which shall be aligned to induce trap oscillations by applying a light pulse. Subsequently, the oscillations are minimized along all directions. The same procedure is used for the 1D-lattice beam while the retro reflection mirror is blocked. After the incoming 1D-lattice beam is aligned the reflected beam is coupled back into the fiber as good as possible.

#### Polarization Alignment of the 2D-lattice

All measurements in this thesis have been performed using a triangular 2D-lattice and thus the polarization of the 2D-lattice beams needs to be precisely aligned perpendicular to the plane of the 2D-lattice. To align each polarization the retroreflected 1D-lattice beam is blocked. The 1D-lattice polarization is aligned to be perpendicular to the propagation direction of the 2D-lattice beam which shall be adjusted. Therefore interference between the 1D-lattice beam and the 2D-lattice beam is possible if the 2D-lattice beam polarization is not precisely aligned to be parallel to the propagation vector of the 1D-lattice beam. By using a BEC and employing Kapitza-Dirac diffraction the interference between all three 2D-lattice beams with the 1D-lattice beam is minimized. Afterward, the 1D-lattice polarization is set back to its original setting.

### 4.4.2. Momentum Distribution of Bosons and Fermions out of the 2D-lattice

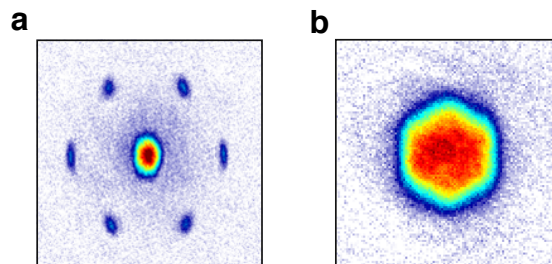


**Figure 4.8.** | Typical absorption image for bosons and fermions loaded into the triangular 2D-lattice after TOF. Shown are typical absorption images taken after cloud expansion from shallow triangular 2D-lattices. In **a** a BEC was loaded into the lattice and the characteristic momentum peaks are visible. In **b** a Fermi gas was loaded into the 2D-lattice. Because of the Pauli-principle the atoms occupy all energy states up to the Fermi-energy and thus the complete first Brillouin-zone is visible. Images are averaged over multiple experimental runs.

Figure 4.8 shows typical time-of-flight images of bosons as well as fermions loaded into a shallow 2D-lattice. The triangular structure of the underlying lattice is clearly visible. For the BEC the lattice was switched off and thus the quasimomentum states are projected onto the free momentum states. The characteristic diffraction peaks are clearly visible and indicate a superfluid state in the lattice. Fermions on the other hand occupy all energy states up to the Fermi-energy because the Pauli-exclusion principle. Here a multi component spin-mixture with  $N = 6$  spin states was loaded into the lattice. The image was taken after band mapping (band mapping time of 2 ms) which maps the quasimomentum to real momenta. The complete first Brillouin zone is clearly visible.

### 4.4.3. Lattice Depth Calibration

One of the central “tuning knobs” for the physics in optical lattices is the depth which is controlled by the intensity of the laser beams. It is therefore necessary to know and control the individual lattice depths precisely. The intensities are monitored and controlled by intensity regulation loops using photo diodes and servo controllers which control the rf-power driving the AOMs. The calibration of the lattice depth is based on resonant excitation of the atoms by lattice beam intensity modulation [118].

#### Lattice Depth Calibration with Bosons

**1D-Lattice Depth Calibration using a BEC** A BEC adiabatically loaded into the lattice occupies the lowest Bloch band and the lowest energy quasimomentum state ( $q = 0$ ). Resonant lattice modulation conserves the quasimomentum. Because of parity conservation transitions from the lowest Bloch band ( $n = 1$ ) into  $n = 2, 4, 6, \dots$  are suppressed. Therefore the lattice is modulated with frequencies resonant to the  $n = 1 \leftrightarrow n' = 3$  transition. From the number of remaining atoms as a function of the modulation frequency, a resonance frequency is obtained. By comparing the resonance frequency to a band structure calculation the lattice depth experienced by the atoms is extracted

An example of such a spectrum obtained in the 1D-lattice is shown in figure 4.9. The spectrum was measured by modulating the lattice depth with a sinusoidal shape for 100 ms with a modulation amplitude of about 1%. After modulation, the number of remaining atoms is counted. By varying the modulation frequency the spectrum shown in figure 4.9b is obtained. From the resonance position, a lattice depth is deduced by comparing with a theoretical band structure calculation as shown in 4.9a. The small asymmetry in the resonance curve is attributed to interatomic interaction which leads to a slight widening of the momentum distribution.

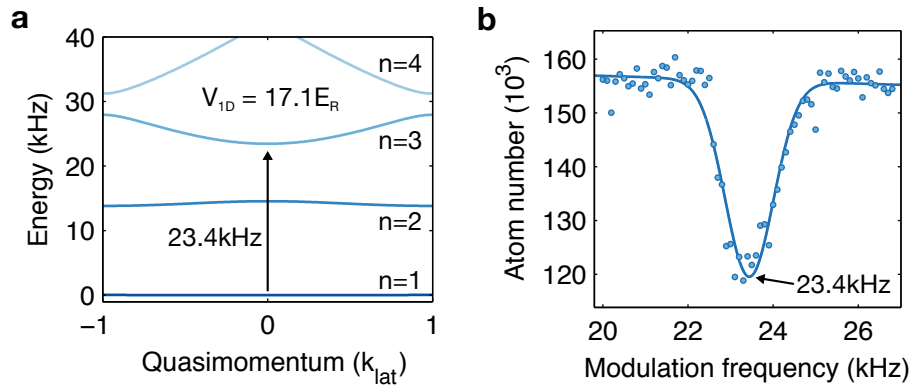


**Figure 4.9. | Band structure of the 1D-lattice resolved by lattice depth modulation.** In **a** a calculated band structure for the 1D-lattice at  $V_{1D} = 17.1E_R$  is shown. In **b** the number of atoms as a function of the modulation frequency is shown. A fit to the data is used to determine the resonance frequency (solid line).

**2D-Lattice Depth Calibration using a BEC** The determination of the 2D-lattice depth is slightly more involved because not only the total lattice depth needs to be measured but also the three beams should be equal in intensities. Therefore the three beams are calibrated in pairs forming individual 1D-lattices. The procedure for the determination of the lattice depth is similar to the procedure explained above. Sample modulation spectra for the three 1D-lattices created by the three beam pairs of the 2D-lattice are shown in figure 4.10.

### Lattice Depth Calibration with Fermions

In contrast to bosons, fermions with the same spin setting occupy not only the  $q = 0$  state but all available energy states up to the Fermi energy. Because of this, there is not a single transition frequency from one band to another but each atom sits at a slightly different quasimomentum in the band structure. There are two possibilities to circumvent this problem in the context of determining the depth of the optical lattice: The first possibility is to use low lattice depths with large band curvatures and use *momentum resolved lattice modulation spectroscopy* [119–121] and *band mapping* [111] to spectroscopically obtain the energy and momentum and therefore reconstruct the complete band structure. The second possibility is to perform the modulation at large lattice depths where effectively no band curvature is present and therefore all atoms experience roughly the same transition frequency. Subsequent counting of remaining atoms leads to resonance curves similar as seen with bosons. The two possibilities are schematically shown in figure 4.11.

In general, the first method is preferred. The method relies on reliable band mapping which means finding a band mapping time fast enough compared to the trap frequency to

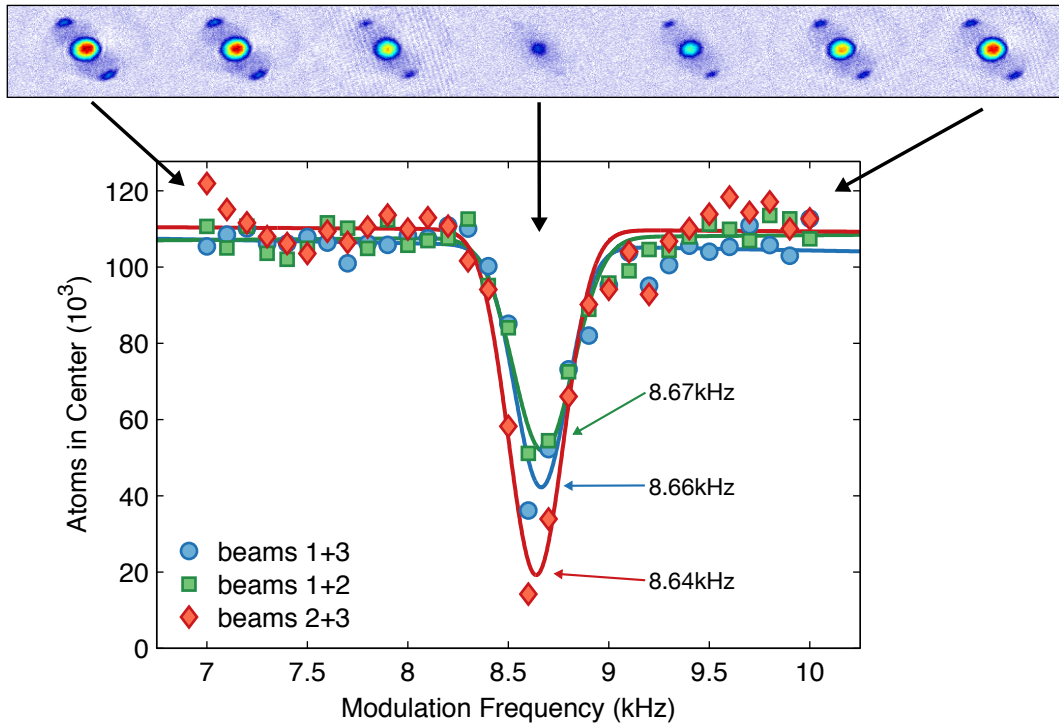


**Figure 4.10.** | **2D-lattice depth calibration and intensity balancing.** The 2D-lattice is calibrated by forming effective 1D-lattices out of pairs of lattice beams and using parametric heating to find the transition frequency into the second excited band. Here the spectra for the three beam pairs are shown after depth and intensity calibration has been performed. Taken from [114].

not destroy the momentum state and being slow enough to not wash out the momentum distribution. Unfortunately, in the 2D-lattice, it was not possible to achieve the reproducibility of the excitation and band mapping necessary to employ the first method and therefore the second method was employed. For the 1D-lattice both methods are employed: lattice modulation spectroscopy was applied to lower lattice depths (up to  $V_{1D} = 20E_R$ ) and the atom counting method was applied to deeper lattices (up to  $V_{1D} = 50E_R$ ). In figure 4.12 a typical absorption image taken at shallow lattice depths after lattice modulation spectroscopy and band mapping is shown. Spin-polarized fermions are used to suppress any interaction which could shift the resonance frequency. For the atom counting method the lattice was modulated for 5 ms and for the modulation spectroscopy a modulation time of 10 ms was used. In figure 4.13 the results of these measurements are shown and a linear fit is applied to the data (forced to (0,0)). The insets in the figure show typical data used to obtain the depth. In the left inset, which shows data obtained using modulation spectroscopy, the problems are apparent: at low and high quasimomenta it was not possible

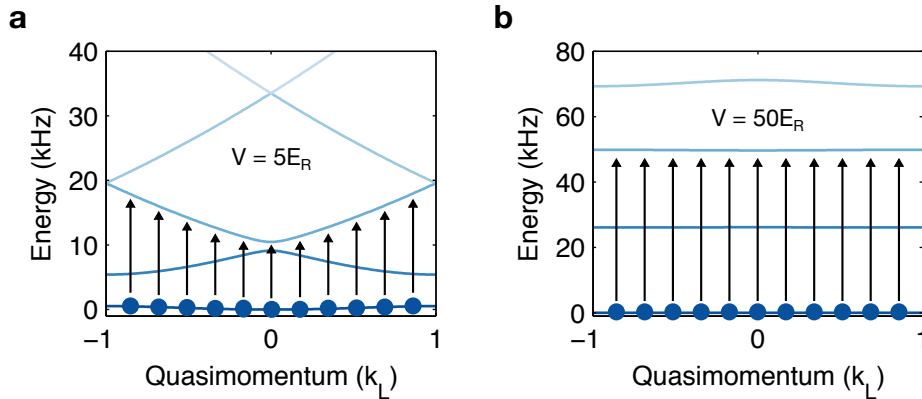


**Figure 4.11.** | **Possibilities for lattice depth calibration using fermions.** For fermions two possibilities to determine the lattice depth are available. By using momentum resolved lattice modulation spectroscopy it is possible to spectroscopically access the complete band structure which is shown in **a**. In **b** another possibility is shown where a very deep lattice leads to almost flat bands which results in a single transition frequency.

to excite enough atoms to extract a momentum. Therefore the depth was determined by fitting the slope of the 3rd band to the data. Despite the problems the calibration between the two methods fits very well and the obtained depth is within the fit error. Therefore it was concluded that both methods could be used to find the lattice depth and the atom counting method was employed for the 2D-lattice.

Both of the methods rely on modulating the lattice depth and therefore it is not possible to detect problems which result from the excitation method. The clock state of Ytterbium offers another possibility for lattice depth calibration. By addressing the clock state it is not only possible to change the electronic state but also transfer the atom into another band (*resolved sideband spectroscopy* [122]). Therefore by performing clock spectroscopy on the first *blue sideband* (corresponding to a transition into the first excited band) an independent depth determination is possible. Because of time constraints, it was not possible to employ this method.

#### 4.4.4. Characterization of the Fiber Noise Cancellation System

The fiber noise cancellation (FNC) system is used to suppress phase noise introduced by mechanical vibrations of optical components or optical fibers. The system was originally built at another experiment where the optical fibers transported the light over 30 m from one room to another. The laser system described here is located on the same optical table as the main experiment chamber. Furthermore, the optical fibers are significantly shorter



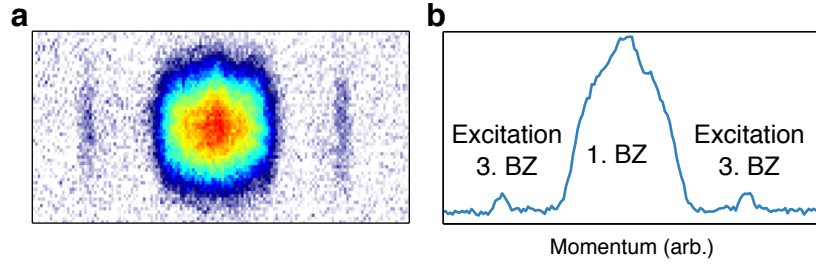


**Figure 4.12. | Lattice modulation spectroscopy.** In **a** a typical absorption image taken using ultracold fermions in the 1D-lattice after lattice modulation and band mapping is shown. In **b** a sum profile along the vertical direction of the data is shown. A small part of the atoms is excited to the second excited band (third Brillouin zone). The excitation energy is momentum dependent and thus the complete band structure is accessible. Note that no clear “holes” are present in the first Brillouin zone. The depth of the 1D-lattice is  $V_{1D} = 7E_{rec}$  and a band mapping time of  $t_{bm} = 500 \mu s$  was used.

(only 5 m) and are mechanically fixed to the optical table and experimental setup. Therefore the necessity for the FNC system is questionable.

To check whether an FNC is needed a BEC was loaded into the 2D-lattice at different lattice depths and the  $1/e$ -lifetime of the *condensate fraction* and *visibility* are extracted. The condensate fraction was determined by fitting a bimodal distribution to the central peak of the diffraction pattern while the visibility is determined by the contrast of the interference peaks. These measurements are repeated for an active FNC (analog PID servo loop with a high-quality digital reference) and a high-quality digital phase coherent source delivering the rf-signal to the three AOMs without active noise control. The lifetimes determined by this experiment are shown in figure 4.14. For both methods, a significant difference between the lifetimes is observed. In both cases, the digitally driven AOM delivers almost a factor of two longer lifetimes from a lattice depth of  $V_0 = 3E_R$  onwards. Similar behavior is observed at other experimental setups in the group. The exact reason for the lifetime increase is unknown but could be related to the fact that the analog FNC is based on a voltage controlled oscillator (VCO) which has a significantly larger instantaneous linewidth compared to the digital frequency source. Thus the FNC not only removes noise introduced by mechanical vibrations but also needs to reduce the linewidth of the VCO. Therefore the hope exists that a combination of an FNC and a digital frequency source will increase the lifetime even further. Such a digital FNC is currently in development. All measurements presented later in this thesis were performed using the digitally driven system without active FNC.

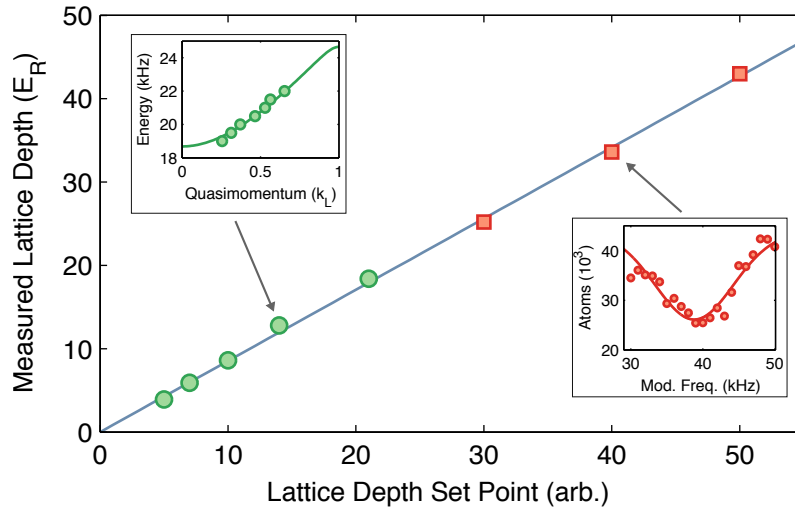


**Figure 4.13. | Comparison of lattice modulation spectroscopy and atom counting for lattice calibration with fermions.** Shown are the measured depth of the 1D-lattice obtained at various intensities. The green round data points are obtained using momentum resolved modulation spectroscopy while the red square points represent the depths obtained through excitation and counting of atoms in the 1st Brillouin zone. The solid line shows a linear fit through the data. The left inset shows data obtained through lattice modulation spectroscopy while the right inset shows typical data obtained using parametric heating and atom counting.

## 4.5. Conclusion

In this chapter, the experimental setup of an optical lattice with non-cubic symmetry was presented. The lattice consists of two substructures: the triangular 2D-lattice formed by three interfering lattice beams and a 1D-lattice perpendicular to the 2D-lattice. For both structures, the achievable lattice depth plays a significant role to reach the strongly correlated regime. Furthermore, the lattice with its axis of symmetry parallel to the clock laser beam (here the 1D-lattice) needs to achieve a sufficient Lamb-Dicke parameter. With this constraints the laser setup and beam shaping optics were planned and built. The experimentally determined beam waists corresponded reasonably well to the planned waists. However, all beams showed some signs of optical aberrations in their on-axis intensity profiles. An interferometric analysis carried out for the 2D-lattice showed only very little distortion of the phase fronts of the beams and thus were determined to be usable. Further, the techniques used for calibration of the lattice depth with fermions as well as bosons were shown. Finally, it could be determined that the active fiber noise cancellation technique at the setup presented here significantly decreased the lifetime of a bosonic sample. A digital frequency source was subsequently used to drive the AOMs used in the 2D-lattice setup.

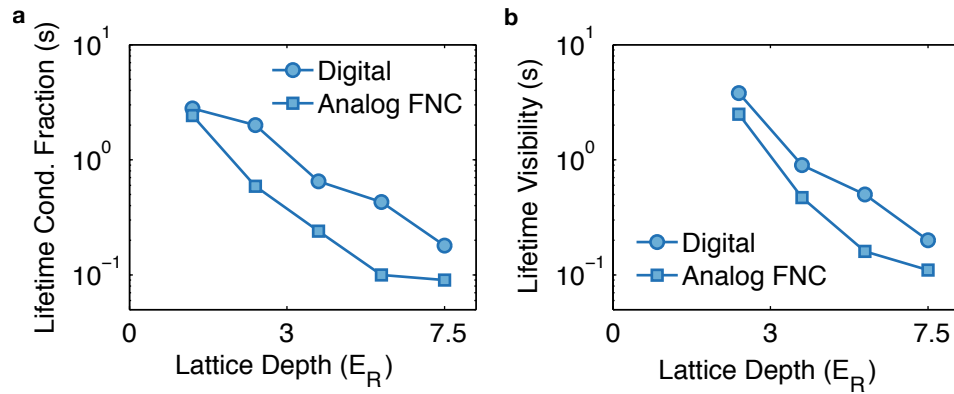


**Figure 4.14.** | **Lifetime measurement with and without fiber noise cancellation.** In **a** the  $1/e$ -lifetime of bosons in the 2D-lattice is shown determined by fitting a bimodal distribution to the central peak of the interference pattern. In **b** the same measurement is presented but the visibility of the interference peaks is plotted. In both cases the digital frequency source shows a significantly longer lifetime.

Additional characterization not relevant in the context of this thesis are described in [57] and [114]. Beside the realization of the Mott-insulator to superfluid transition [7] in the triangular lattice, the alignment of the three 2D-lattice beams with respect to each other was checked to be as close to  $120^\circ$  as possible.



## 5. Excited State Preparation and Detection

The very narrow transition connecting the ground state and the  $^3P_0$  excited state is employed for state-of-the-art optical lattice clocks [31] and can be utilized for quantum simulation of solid-state models with orbital degrees of freedom like the *Kondo-Lattice model* (KLM) [32, 33, 123, 124]. The large two-body loss rate of  $^3P_0$  atoms furthermore opens up the possibility to investigate correlated system characterized by dissipation.

The excited state is coupled to the ground state via an optical transition on the order of  $\Delta f \approx 10$  mHz. To achieve useful coupling strengths it is necessary to deliver high optical power in a comparable frequency interval. For this, a laser stabilized to a high-finesse optical resonator using a high-bandwidth servo-loop is employed. The standard method to transfer population is applying a  $\pi$ -pulse. These pulses have a total pulse area so that the probability to find all atoms in the excited state is unity. Details can be found in the PhD-Thesis of Alexander Thobe [57]. While this method is very well suited for spectroscopic measurements it has experimental drawbacks. One of the problems is the high demand on the frequency stability of the laser system. The probability of excitation depends directly on the detuning from the transition. Thus a small detuning results in nonoptimal population transfer. The second important drawback is the dependence of the pulse-time on the power of the clock-laser beam which makes precise control of the laser intensity necessary. In short: the pulse area has to be very well controlled and needs to be very stable from experimental run to experimental run.

A well-known solution to this problem is the *Rapid Adiabatic Passage* (RAP) technique [125]. A RAP coherently transfers atoms to another state by time-dependent *dressing* of the atomic states. In this thesis, the RAP is employed by sweeping the clock laser frequency over the resonance. As long as the initial detuning remains significantly larger than the Rabi-frequency and the sweep-speed remains small enough, a complete population transfer from the ground to the excited state should be achieved. In practice fluctuations in the laser power have almost no influence on the transfer probability. Similarly drifts of the laser frequency are insignificant as long as the initial and end detuning remain high enough. Notably a RAP allows population transfer of atoms in a non-magic optical lattice where due to the inhomogeneous Rabi frequencies simple  $\pi$ -pulses are difficult or impossible. Non-magic optical lattices are a cornerstone of the aforementioned KLM.

After preparation of the excited-state, it is necessary to detect the atoms. Ideally, a detection scheme which is independent of the preparation step is used to cancel imperfections in

the preparation scheme. Here a *repumper* [31, 126] is used which incoherently transfers the atoms back to the ground-state where standard absorption imaging is performed.

This chapter is organized as follows: the laser system and the important components used to address the clock state are briefly described in section 5.1. Next the detection part and the repumping-method is presented (section 5.2). Afterward the RAP on the clock transition is described in section 5.3 for a spin-polarized as well as for a spin mixture with  $N = 6$  spin states. The focus here lies on the influence of the many-body state and inelastic collisions between excited state atoms on the observed dynamics. Finally, the necessity of a RAP in non-magic optical lattice setups is discussed and parameters for the RAP in a KLM-lattice are presented in section 5.4.

The clock laser-system was built and characterized by Alexander Thobe and is described here very briefly. Details can be found in his PhD-Thesis [57]. The clock laser switching setup was implemented by the author. The repumping-system has been built by André Kochanke. The detection scheme and the RAP-scheme were implemented and characterized by André Kochanke, Thomas Ponath and the author. Numerical simulations and data analysis were performed by the Author.

## 5.1. Addressing the Clock-State

In the first part of this section the clock laser system used to address the  $^1S_0 \rightarrow ^3P_0$  transition is briefly described. The second part presents a new optical setup used to remove any Doppler shifts between the atoms and the clock laser beam due to small movements of the retro-reflex mirror of the 1D-lattice. This setup was implemented in the framework of this thesis.

### 5.1.1. High-Finesse Resonator and High-Bandwidth Control Loop

Addressing very narrow optical transitions require narrow laser sources. Typical semiconductor or solid state lasers are 10 kHz to 100 kHz broad. To reach linewidths on the order of Hz a high-finesse optical cavity is needed. The narrow transmission lines of such a cavity provide a high gain frequency discriminator. A high bandwidth servo loop controlling the frequency of the laser then narrows the linewidth of the laser down to the 1 Hz regime.

The optical cavity used in the experiment described here is a vertically mounted plano-concave cavity fabricated from “Ultra Low Expansion”-glass (ULE, trademarked by Corning Inc.) designed by the group of Hall [127]. The cavity is shielded against environmental influences (temperature and vibrations) by a vacuum-system and active and passive heat-shields. ULE has a coefficient-of-thermal-expansion (CTE) which crosses zero near

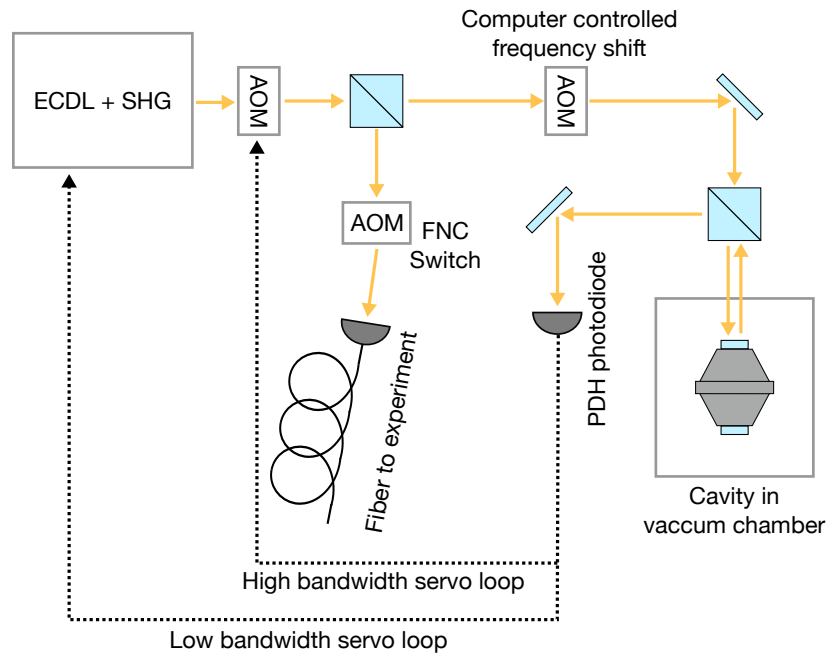


**Figure 5.1. | Important components of the laser-system used to address the clock-transition in  $^{173}\text{Yb}$ .** An frequency-doubled (SHG) External-Cavity-Diode-Laser (ECDL) is used to create laser-light at 578 nm. The laser-light is then frequency-stabilized to a High-Finesse optical cavity using a Pound-Drever-Hall (PDH) locking scheme. Fast corrections are performed via an acoustic-optic-modulator (AOM) while slow and long-term drifts are corrected by changing the ECDL cavity length. The light used at the experiment is switched on and off via an AOM which is additionally used to suppress noise introduced by the fiber-link (fiber-noise-cancellation, FNC). Another AOM in front of the reference cavity is used to control the absolute frequency of the laser-light.

room-temperature. The finesse of the cavity used in this thesis is  $\mathcal{F} = 148120$  and has a linewidth of  $\Delta\nu = 13.03$  kHz [57].

The laser itself is a commercially available, frequency-doubled (SHG) diode based system where the fundamental wavelength is amplified by a tapered-amplifier. The SHG stage is based on a non-linear crystal inside a ring-cavity and produces around 300 mW light at the clock-transition wavelength of 578 nm.

The laser is locked to the reference cavity via an *Pound-Drever-Hall* (PDH) locking-scheme [128]. The active-component is an *acousto-optic-modulator* (AOM) and a high-bandwidth “proportional-integral-derivative” (PID) controller. The servo loop has a bandwidth of 900 kHz.

Further AOM's are used to shift the frequency of the laser near the desired cavity resonance. Additional AOMs are used to control the frequency of the light used at the experiment which will be discussed in more detail in the next section. See figure 5.1 for a schematic drawing of the clock-laser setup. With this setup, it was possible to observe a laser-linewidth of 1.1 Hz on second-timescales. All further details are described in detail in [57].

### 5.1.2. Switching-Setup and Frequency-Sweeping

The part of the clock-laser system used to switch the clock-beam on and off and to dynamically sweep the clock-laser frequency for the rapid adiabatic passage (RAP) is now described. Additionally, this system allows stabilizing the phase of the clock laser beam to the reference frame of the atoms. Movements of optical elements along the path can induce a Doppler shift between the reference frame of the clock beam and the atoms trapped in the 1D-lattice. A relative movement of  $\Delta v = 100 \mu\text{m/s}$  results in a Doppler shift of  $\Delta f = \Delta v/\lambda \approx 170 \text{ Hz}$ .

The complete setup consists of three parts: the fiber noise cancellation (FNC) and switching AOM, an AOM used for frequency sweeps and an optical setup to compensate relative longitudinal movement between the 1D-lattice and clock-beam.

The complete setup is shown in figure 5.2. The FNC part is similar to the setup described in the last chapter for the 2D-lattice beams (section 4.2). It is based on a beat measurement of a local oscillator (LO) beam picked up in front of the optical fiber and a back reflected beam. The back reflected part acquires phase noise introduced by vibrations of the fiber and by vibrations of the 1D-lattice retroreflector and any optical elements in its path. If any noise is detected it is corrected by the FNC AOM using a servo loop. Because the back reflection beam is picked up near the glass cell and as near as possible to the 1D-retroreflector not only noise introduced by the fiber but also noise due to acoustics and vibrations of mirrors are compensated. The FNC AOM is also used for switching the clock beam on and off by a rf-switch.

Another AOM placed next to the experimental setup offers the possibility to dynamically change the frequency of the clock beam during the experimental cycle. The AOM is driven by a rf-synthesizer which can be controlled externally. The 0<sup>th</sup> AOM order is used for the FNC lock. A mechanical shutter is used to suppress as much light as possible in certain phases of the experimental cycle.

The clock beam passes through the concave retroreflection mirror ( $R = -600 \text{ mm}$ ). Two mode-matching lenses ( $f_1 = 1000 \text{ mm}$ ,  $f_2 = 750 \text{ mm}$ ) in front of that mirror allow adapting the spot size and shifting the focus position. For all experiments described in this thesis a spot size of  $w_0 = 200 \mu\text{m}$  was used. A polarizing beam splitter (PBS), a quarter waveplate (QWP) and a half waveplate (HWP) clean the polarisation of the beam and align it with the desired axis. In this thesis, all measurements are performed using  $\pi$ -polarized light.



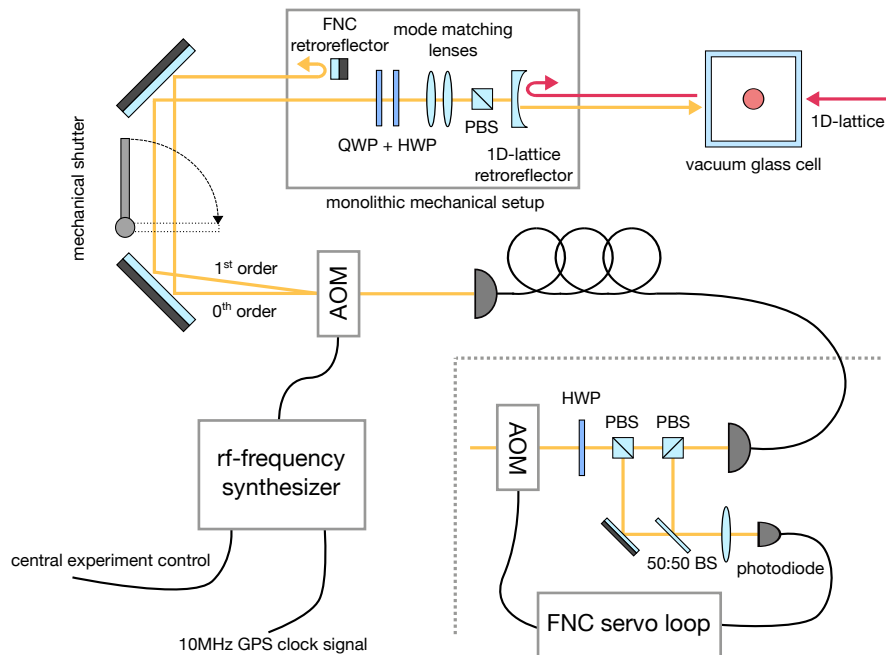


**Figure 5.2. | Schematics of the setup used to switch and sweep the clock laser beam.** The clock laser phase is stabilized to the 1D-lattice retroreflector. When the retroreflector is moving because of e.g. vibrations the fiber noise cancellation (FNC) servo loop compensates the resulting doppler shift between atoms and clock laser beam. The FNC AOM is further used for switching the clock beam. Frequency sweeps are performed via the second AOM in front of the 1D-lattice retroreflection mirror and are controlled via the central experiment control software.

The lenses, waveplates, and retroreflector are mounted on a monolithic aluminum structure to suppress vibrations of the 1D-lattice mirror relative to the FNC reflection mirror. The FNC servo loop has a servo bandwidth of approximately 100 kHz.

## 5.2. Excited State Detection

As described in the introduction a repumper is used to transfer atoms from the excited state into the ground state. In this section first the experimental setup of the repumping laser is described and then the implementation at the main experiment is shown.

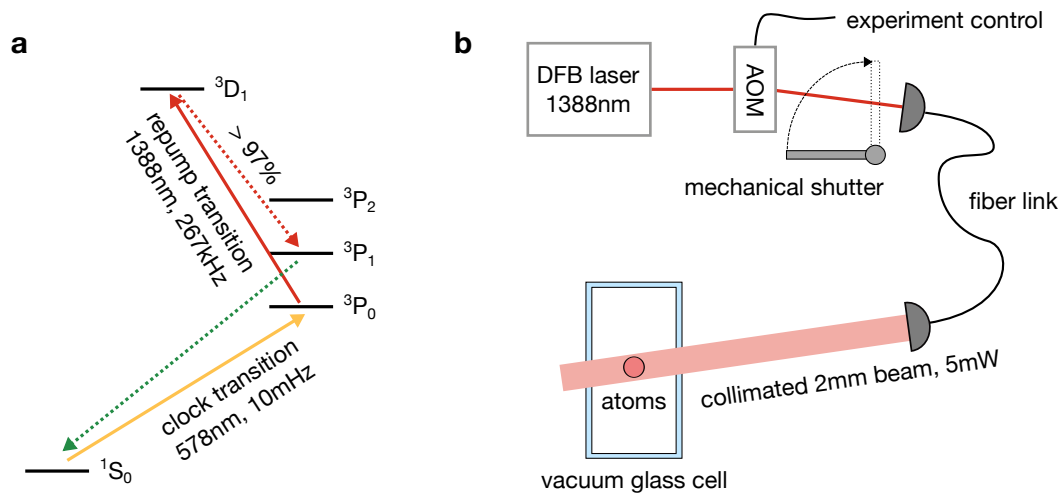


**Figure 5.3. | Repumping level scheme and laser setup.** In **a** the energy levels of  $^{173}\text{Yb}$  relevant for the repumping scheme are shown. The 1388 nm repumper pumps atoms from  $^3\text{P}_0$  to the  $^3\text{D}_1$  state from where most of the atoms spontaneously decay into the ground state via the  $^3\text{P}_1$  state. **b** shows the simple laser system used for repumping. A distributed feedback (DFB) laser emits about 10mW of light. The laser is not frequency locked. To minimize frequency drifts the DFB diode is spectrally broadened by modulating the pump current. The light is passed to the experiment via a fiber link and is directly imprinted onto the atoms. An AOM as well as a mechanical shutter allows fast switching and completely blocking the light.

### 5.2.1. Repumping Setup

The repumping transition connects the  $^3\text{P}_0$  clock state with the  $^3\text{D}_1$  level with a transition wavelength of 1388nm as shown in figure 5.3. The  $^3\text{D}_1$  state spontaneously decays into either  $^3\text{P}_2$ ,  $^3\text{P}_1$  or  $^3\text{P}_0$  with branching ratios of 0.9%, 35.4% and 63.7%.  $^3\text{P}_2$  is meta-stable and thus atoms decaying into this state are lost from the repumping cycle. Assuming a constant depopulation of all  $^3\text{P}_0$  atoms and transfer into  $^3\text{D}_1$ , a total branching ratio into the ground state of 97.5% is estimated. A complete model (which will be described in the Ph.D. thesis of André Kochanke) using rate-equations incorporating the possible transfer back to the clock state confirms this simple estimate.

The laser used for repumping is a commercially available distributed feedback (DFB) laser. It outputs about 10mW of power. The laser is free running without active frequency stabilization. The frequency is adjusted and passively stabilized by a temperature control servo loop which is set to the desired wavelength using an optical spectrum analyzer. To minimize effects of temperature drifts the laser is spectrally broadened by modulating the pump power, thereby modulating the frequency. The light is controlled by a single pass

AOM and a mechanical shutter. About 5 mW of light reach the experiment via a fiber link and is directly sent to the atoms. The beam diameter is large (about 2 mm collimated beam) compared to the atomic cloud minimizing adjustment and allowing to repump the atoms during time of flight (TOF).

### 5.2.2. Imaging sequence

The imaging sequence including the repumper consists of two steps. First, the remaining ground state atoms are imaged using normal absorption imaging on the principal 399 nm transition. This first imaging is performed after typically 15 ms TOF. The second step is the repumping stage where the repumper is activated for 1 ms. 2 ms later the next imaging is performed where the atoms which originally have occupied the excited state are imaged.

As in standard absorption imaging, two images are taken, the absorption image and the reference image allowing to normalize the intensity distribution of the imaging laser. For the repumping cycle, the ground state atoms are imaged using the first imaging pulse while the excited state atoms are recorded on the second image. This procedure simplifies the readout of the image because only two images have to be taken which allows using existing analysis software and speeds up the image transfer from camera to the computer. This simplified procedure works only if the TOF between the two clouds is large enough to separate them.

A typical image showing the ground state as well as excited state atoms are presented in figure 5.4 which shows a 50% population transfer to the excited state.

### 5.2.3. Repumper Efficiency

To check how efficient the repumping scheme is Rabi-oscillations on a spin-polarized gas of  $^{173}\text{Yb}$  were performed and it was checked whether oscillations on the sum of detected ground state and detected excited state atoms are detectable. A spin-polarized ( $m_f = 5/2$ ) sample of  $^{173}\text{Yb}$  is therefore loaded into the deep ( $V_{1D} = 50E_R$ ) optical lattice and the pulse time of the clock laser is varied. Detection of ground and excited state is performed as described above. The corresponding data is shown in figure 5.5. A Rabi frequency of  $\Omega = 2\pi \times 2.7\text{kHz}$  is extracted from damped sine fits to the data.

To check for oscillations on the total number of atoms (ground state atoms plus excited state atoms) a Fourier transform (FFT) on the data is performed. The result is presented in figure 5.6.

No oscillations at the Rabi frequency are observed. Thus the repumping process does not introduce errors in the detected number of atoms beyond the limits of our normal absorption detection. A decrease in atom number at the end of the Rabi cycle is observed which is

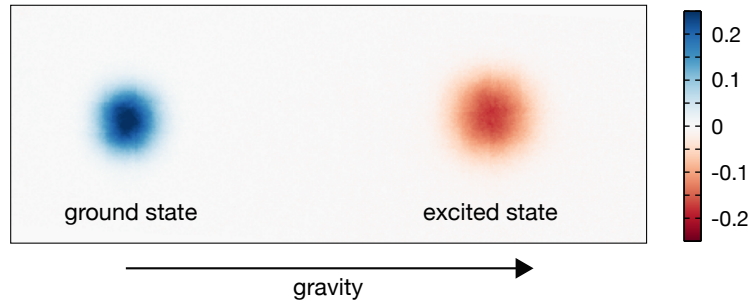


**Figure 5.4.** | Typical absorption image of atoms in  $^1S_0$  and  $^3P_0$  imaged using the repumper. The image was taken after 50% of the atoms were transferred to the excited state using a Rabi-pulse on the clock transition. Images are averaged and are only intended for illustration. Standard absorption imaging with two successive images (“absorption image” and “reference image”) was performed. The first image taken after 15 ms TOF reveals the ground state atom distribution. 1 ms repumping and further 2 ms TOF reveals the repumped excited state atoms. The excited state atoms are imaged onto the second image (“reference image”) and thus exhibit a negative optical density because the images were normalized to the “reference image”.

attributed to a drift in the experimental setup. It is observed in the FFT as a low-frequency signal.

### 5.3. Rapid Adiabatic Passage on Clock Transition

In this section the rapid adiabatic passage (RAP) in the context of optical clock transitions is discussed. First, the concept of adiabatic passages is introduced and then the implementation of the experiment is presented. Finally, the observed time dynamics of a RAP on a spin-polarized gas and a gas with multiple spin states is studied.

#### 5.3.1. Principle of Adiabatic Passages

The discussion of adiabatic passages follows [125] and [129]. The fundamental principle of a rapid adiabatic passage (RAP) is best understood in terms of a two-level atom. Assume a two-level system with eigenstates and eigenenergies according to

$$\begin{aligned}\hat{H}_A |g\rangle &= E_g |g\rangle \\ \hat{H}_A |e\rangle &= E_e |e\rangle\end{aligned}\tag{5.1}$$

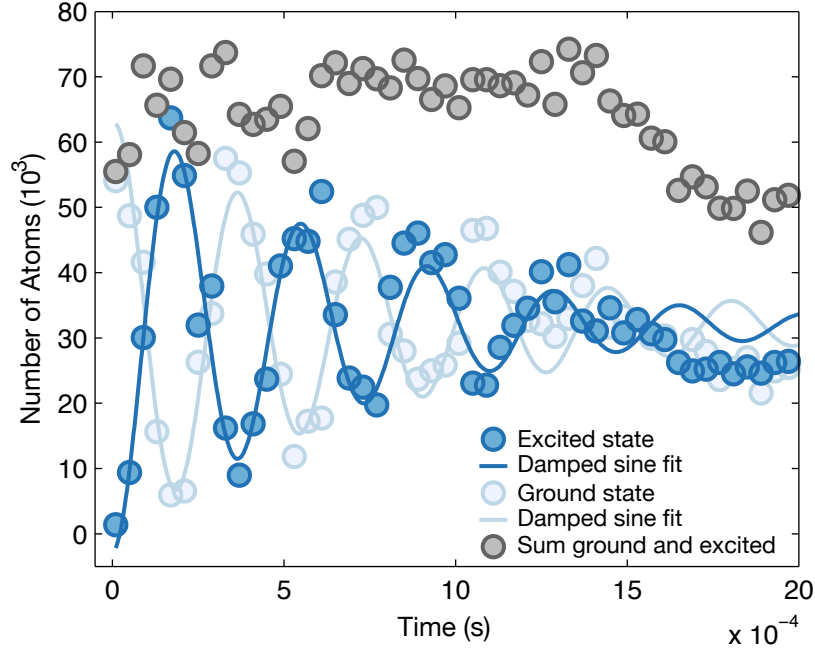


**Figure 5.5. | Rabi oscillations on a spin polarized gas imaged using the repumper.** Rabi oscillations on a spin polarized sample of  $^{173}\text{Yb}$  in the  $m_F + 5/2$  state is shown. The excited state atoms are counted using the repumper.

and a transition frequency between the states of  $\omega_0 = \frac{E_e - E_g}{\hbar}$ . The two states are coupled with a coupling strength given by the Rabi frequency  $\Omega(t)$ . The Hamiltonian describing this system in the rotating wave approximation (RWA) is written as [130]:

$$\hat{H}(t) = \frac{\hbar}{2} \begin{bmatrix} \Delta(t) & \Omega(t) \\ \Omega(t)^* & -\Delta(t) \end{bmatrix} \quad (5.2)$$

$\Delta(t) = \omega_0 - \omega(t)$  is the detuning of the photon energy  $\omega(t)$  with respect to the atomic transition energy  $\omega_0$ . Diagonalization of  $\hat{H}(t)$  yields eigenenergies

$$\begin{aligned} E_2 &= \frac{\hbar}{2} \sqrt{\Delta(t)^2 + \Omega(t)^2} \\ E_1 &= -\frac{\hbar}{2} \sqrt{\Delta(t)^2 + \Omega(t)^2} \end{aligned} \quad (5.3)$$

and eigenstates

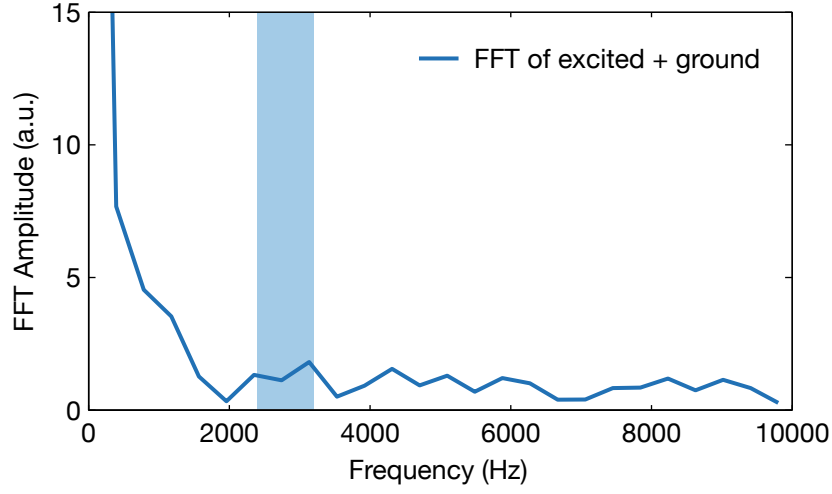


**Figure 5.6.** | **FFT spectrum of Rabi oscillations imaged using the repumper.** Shown is the FFT of the sum of ground and excited state atom undergoing Rabi oscillations. No distinct feature is observed at the Rabi frequency (blue shaded area) indicating that detection is not limited by the repumping process.

$$\begin{aligned} |2\rangle &= \sin \Theta(t) |g\rangle + \cos \Theta(t) |e\rangle \\ |1\rangle &= \cos \Theta(t) |g\rangle - \sin \Theta(t) |e\rangle \end{aligned} \quad (5.4)$$

with a mixing angle  $\Theta(t) = \frac{1}{2} \arctan \Omega(t)/\Delta(t)$ . The states  $|1\rangle$  and  $|2\rangle$  are called “adiabatic”-states while the states  $|g\rangle$  and  $|e\rangle$  are called “bare”. The condition for adiabatic time evolution is formulated by requiring that the rate of change of the mixing angle of the two states is significantly smaller than the difference of the eigenfrequencies of the adiabatic states [129] which is evaluated to [125]:

$$\frac{1}{2} |\dot{\Omega}\Delta - \Omega\dot{\Delta}| \ll (\Omega^2 + \Delta^2)^{3/2} \quad (5.5)$$

This result shows that an atom prepared in an adiabatic state will remain in this state if  $\Delta$  and  $\Omega$  are changed sufficiently slow. In particular, consider the case of an atom prepared in the bare state  $|g\rangle$  with a constant coupling strength ( $\dot{\Omega} = 0$ ). When the detuning is set to large negative values the adiabatic state  $|1\rangle$  consists mostly of the bare state  $|g\rangle$ . Slowly sweeping  $\Delta$  to large positive values keeps the atom in state  $|1\rangle$ . For large positive detunings the adiabatic state  $|1\rangle$  consists mostly of bare state  $|e\rangle$ . Thus a complete population transfer between atomic states  $|g\rangle$  and  $|e\rangle$  has been performed.

To illustrate this behavior equation 5.2 was solved and integrated numerically with a Runge-Kutta method. A constant coupling strength of  $\Omega \approx 3.8$  kHz was used and the detuning

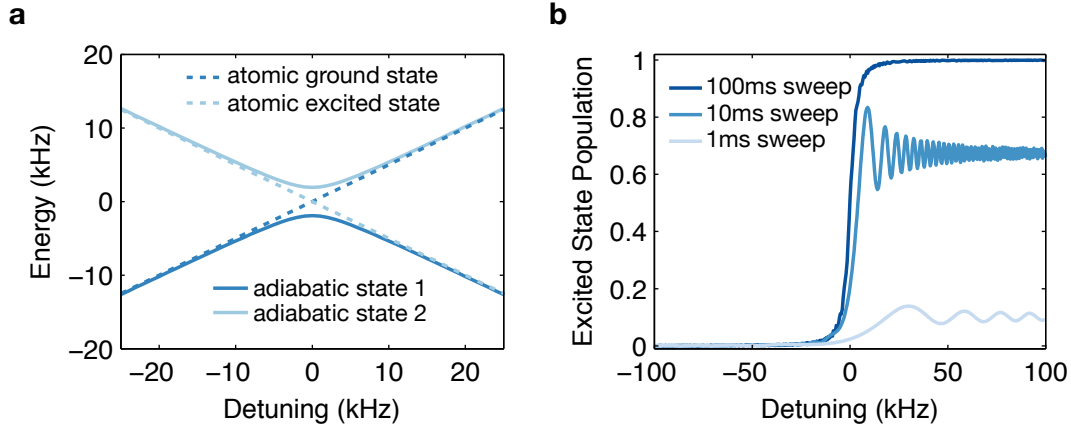


**Figure 5.7. | Rapid adiabatic passage in a two-level system.** **a** shows the energy spectrum of a coupled two-level system with a coupling strength of  $\Omega \approx 3.8$  kHz. The coupling leads to new eigenstates of the coupled system and an avoided crossing at  $\Delta = 0$ . **b** shows a numerical simulation of a RAP with constant coupling and a linear frequency sweep as seen in **a**. Initially, the system is in the atomic ground state which is mostly identical to the adiabatic state  $|1\rangle$ . If the frequency sweep is slow enough the system follows the eigenstates adiabatically and the population is transferred to the excited state. Increasing the sweep speed results in reduced transfer to the excited state and the observation of residual oscillations.

was varied between  $\Delta(t=0) = -100$  kHz and  $\Delta(t=T) = 100$  kHz. The sweep time  $T$  was varied between 1 ms and 100 ms. Equation 5.5 shows that a sweep time of  $T = 1$  ms does not fulfill the adiabaticity condition which is confirmed by the simulation shown in figure 5.7. A sweep time of 100 ms fulfills condition 5.5 showing complete population transfer from the atomic ground state to the atomic excited state.

### 5.3.2. Experimental RAP Sequence

The starting point of the RAP is a quantum degenerate gas with one or six spin components. The gas has been prepared as described in chapter 3 in the crossed optical dipole trap. A constant homogeneous magnetic field of  $B = 3$  G is applied throughout the complete sequence ensuring a well-defined quantization axis. The atoms are loaded into the magic optical lattice by first ramping up the triangular 2D-lattice thereby suppressing tunneling perpendicular to the 1D-lattice. Next, the 1D-lattice is ramped up. The depth was chosen to  $50E_R$  which yields a Lamb-Dicke parameter of  $\eta^2 = 0.07$  thus suppressing higher band transitions. After the lattice ramp, the crossed optical dipole trap is ramped down and switched off. This is necessary to prevent shifting and broadening of the clock transition. The clock laser is switched on while red detuned to  $-50$  kHz from the carrier transition. Sweeping the frequency of the clock laser frequency to higher values initiates the RAP.

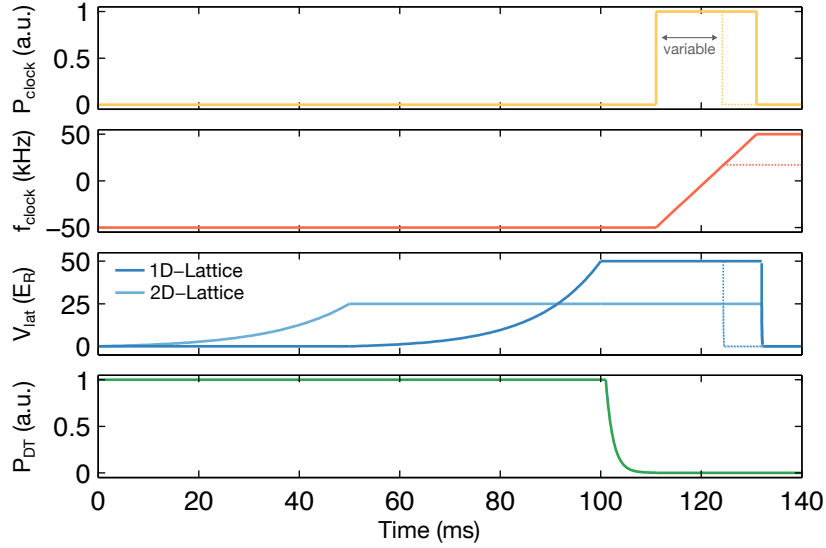


**Figure 5.8.** | **Experimental sequence of the RAP on the clock transition in  $^{173}\text{Yb}$ .** The experimental sequence for the adiabatic passage on the clock transition starts with a quantum degenerate gas of  $^{173}\text{Yb}$ . After the lattice is ramped to its final value the dipole trap (DT) is ramped down and switched off to suppress intensity dependent light shifts and broadening. The RAP is performed by switching on the clock laser and linearly sweeping its frequency. Finally, the atoms are released from the trap and the atoms are imaged using the repumper. By changing the duration of the frequency sweep and the endpoint of the sweep (dashed lines) it is possible to study the time evolution of the RAP process.

When total population transfer is needed the final frequency is +50 kHz. A sweep time of 20 ms is chosen which fulfills the adiabaticity condition 5.5 for Rabi frequencies of about  $\Omega = 2\pi \times 1\text{ kHz}$  and larger. For the RAP characterization, the passage is interrupted at certain points during the sweep thus enabling us to study the time evolution. The described sequence is illustrated in figure 5.8. Finally, the atoms are released from the trap and imaging of ground and excited state atoms as described in section 5.2 is performed.

### 5.3.3. RAP using a Polarized Gas

The above described sequence was employed using a spin polarized gas of  $^{173}\text{Yb}$  in the  $+\frac{5}{2}$  state. For this configuration a Rabi frequency of  $\Omega = 2\pi \times 3.8\text{ kHz}$  was used. All other parameters were chosen as described above. The time evolution of the population was observed in 1 ms intervals and is shown in figure 5.9.

This sequence was performed for different numbers of atoms at the beginning of the RAP by decreasing the final dipole trap power before loading the atoms into the lattice. A complete



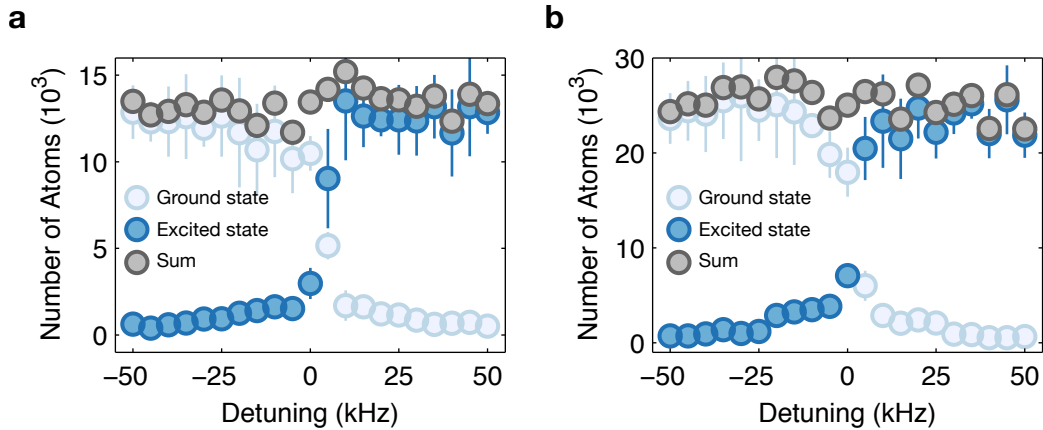


**Figure 5.9.** | RAP with a spin polarized  $^{173}\text{Yb}$  sample. **a** and **b** show excited and ground state atom numbers for a rapid adiabatic passage on the clock transition. The sweep time is set to 20 ms and all atoms are in the  $m_F = +5/2$  state. A lower initial atom number was prepared in **a** compared to **b** by decreasing the final dipole trap power before ramping up the optical lattice. Complete population transfer is observed.

population transfer from the ground into the excited state is observed as predicted by equation 5.5. The observed dynamics is independent of the number of atoms.

### 5.3.4. RAP using a Spin-Mixture

The same sequence is employed using a sample with six spin components. Equal distribution of all six spin states is assumed. All other parameters (frequency sweep time, clock beam power etc.) are chosen as before. The result of this measurement for four different amounts of atoms in the ground state at the beginning of the RAP is shown in figure 5.10.

A significantly different time behavior compared to the spin-polarized measurement is observed. The important observations are:

- For all but the lowest initial particle number, a significant difference between the remaining atoms and the initial particle number is observed.
- For the lowest particle number a small difference between initial and remaining atoms is observed while at the end of the RAP more atoms remain in the ground state, i.e. an overall worse RAP efficiency compared to the spin polarized RAP is observed.
- For the two highest particle numbers a small transfer of ground state atoms into the excited state is visible at a distinct detuning of approximately  $\Delta = -30$  kHz.

The next three sections will discuss this observation in detail.

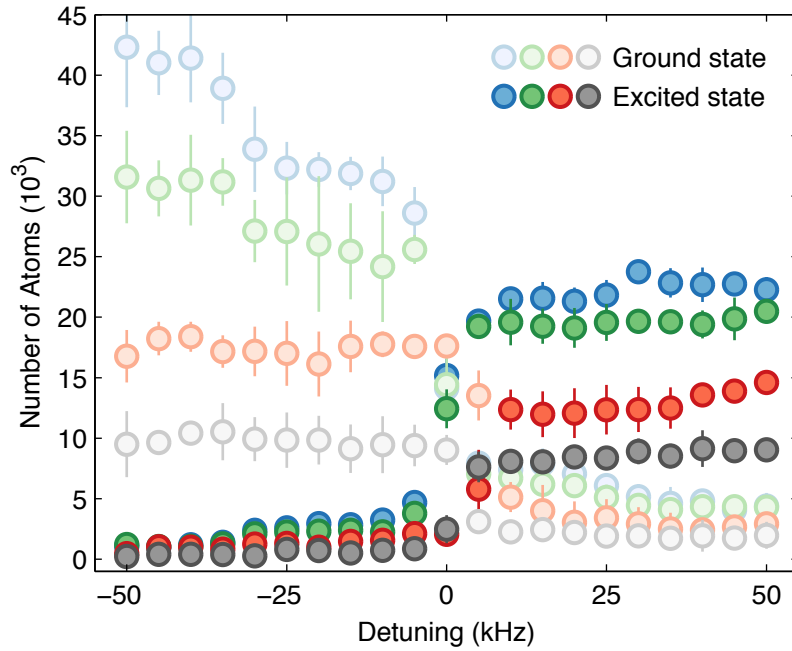


**Figure 5.10. | RAP with six spin components.** RAP on a six spin mixture of  $^{173}\text{Yb}$  for different initial particle numbers. A significant atom loss is observed for the three high particle numbers. Further a decrease in the ground state particle number at approximately  $-30$  kHz is detected. The former particle loss is attributed to double occupancies. The latter particle loss is attributed to higher-band occupations. See main text for details.

### 5.3.5. Differential Rabi Frequencies

The transition  $^1\text{S}_0 \rightarrow ^3\text{P}_0$  is addressed using  $\pi$ -polarized light so the hyperfine state of the atom is conserved. While the elastic scattering length is spin independent the  $^1\text{S}_0 \rightarrow ^3\text{P}_0$  coupling strength (Rabi frequency) depends on the particular  $m_f$  setting. Furthermore, the Rabi frequency is not only dependent on the spin state but can either be positive or negative. The relevant coupling coefficients are presented in figure 5.11b. The sign of the Rabi frequency will play a significant role when two atoms on the same lattice site are addressed using the clock laser and will be discussed in the next section. On lattice sites with only one atom only the magnitude of the coupling influences the RAP dynamics. The time behavior of the RAP on a singly occupied lattice site is simulated for the three different Rabi frequencies and the experimental parameters introduced above. The Hamiltonian from equation 5.2 is used. A term to include the linear Zeeman effect due to the applied

quantization axis is added:

$$\hat{H}(t) = \frac{\hbar}{2} \begin{bmatrix} \Delta(t) + 2Z_g & \Omega \\ \Omega^* & -\Delta(t) + 2Z_e \end{bmatrix} \quad (5.6)$$

Here  $Z_g$  and  $Z_e$  are the spin, electronic state and magnetic field dependent Zeeman energies. This Hamiltonian is time evolved using a 3rd order Runge-Kutta method with a linear detuning sweep. The simulation was performed for all coupling strengths and the propability of transferring a ground state atom into the excited state is presented in table 5.1.

Spin State	Propability of transfer	Clebsch-Gordon coefficient
$ \pm 5/2\rangle$	0.99	$\pm 0.845$
$ \pm 3/2\rangle$	0.81	$\pm 0.507$
$ \pm 1/2\rangle$	0.16	$\pm 0.169$

**Table 5.1. | Probabilities of transfer of a ground state atom into the excited state by a RAP.** The probability for transfer from the ground state into the excited state is calculated by a numerical simulation of the RAP process. Due to the different Rabi frequencies the adiabaticity condition is violated for the  $m_F = \pm 1/2$  transitions and only a low transfer probability is observed.

The results of the simulation indicate a low transfer probability for the lowest Rabi frequencies / Clebsch-Gordon coefficients. Averaging over all probabilities gives an overall RAP efficiency of 65%. For the lowest particle numbers presented in figure 5.10 RAP efficiencies of more then 80% are observed. It is currently unclear why the simulation yields worse transfer efficiencies compared to the experiment but it can be concluded that the difference in Rabi frequencies yields worse transfer probabilities and thus explains the second observation stated in chapter 5.3.4. For future experiments, the initial detuning and the sweep time of the detuning should be adapted to mitigate this effect.

### 5.3.6. Influence of Double-Occupancies on the RAP

The overall particle number dependence of the RAP efficiency is attributed to doubly occupied lattice sites as will now be explained.

#### Amount of Double Occupancies

In 5.3.4 a particle number dependent loss was observed. The loss is observed on resonance where the population changes from the ground to the excited state. This loss process is attributed to doubly occupied lattice sites where both atoms are lost when transferred

to the excited state due to inelastic scattering between excited state atoms. To confirm this the atomic distribution of the ground state of a fermionic spin mixture in the optical lattice for the experimental conditions has been performed. The simulation “sorts” each atom into the lowest available energy state of an optical lattice including the harmonic confinement induced by the lattice and dipole trap beams. No tunneling ( $J = 0$  limit) and zero temperature were assumed while interactions and the Pauli principle is accounted for. From this simulation, the number of atoms on singly occupied lattice sites is deduced. The following parameters were assumed for the calculation of the density distribution:

$$\begin{aligned}\omega_x &= 2\pi(70 + 51) \text{ Hz} \\ \omega_y &= 2\pi(24 + 51) \text{ Hz} \\ \omega_z &= 2\pi(27 + 55) \text{ Hz} \\ U &= 1.56E_R\end{aligned}\tag{5.7}$$

The harmonic frequencies stem from the confinement due to the optical dipole trap (first number in the table above) and the additional confinement due to the lattice beams (second number in the table). The interaction energy  $U$  is based on calculated Wannier functions for the complete 3D-lattice.

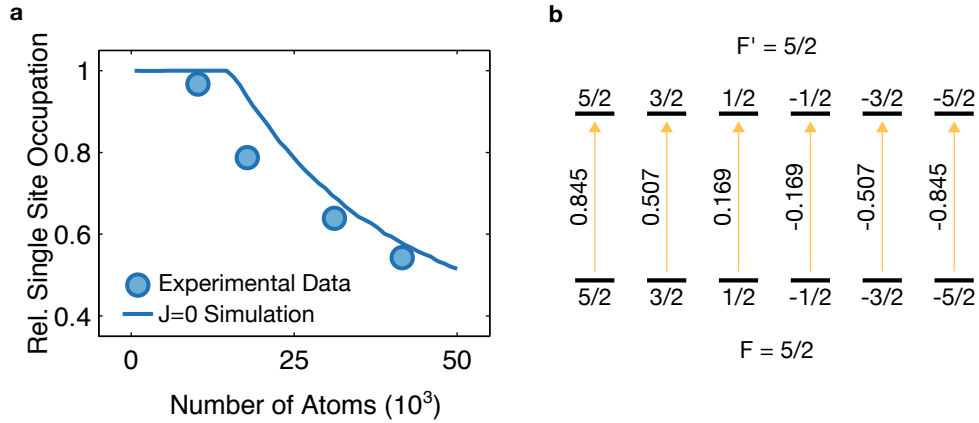


**Figure 5.11. | Singly occupied lattice sites and Clebsch-Gordan coefficients for clock transition.** In **a** the normalized number of atoms on singly occupied lattice sites depending on the total number of atoms for the experimental parameters is shown. The solid line shows a  $J = 0$  simulation while the datapoints are extracted from the measurement of the spin mixture RAP sequence. **b** shows the different Clebsch-Gordan coefficients for the  $^1S_0 \rightarrow ^3P_0$  transition of  $^{173}\text{Yb}$ .

The simulation is compared to the data of figure 5.10 by averaging the atom number of the first three ground state datapoints and the last three excited state datapoints and assuming all remaining excited atoms are on singly occupied lattice sites. The result of this analysis is shown in figure 5.11a showing good qualitative agreement. For lower particle numbers the

agreement between the theoretically expected double occupancies and the observed atom number is worse. This is understood in terms of the overall slightly worse RAP efficiency due to differential Rabi frequencies as explained in the section above.

### Two Body Interaction Hamiltonian

To solidify the assumption of inelastic scattering of excited states on doubly occupied sites playing a large role the observed behavior it was checked whether two atoms on a lattice site can be simultaneously transferred to the excited state. The time evolution of two ground state atoms on a lattice site coupled to the excited state with the RAP sequence is simulated. Here only the result of the simulation will be presented while details of the interaction Hamiltonian can be found in appendix B. The states and the Hamiltonian are also analyzed in [82] and in [57].

Starting from the Pauli exclusion principle two fermions in different spin states on a lattice site can be in either of four quantum states [82]:

$$\begin{aligned}
|gg\rangle &= \frac{1}{\sqrt{2}}(|g, \uparrow\rangle_1 |g, \downarrow\rangle_2 - |g, \downarrow\rangle_1 |g, \uparrow\rangle_2) \\
|+\rangle &= \frac{1}{2}(|e, \uparrow\rangle_1 |g, \downarrow\rangle_2 - |e, \downarrow\rangle_1 |g, \uparrow\rangle_2 + |g, \uparrow\rangle_1 |e, \downarrow\rangle_2 - |g, \downarrow\rangle_1 |e, \uparrow\rangle_2) \\
|-\rangle &= \frac{1}{2}(|e, \uparrow\rangle_1 |g, \downarrow\rangle_2 + |e, \downarrow\rangle_1 |g, \uparrow\rangle_2 - |g, \uparrow\rangle_1 |e, \downarrow\rangle_2 - |g, \downarrow\rangle_1 |e, \uparrow\rangle_2) \\
|ee\rangle &= \frac{1}{\sqrt{2}}(|e, \uparrow\rangle_1 |e, \downarrow\rangle_2 - |e, \downarrow\rangle_1 |e, \uparrow\rangle_2)
\end{aligned} \tag{5.8}$$

Here  $|e/g\rangle$  denotes the states  ${}^3P_0$  and  ${}^1S_0$  and  $|\uparrow / \downarrow\rangle$  represents one of the two spin states. The Hamiltonian  $\hat{H}(t)$  describing the system consists of an inter-atomic interaction term, an atom-light interaction term, an Zeeman-interaction term and the electronic term. No direct coupling between  $|gg\rangle$  and  $|ee\rangle$  exists while states  $|gg\rangle / |ee\rangle$  and  $|+\rangle / |-\rangle$  couple:

$$\begin{aligned}
\langle ee|\hat{H}(t)|gg\rangle &= 0 \\
\langle +|\hat{H}(t)|gg\rangle &\propto \frac{\sqrt{2}}{4}(\Omega_{\uparrow} + \Omega_{\downarrow}) \\
\langle +|\hat{H}(t)|ee\rangle &\propto \frac{\sqrt{2}}{4}(\Omega_{\uparrow} + \Omega_{\downarrow}) \\
\langle -|\hat{H}(t)|gg\rangle &\propto \frac{\sqrt{2}}{4}(\Omega_{\uparrow} - \Omega_{\downarrow}) \\
\langle -|\hat{H}(t)|ee\rangle &\propto \frac{\sqrt{2}}{4}(\Omega_{\uparrow} - \Omega_{\downarrow})
\end{aligned} \tag{5.9}$$

$\Omega_{\uparrow/\downarrow}$  is the spin state dependent Rabi frequency depending on the particular  $m_F$  transition. Figure 5.12 shows the time evolution of the transfer probabilities for a  $\frac{5}{2} + -\frac{5}{2}$  mixture with  $\Omega_{\uparrow} = -\Omega_{\downarrow}$ .

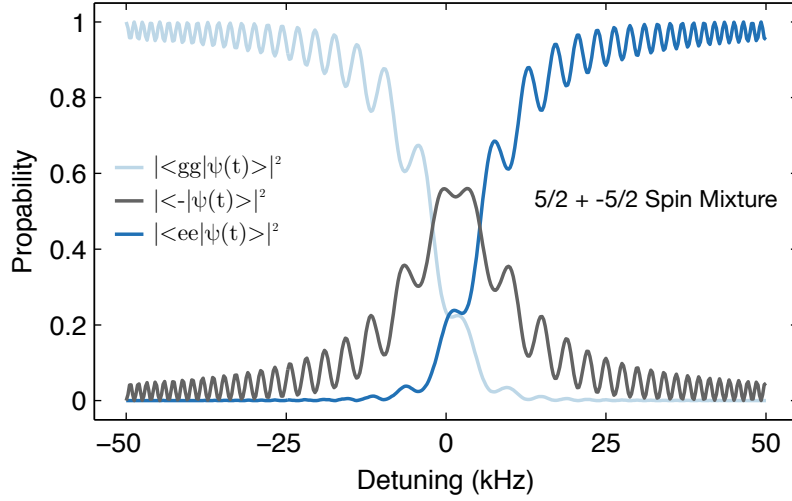


**Figure 5.12. | Simulation of RAP on a doubly occupied lattice site.** Shown is the numerical simulation of a RAP on a lattice occupied with atoms in the  $|5/2\rangle$  and  $|-5/2\rangle$  state. A complete population transfer from  $|gg\rangle$  to  $|ee\rangle$  is observed.

In figure 5.12 strong residual oscillations are visible. This is explained by the coupling strength which is increased by a factor of  $\sqrt{2}$  compared to the case of only one atom per lattice site (compare with equations 5.9). As a result, the initial detuning is not large enough for the increased effective Rabi frequency. The second observation is a complete (neglecting the residual oscillations) population transfer from  $|gg\rangle$  to  $|ee\rangle$  via intermediate state  $|-\rangle$ .

As already seen in equation 5.9 the particular dynamics and the particular intermediate state depends crucially on the difference of  $\Omega_{\uparrow}$  and  $\Omega_{\downarrow}$  but it is noteworthy that a transfer to  $|ee\rangle$  is possible for every spin state combination. For brevity figures similar to figure 5.12 for all combinations of spin states is not shown but a list the approximate probability of populating state  $|ee\rangle$  is shown in table 5.2.

As in section 5.3.5 the difference in Rabi frequencies yields very different transfer probabilities. Averaging all transfer probabilities yields a total theoretical efficiency of 66%. As before this efficiency is lower compared to the experimentally observed efficiency. This is seen very well in section 6.2.3 where RAP based measurements are presented which only use a  $5/2 + 3/2$  mixture which shows good experimental transfer efficiencies in contrast to the theoretically predicted efficiency. The reason for the difference in theoretical description and experiment is unknown. Regardless of the details, this analysis proves that a simultaneous two atom transfer is possible for every spin state combination. This means that the assumption of excited state losses on doubly occupied lattice sites leading to the sharp

Mixture	$ \langle ee \psi(T)\rangle ^2$	Mixture	$ \langle ee \psi(T)\rangle ^2$
$5/2 + 3/2$	0.15	$3/2 + -5/2$	0.99
$5/2 + 1/2$	0.77	$1/2 + -1/2$	0.17
$5/2 + -1/2$	0.99	$1/2 + -3/2$	0.79
$5/2 + -3/2$	0.99	$1/2 + -5/2$	0.98
$5/2 + -5/2$	0.98	$-1/2 + -3/2$	0.18
$3/2 + 1/2$	0.17	$-1/2 + -5/2$	0.80
$3/2 + -1/2$	0.83	$-3/2 + -5/2$	0.14
$3/2 + -3/2$	0.99	-	-

**Table 5.2.** | Probabilities of finding two atoms on a lattice site in the excited state after a RAP. Small probability variations between symmetric spin combinations are due to small numerical errors.

decrease in particle numbers is valid.

### 5.3.7. Initial Higher-Band Population

A last open question is the third observation stated in section 5.3.4. A particle loss is observed far off resonance with regard to the principal clock transition. The loss occurs at approximately  $-30$  kHz. While at the same frequency a small increase in the number of excited state atoms is visible the total number of atoms decreases at that point. For a 1D-lattice depth of  $50E_R$  the transition energy between the ground band and the first excited band is approximate 26 kHz. This corresponds reasonably well with the observed loss frequency which would indicate a small excited band population. The RAP could drive a sideband transition thereby transferring an atom into the electronic excited state and simultaneously transferring it into the lowest band of the lattice. Then a loss due to inelastic scattering between ground and excited state atoms could occur.

### 5.3.8. Summary of Spin Mixture RAP

In the last sections, a characterization of the RAP employed on a six-component spin mixture was presented. The observed dynamics is explained in terms of higher-band population, doubly occupied lattice sites and differential Rabi frequencies between the different spin transitions. While details of the behavior are not understood the overall dynamics is. Depending on the requirements of the particular experiment conducted it is necessary to limit the initial number of ground state particles in order to limit the amount of “holes” created by the loss of doubly occupied lattice sites. Here a reasonable tradeoff between

signal-to-noise and influence by the holes needs to be found. An efficient RAP on a six-spin component is possible and therefore all benefits of adiabatic passages are available.

## 5.4. RAP for the Study of the Kondo Lattice Model

The Kondo Lattice Model (KLM) is a fundamental model in solid state physics describing the interaction of localized spins with mobile spins in a lattice structure [131, 132]. It has been proposed to use atoms such as fermionic Sr or fermionic Yb as a means to study this model in a quantum gas environment [32, 33, 124]. Implementing such a model would require a mixture of  $^1S_0$  and  $^3P_0$  atoms in a state-dependent optical lattice. The lattice needs to trap  $^3P_0$  while the other component (here  $^1S_0$ ) is allowed to tunnel and would, therefore, simulate the mobile spin. The two species interact via an onsite spin exchange interaction  $V_{ex} = (U_{eg}^+ - U_{eg}^-)/2$  given by the difference in the two interaction energies between the states  $|+\rangle$  and  $|-\rangle$ .

Because the lattice depth for the two species needs to be significantly different it is obvious that the optical lattice can not be operated at the magic wavelength where both states experience the same polarisability. From figure 2.2 a wavelength region around 660 nm is identified where the above-stated requirements for the polarisability difference are found. This polarizability difference leads to a shift of the clock transition which is intensity dependent. Because of the transversal Gaussian intensity distribution of the lattice beams, every atom experiences a slightly different intensity and therefore clock transition frequency. This means excitation through  $\pi$ -pulses is very difficult. Therefore the questions arise whether an adiabatic passage can be used as a preparation tool in a non-magic lattice. To answer that questions the expected broadening of the transition line is calculated and afterward the RAP adiabaticity condition is used to find detunings and sweep times to ensure efficient population transfer. Note that an adiabatic passage is in principle very well suited for a complete population transfer. Preparing a mixture of excited and ground state atoms is more intricate and is not the focus of this section.

### 5.4.1. Broadening of the Clock Transition in a Non-Magic Lattice

The energy shift induced by a varying electromagnetic-field given in Hertz is [93]:

$$f(\alpha, I) = -\frac{1}{h} \frac{1}{2\epsilon_0 c} \text{Re}(\alpha) I \quad (5.10)$$



Here  $\alpha$  is the complex polarisability and  $I$  the intensity of the laser beam. The intensity dependent differential frequency shift of the excited and ground state is:

$$\begin{aligned}\Delta f_{eg}(I) &= -\frac{1}{h} \frac{1}{2\epsilon_0 c} (\text{Re}(\alpha_e) - \text{Re}(\alpha_g)) I \\ &= -\frac{1}{h} \frac{1}{2\epsilon_0 c} \Delta\alpha_{eg} I\end{aligned}\quad (5.11)$$

Finally the observed broadening of the transition for an intensity difference  $\Delta I$  is calculated:

$$\delta f = -\frac{1}{h} \frac{1}{2\epsilon_0 c} \Delta\alpha_{eg} \Delta I \quad (5.12)$$

The following parameters were chosen in accordance with the planned implementation of the KLM: lattice at 660 nm, lattice beam waist of 80  $\mu\text{m}$ , transversal lattice site distance of 506 nm and a power in the non-magic lattice of 200 mW. These parameters result in a lattice depth for the ground state atoms of  $26E_R$  while the excited state experiences a  $140E_R$  deep lattice. This very deep lattice is necessary to fulfill the Lamb-Dicke criterion for excitation to the excited state. The lattice would subsequently be lowered to allow tunneling in one component. For this parameters  $\delta f$  is plotted in figure 5.13.

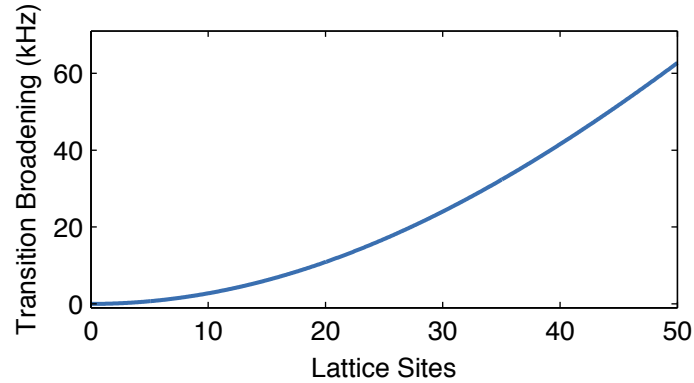


**Figure 5.13. | Broadening of the Clock Transition due to Intensity Dependent AC-Stark Shifts.** Shown is the effective broadening of the clock transition due to the Gaussian intensity distribution in a non-magic optical lattice at 660 nm. The x-axis is given in lattice sites transversal to the non-magic lattice.

Assuming a dense atomic distribution and symmetric harmonic confinement  $10^4$  spin-polarized atoms occupy about 22 lattice sites. As seen from figure 5.13 this results in a broadening of the clock transition of 13 kHz. Doubling the number of atoms results in a broadening of 20 kHz.

### 5.4.2. Experimental Parameters for a RAP in the Non-Magic Optical Lattice

Here a clock transition broadened to 20 kHz is assumed. Assuming only singly occupied lattice sites each atom has a slightly shifted resonance position but by itself experiences an undisturbed RAP. It is, therefore, straightforward to choose viable RAP parameters. Using the same Rabi frequency as before ( $\Omega = 2\pi \times 3.8$  kHz) and a linear frequency sweep the adiabaticity condition is fulfilled for a sweep span of 150 kHz and a sweep time of 30 ms. The larger span and therefore slightly slower sweep time is chosen to incorporate the shifting of the resonance position.

#### Non-Magic Lattice Preparation Summary

To conclude, a RAP in a non-magic optical lattice should not pose fundamental problems regarding the possibility of performing a complete population transfer into the excited state. However, for the KLM a mixture of excited and ground state atoms is needed. Ideally, the density of ground state atoms (“mobile spins”) can be tuned. The production of this mixture is more complicated and different initial atomic distributions (unity filling vs. half filling) and different preparation schemes ( $\pi$ -pulses, RAP) need to be explored.

## 5.5. Summary

In this chapter methods and techniques to prepare and detect  $^{173}\text{Yb}$  in the meta-stable  $^3\text{P}_0$  state using the ultranarrow clock transition and a repumping detection scheme were presented. The repumper allows reliable detection of excited state atoms with a simple experimental setup. The RAP allows the preparation of excited state polarized gases as well as excited state spin mixtures. By performing numerical simulations, limits for sweep time and sweep width due to the differential Rabi frequencies of the various spin transitions were identified. While not limiting the experiments discussed in the next chapter of this thesis small adaptations of the RAP parameters for future experiments are necessary. Further, it was shown that the RAP on a sample with inelastic interatomic losses can be used as a means to study the density distribution of spin mixtures. In the future, the adiabatic passage will most likely play an important role in preparation of the KLM or other systems relying on state-dependent optical lattice potentials.

## 6. Dissipative Dynamics with Ultracold $^{173}\text{Yb}$

Quantum gases in the laboratory are most often very well isolated from the environment which allows highly precise, controlled and reproducible experiments. In reality though, most physical systems are coupled to some kind of environment. This coupling can change the behavior of the system under study significantly. The physical mechanisms of this coupling and resulting properties of the open system are of great interest not only for fundamental studies but for applications like quantum computing [44, 45].

The study of open quantum systems using ultracold quantum gases in optical lattices is in no way straightforward. Because the creation of a quantum gas is based on reliable and strong isolation from the environment, introducing a controlled coupling to a bath poses a challenging task. Only in recent years, cold gas experiments started to investigate dissipative dynamics and decoherence. Pioneering work has been performed using ultracold bosonic molecules in 1D-optical lattices where very strong two-body losses induced particle number correlations [49], which was supported by extensive theoretical work [50]. Using fermionic molecules comparable experiments were able to show quantum Zeno dynamics and used the time evolution of the system to deduce important experimental parameters [51]. Theoretical studies further suggested the importance of multiband effects for systems with dissipation as the dominant energy scale [52]. It was proposed that dissipation can drive a fermionic quantum gas in a highly entangled spin-state [55] even for comparable high temperatures. A system with localized particle dissipation was realized using a scanning electron microscope [54].

In this chapter the experimental situation is similar to [52] where a fermi gas with very strong two-body losses in a 1D-optical lattice is studied. In the cited experiments the two-body loss rate is the dominant energy scale of the system. For the experiments presented here, the two-body loss rate is comparable to the on-site interaction so a more intricate interplay of energy scales is expected.

In section 6.1 the open quantum system under study is described from a more conceptual point of view. The experimental sequence and the experimental results are presented in section 6.2. A discussion of the data is found in section 6.2.5. In section 6.3 the lossy Fermi-Hubbard model is proposed as a way to extract information about the initial state of the system. Finally open questions and future research possibilities are discussed in section 6.4.

The experimental data described in this chapter was obtained together with André Kochanke and Thomas Ponath. The analysis was performed by the author.

## 6.1. Dissipative 1D-Fermi-Hubbard Model

### 6.1.1. Theoretical Description of Open Quantum Systems

The dynamics of a quantum system consisting of interacting fermions in a 1D-optical lattice, which is subject to two-body losses, is sketched in figure 6.1. This system can be thought of as an open quantum system where the system of interest is coupled to a bath. In this case, the bath is the continuum of motional states. The coupling between the two systems is the inelastic two-body scattering between two  $^{173}\text{Yb}$  atoms in the  $^3\text{P}_0$  meta-stable state as discussed in section 2.3.2.

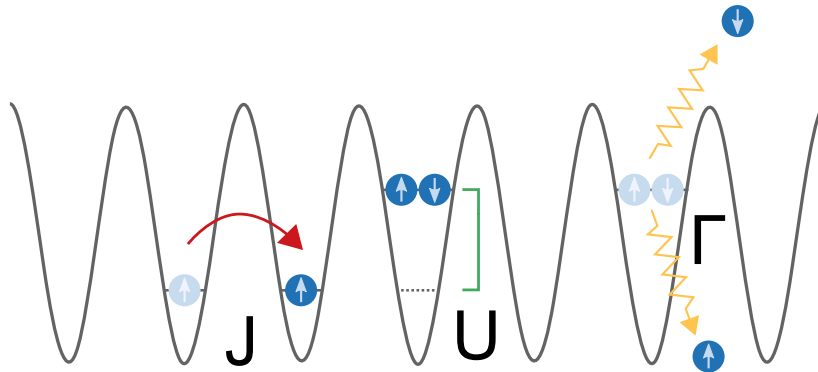


**Figure 6.1.** | Sketch of the basic processes involved in the dissipative Fermi-Hubbard model. The dynamics in the Fermi-Hubbard model with two-body losses is governed by three major energy scales sketched in the picture above: the inter-atomic interaction  $U$  for particles with different spin on the same lattice site, the tunneling  $J$  between neighboring lattice sites and a two-body loss rate  $\Gamma$ . The small arrows depict the spin of the corresponding atom.

From the description above the challenges in predicting the time evolution of this system are immediately obvious: for a full description, the Hilbert space of the complete system has to be taken into account. This quickly becomes impossible. A bath which does not retain information about the system at earlier times (*Markov approximation*, see for example [133]) allows describing the system by a master equation [133, 134] which is used in [55] to find the formation of a many-body entangled state. For the purposes of this thesis, the particle number evolution is described by a rate equation with an effective loss rate.

### 6.1.2. Effective Loss-Rate and Rate-Equation

The system under study is a 1D-Fermi-Hubbard model with onsite, two-body losses. Of interest are the particle number dynamics of such a system and the growth and decay of correlations. The three most relevant energy scales of the system are the onsite elastic interaction  $U_{ee}$ , the nearest neighbor tunneling  $J$  and the onsite two-body loss-rate  $\Gamma_{ee}$ .

The onsite interaction is given by the onsite Wannier states and scales linearly with the elastic s-wave scattering length:

$$U_{ee} = \frac{4\pi\hbar^2 a_{ee}}{m} \int |w_0(\mathbf{r})|^4 d\mathbf{r} \quad (6.1)$$

The scattering length for  $^{173}\text{Yb}$  is  $a_{ee} \approx 306.2 a_0$  [34]. The on-site loss rate is given by [51]

$$\hbar\Gamma_{ee} = \hbar\beta_{ee} \int |w_0(\mathbf{r})|^4 d\mathbf{r} \quad (6.2)$$

where  $\beta_{ee} \approx 2.2 \times 10^{-11} \text{ cm}^3 \text{ s}^{-1}$  for  $^{173}\text{Yb}$  [34]. In figure 6.2 the relevant energies for  $^{173}\text{Yb}$  in a 3D-optical lattice for the experimental parameters used throughout this chapter are shown. Atoms can tunnel along the 1D-lattice while the transversal 2D-triangular lattice remains at  $V_0^\Delta = 18.8E_R$ . This results in a the tunneling energy of 0.0066 Hz in the plane of the 2D-lattice and thus no dynamics on experimental relevant time scales is expected.

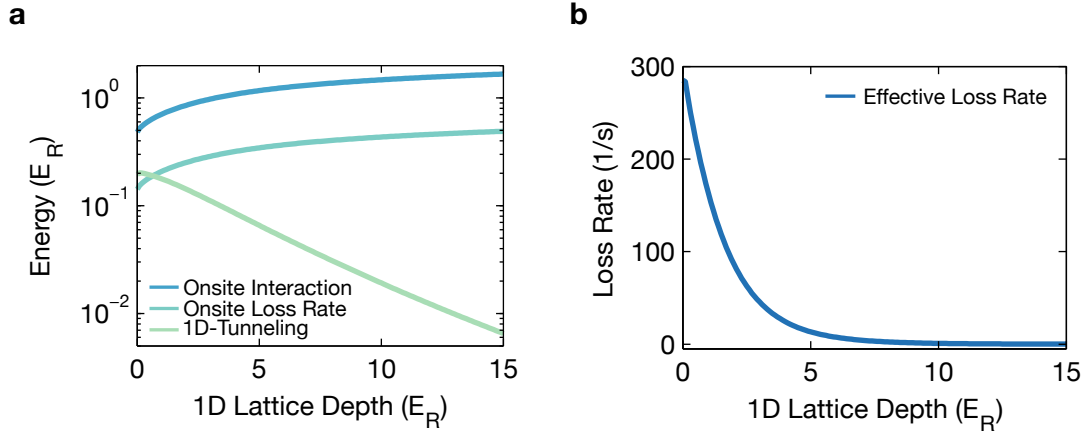


**Figure 6.2.** | Tunneling, onsite interaction, two-body loss and effective loss-rate as a function of 1D-lattice depth. **a** shows the onsite interaction energy, tunneling energy and loss-rate as a function of the 1D-lattice depth. In **b** the effective loss rate calculated from the parameters in **a** is shown. All values are calculated in a 3D-lattice consisting of a deep 2D-triangular lattice and the 1D-lattice at various 1D-lattice depths.

It is important to note that  $U_{ee}$  and  $\Gamma_{ee}$  scale exactly the same with the lattice depth. Consequently the ratio between  $U_{ee}$  and  $\Gamma_{ee}$  is constant. For  $^{173}\text{Yb}$  it is:

$$\frac{\hbar\Gamma_{ee}}{U_{ee}} = \frac{\hbar\beta_{ee}}{\frac{4\pi\hbar^2 a_{ee}}{m}} = 0.29 \quad (6.3)$$

The three fundamental energy scales influence the observed dynamics. Since particle loss is one of the fundamental processes characterizing this system, the question how many particles remain after a certain amount of time (i.e. the observed or effective loss rate) is natural. Assuming  $J \ll \hbar\Gamma_{ee}$  an effective (or *observed*) loss-rate is found [50–52, 121, 135]:

$$\Gamma_{\text{eff}} = \frac{4J^2}{\hbar^2\Gamma_{ee}} \left( \frac{1}{1 + (2U_{ee}/\hbar\Gamma_{ee})^2} \right) \quad (6.4)$$

This relation shows intriguing physics which will be discussed in the next paragraph. A plot of the effective loss rate for the experimental parameters is shown in figure 6.2.

It can be further shown that the observed particle number can be described by a rate equation of the following form [50]:

$$\frac{dN}{dt} = -\frac{\kappa}{N_0} N^2 \quad (6.5)$$

Here  $N$  is the particle number and  $N_0$  the particle number at the beginning of the loss sequence. One atom can only be lost if another atom is present. Thus  $\dot{N} \sim N^2$  in contrast to single body losses which scale  $\sim N$ . The loss coefficient  $\kappa$  is closely related to the effective loss rate introduced in equation 6.4 [51]:

$$\kappa = 4q\Gamma_{\text{eff}}g^{(2)}\eta_0 \quad (6.6)$$

Here  $q$  is the number of nearest neighbors (the experiments here are performed in a 1D-lattice so  $q = 2$ ),  $\eta_0$  is the initial filling of the lattice where the convention of  $\eta = 0.5$  for one particle per lattice site is adopted.

The nearest neighbor correlation function

$$g^{(2)} = \frac{\langle \hat{n}_i \hat{n}_j - 4\hat{\mathbf{S}}_i \hat{\mathbf{S}}_j \rangle}{\langle \hat{n}_i \rangle^2} \quad (6.7)$$

plays an important role in the observed loss process. It describes the influence of spin correlations between neighboring lattice sites ( $\hat{\mathbf{S}}_i$  is the spin operator at site  $i$ ) and particle number correlations ( $\hat{n}_i$  is the number of atoms at site  $i$ ) on the evolution of the particle number. For the case of a Mott-insulator state without any spin correlations  $g^{(2)} = 1$ . In a Mott like state where each other lattice site is empty  $g^{(2)} = 0$  which is also the case for

a spin polarized band isolator. With equal amounts of spin up and down and each spin up sits next to a spin down  $g^{(2)} = 2$ .

Assuming a time independent loss coefficient  $\kappa$ , i.e. a time independent  $g^{(2)}$  a simple analytical solution for the rate equation 6.5 exists:

$$N(t) = \frac{N_0}{1 + \kappa t} \quad (6.8)$$

In general one can not assume that the correlations remain constant when the system is allowed to tunnel. Through interactions and losses, correlations will start to build or change. In figure 6.3a three numerical solutions to equation 6.5 are shown. One curve depicts a constant  $g^{(2)}$  (no change in the nearest neighbor correlation function) and thus shows the behavior of equation 6.8. The other example assumes exponential decay of  $g^{(2)}$  according to

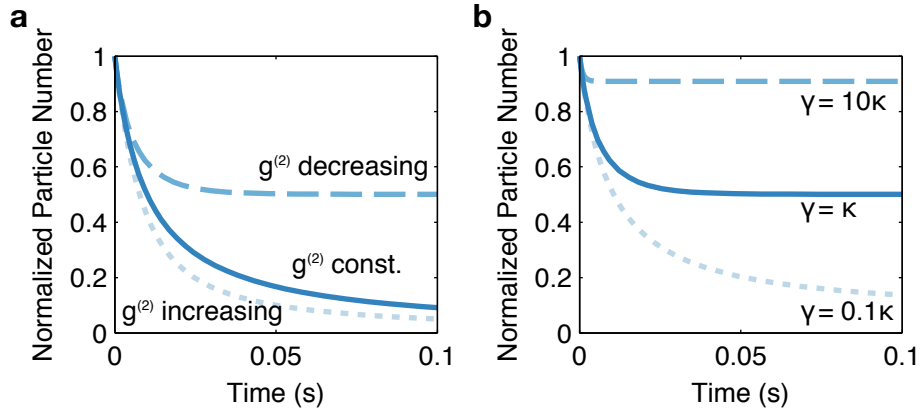


**Figure 6.3.** | Time evolution of the particle number found in a dissipative lattice model. In **a** numerical solutions to the rate equation 6.5 for time dependent and time independent correlation functions are shown. **b** shows a exponentially decreasing  $g^{(2)}$  for different timescales of correlation function decrease.

$$g^{(2)}(t) = \exp(-\gamma t) \quad (6.9)$$

while the last example shows exponential growth:

$$g^{(2)}(t) = 2(1 - \exp(-\gamma t)) \quad (6.10)$$

All three examples assume arbitrarily  $\gamma = \kappa = 100\frac{1}{s}$ . One can clearly observe the significant influence of the correlations on the observed loss dynamics. In figure 6.3b the solution to

equation 6.5 for an exponentially decaying  $g^{(2)}$  is plotted for different values of  $\gamma/\kappa$ . For a slow decrease of  $g^{(2)}$  the number of atoms decreases faster while for a fast correlation function decrease the number of atoms are lost slower. Thus the number of atoms remaining in the system is a measure of the buildup of nearest neighbor particle and spin correlations.

### 6.1.3. Mott-Insulator vs. Zeno-Insulator

The effective loss rate introduced in equation 6.4 depends on the onsite elastic interaction as well as the inelastic scattering properties and the tunneling parameter. Two limiting cases are instructive to consider. In the case of strong elastic onsite interaction  $U \gg \Gamma$  equation 6.4 reduces to:

$$\Gamma_{\text{eff}}^U = \frac{J^2 \hbar \Gamma}{\hbar U U} \quad (6.11)$$

This limit shows an effective loss rate which gets smaller with larger onsite interaction. This means that the two-body loss is suppressed by the creation of Mott-Insulator like particle correlations. The effective loss rate scales with  $J^2/U$  because  $\hbar \Gamma/U$  is constant for varying lattice depths.  $J^2/U$  is now the dominant time scale for the observed losses.

In the case of very strong losses  $\Gamma \gg U$  the effective loss rate becomes:

$$\Gamma_{\text{eff}}^\Gamma = \frac{4J^2}{\hbar^2 \Gamma} \quad (6.12)$$

In this regime, the observed losses are again suppressed but this time the physical mechanism can be understood in terms of quantum Zeno-like dynamics. The continuous measurement of particle correlations inhibits tunneling [47, 48] and forces the system in a state with one particle per lattice site. Note that both limits scale equally with the depth of the lattice. To check whether the system is in one or the other regime can thus only be checked by scaling  $U$  or  $\Gamma$  individually.

The effective loss-rate for various two-body loss rates  $\Gamma$  is plotted in figure 6.4. The two regimes described above are clearly visible and separated by a maximum of the observed loss-rate at  $\hbar \Gamma/U = 2$ . For  $^{173}\text{Yb}$   $\hbar \Gamma/U = 0.29$  and thus the dynamics for  $^{173}\text{Yb}$  are expected to be dominated by a Mott-insulator like behavior.

## 6.2. Experimental Realization of a Dissipative-Fermi Hubbard Model

This section presents the experimental results for the dissipative Fermi-Hubbard system. In section 6.2.1 the experimental procedure is described while the experimental results are presented in section 6.2.3. In section 6.2.2 a lifetime measurements of a spin-polarized gas



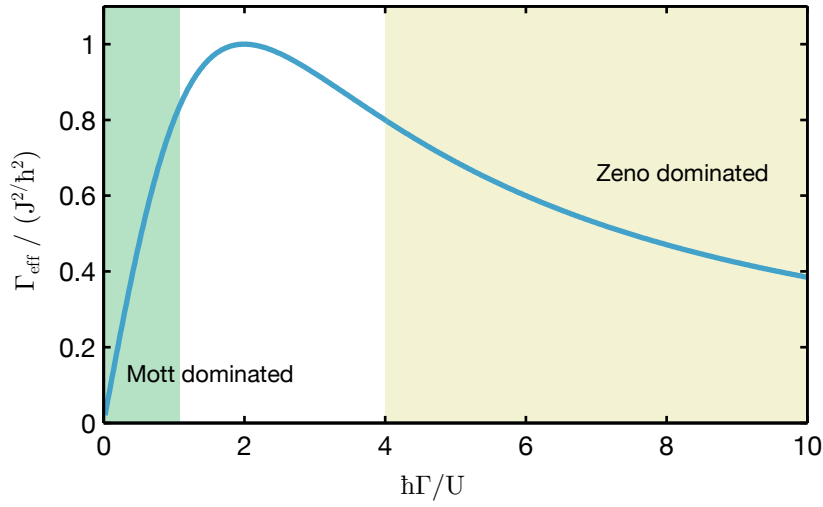


**Figure 6.4. | Effective loss rate.** Shown is the effective loss rate for variable strength of the two-body loss rate  $\Gamma$ . Two kinds of loss-rate suppression regimes can be distinguished: For loss-rates small compared to the onsite interaction the observed loss-rate is reduced due to the repulsive onsite interaction which drives the system in a correlated Mott-state. For very strong two-body losses the system is again driven into a correlated, lossless state due to the continuous quantum Zeno effect. The maximum loss rate is observed at  $\hbar\Gamma/U = 2$ .

is used to characterize the behavior of the system without the presence of two-body losses between excited state atoms.

### 6.2.1. Experimental Procedure

In this section, the experimental implementation of the dissipative Fermi-Hubbard model is described. The description of most of the techniques will be kept brief and details can be found in the corresponding chapters of this thesis.

#### Quantum Gas

All experiments presented here are performed using an ultracold fermi gas of  $^{173}\text{Yb}$ . The gas is created with  $N = 1$ ,  $N = 2$  or  $N = 6$  spin components with temperatures of about  $T/T_F = 0.25$ . Details of the creation of the gas can be found in section 3. The total number of atoms was chosen to  $N_0 = 18.000$ . This number is a compromise between the number of doubly occupied sites and signal-to-noise (compare with chapter 5). A small vertical magnetic field of  $B_y = 3\text{ G}$  is applied throughout the whole experimental sequence to provide a defined quantization axis.

## Preparation

The preparation scheme is described in detail in chapter 5 and is based on the rapid adiabatic passage (RAP) scheme. The preparation starts by ramping into a very deep 3D-lattice ( $V_{1D} = 50E_R$ ,  $V_{2D} = 18.8E_R$ ). The 2D-lattice is ramped up first during a time of 50 ms. Afterwards the 1D-lattice is ramped up in 50 ms to a depth of  $V_{1D} = 50E_R$ . Due to the very deep lattice the atoms are in a Mott-Insulator state with about 20% double occupancies for the  $N = 2$  and  $N = 6$  spin component case. A 20 ms clock laser frequency sweep ( $\Delta = \pm 50$  kHz) on the clock transition transfers the atoms into the excited state. See section 5.3.4 for details.

## Lattice Geometry

The dissipative dynamics is initiated by ramping down the 1D-lattice to a finite value where a significant tunneling matrix element exists but the condition of  $\Gamma_{ee} \ll J$  is fulfilled (see section 6.1.2). Here, this means a 1D-lattice depth of at least  $V_{1D} = 3E_R$  (compare with figure 6.2). The 2D-lattice is kept at a deep value with a tunneling rate of  $J_{1D}/h = 0.0066$  Hz. There are two reasons to keep the 2D-lattice deep: first, the 2D-lattice is needed to hold the atoms against gravity. Second, a deep 2D-lattice compresses the wannier-function and thus increases the bare loss-rate. The 1D-lattice ramp down time is chosen to  $t_{\text{ramp}} = 300 \mu\text{s}$ . This very fast ramp assures no losses occur during the ramp while minimizing higher band occupation through induced inter-band transitions. Note that such short ramping times will induce breathing modes in the trap for shallow 1D-lattices ( $V_{1D} < 5E_R$ ) and higher band population can not be avoided completely.

## Time Evolution and Detection

After the 1D-lattice ramp, the system is allowed to evolve in time. After the time evolution, the complete lattice is ramped down and the atomic cloud is allowed to expand freely. The number of atoms in the ground state is counted by absorption imaging. Repumping the excited state atoms into the ground state and successive imaging allows counting the excited-state atom number as described in section 5.2.

### 6.2.2. Lifetime of a Polarized-Fermi-Gas in the Excited-State

In all measurements effectively the reduction of the lifetime of the sample relative to the “natural” lifetime of the atoms in the optical lattice is measured. Thus it is important to understand the fundamentally limiting timescale of the lifetime of excited state atoms. In figure 6.5 the lifetime of spin-polarized ground state atoms and spin-polarized excited state atoms is shown. A rather long lifetime of  $\tau_g \approx 18.5$  s for the ground state atoms is measured.

A simple exponential decay is used to determine the value for  $\gamma_g = 1/\tau_g = 1/18.5\text{ s}$ . The lifetime for the excited state is  $\tau_e = 2.3\text{ s}$ . Additionally, a transfer of atoms from the excited state into the ground state is observed. This ground state atom growth is approximated by a simple exponential growth:

$$N_g^{\text{RAP}}(t) = N_0 \left(1 - \exp\left(-\gamma_g^{\text{RAP}} t\right)\right) \quad (6.13)$$

The following rates are extracted from the data:

$$\begin{aligned} \gamma_e^{\text{RAP}} &= 0.428/\text{s} \pm 0.123/\text{s} \\ \gamma_g^{\text{RAP}} &= 0.228/\text{s} \pm 0.020/\text{s} \\ \gamma_g &= 0.054/\text{s} \pm 0.034/\text{s} \end{aligned} \quad (6.14)$$

Here the subscript ‘‘RAP’’ indicates whether a RAP has been performed before the atoms were counted.  $\gamma_g$  is the ground-state loss rate obtained from the measurement without a transfer of atoms into the excited state.

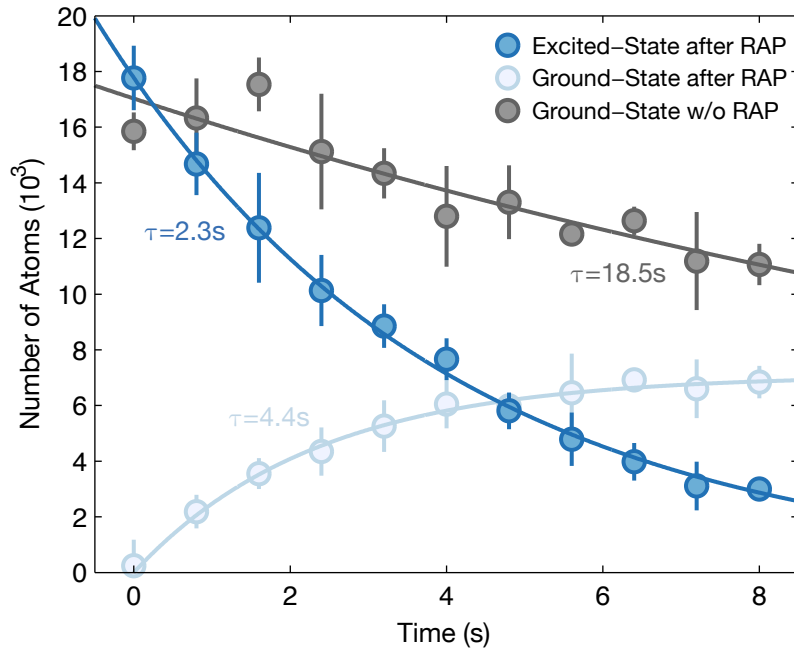


**Figure 6.5. | Lifetime of a spin-polarized gas in deep 3D-lattice.** The lifetime of ground- and excited-state atoms for a spin-polarized gas with and without a transfer to the excited state by RAP. Additionally exponential decay regressions are performed and their corresponding  $1/e$ -lifetimes are given. See main text for details and discussion.

A significantly lower lifetime of the excited state compared to the ground state atoms is observed. This lifetime is also smaller than the lifetime of the excited state for a free atom which is on the order of tens of seconds. The reduction of the lifetime is attributed to the influence of the electromagnetic field of the lattice laser beams. The atoms are trapped by the dipole force which is based on the mixing of energy states. While small this mixing effectively lowers the lifetime of the atoms.

The excited state atoms are not lost from the trap but decay into the ground state. This is seen by the growth of ground state population. The rate of ground state population growth is smaller than the decay of the excited state into the ground state. This is explained in terms of density losses resulting from the inelastic collision of excited state atoms and atoms decayed from the excited state into the ground state: after a decay into the ground state, the atoms are no longer in the same quantum state. Tunneling between lattice sites is therefore allowed. A ground state atom and an excited state atom can scatter inelastically (see section 2.3.2) and both are lost from the trapping potential.

To conclude: the dynamics of the atom number is governed by three different processes:

- Excited state atoms decay into the ground state.
- Inelastic scattering of ground and excited state atoms.
- Ground and excited state atoms loss due to single particle processes (e.g. background gas collisions).

These processes are simulated by a rate-equation model which incorporates onsite density dependent loss between excited-state and ground-state atoms. The model consists of two coupled differential equations.

The first equation describes the time evolution of the number of excited state atoms  $N_e$ . It assumes a single-particle loss due to decay into the ground-state with a rate  $\gamma_e$ . Further, it is assumed that the excited state atoms are lost from the trap due to the same processes which remove ground-state atoms from the trap. This single particle decay is incorporated by a term with the rate  $\gamma_g$ .  $\gamma_g$  is taken from the fit as shown in equation 6.14. The last term describes inelastic scattering between ground- and excited-state atoms (i.e. a density term):

$$\frac{dN_e}{dt} = -\gamma_g N_e - \gamma_e N_e - \gamma_{eg} N_e N_g \quad (6.15)$$

The second rate equation describes the number of ground-state atoms. Atoms from the ground state are lost by single-particle decay with a rate  $\gamma_g$  and two-body losses between ground and excited state atoms as before. The gain of atoms from the decay of the excited state is modeled with the rate  $\gamma_e$ :

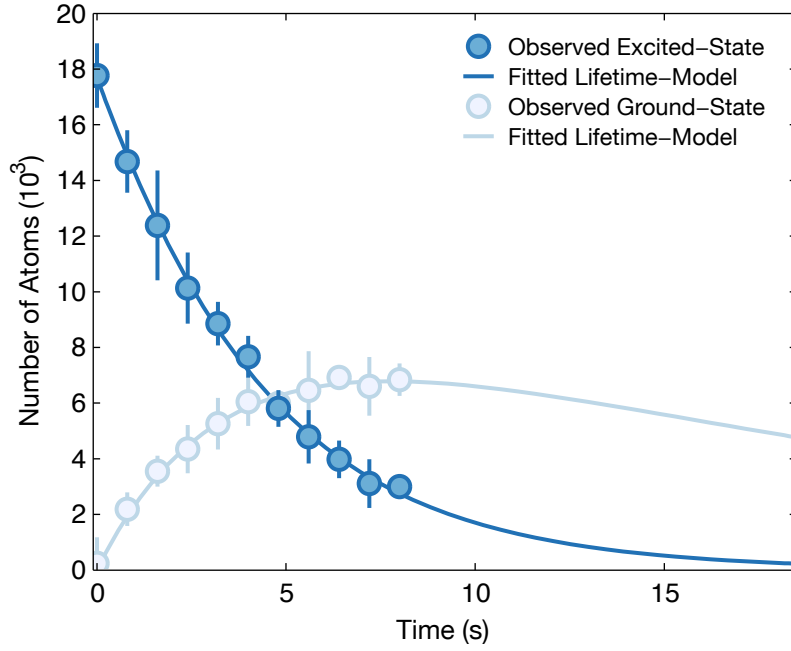


**Figure 6.6.** | **Simulation of the Lifetime of a Spin-Polarized Gas in Deep 3D-Lattice.** Shown is the fit of a lifetime model incorporating density dependent losses to experimental lifetime data. See main text for details.

$$\frac{dN_g}{dt} = -\gamma_g N_g + \gamma_e N_e - \gamma_{eg} N_e N_g \quad (6.16)$$

Here  $\gamma_g = 0.054/\text{s}$  is the single-particle loss-rate of ground-state atoms as shown in equation 6.14. The loss-rate  $\gamma_{eg}$  describes onsite inelastic scattering.

This model neglects excited-state decay into higher bands (Lamb-Dicke regime) and it assumes the same  $\gamma_g$  for the ground- and excited-state.

The lifetime model is fitted to the data. The regression yields the following values (for completeness also  $\gamma_g$  is given but is held constant during the fit):

$$\begin{aligned} \gamma_g &= 0.0540/\text{s} \\ \gamma_e &= 0.1558/\text{s} \\ \gamma_{eg} &= 0.0045/\text{s} \end{aligned} \quad (6.17)$$

The experimental data together with the fitted lifetime model is shown in figure 6.6. The data and the lifetime model seem to agree well and the behavior for longer time scales is

reasonable. The lifetime model presented here shows the best fit results compared to simpler models which do not include a density-dependent term. See appendix A for details.

To conclude this section a lifetime measurements in a deep optical lattice of  $^{173}\text{Yb}$  in the metastable excited state was presented. The behavior of the atom-number was simulated using rate equations. A density-dependent loss-term has to be incorporated in order to describe the observed particle number dynamics. This means the loss process between excited and ground state atoms plays a significant role on the time scales considered here.

### 6.2.3. Lifetime of Spin-Mixtures in Shallow 1D-Lattices

This section presents the central measurements performed to implement the dissipative Fermi-Hubbard model. The data obtained using the experimental sequence outlined in section 6.2.1 is presented first. The lifetime of a Fermi-gas consisting of excited-state atoms loaded into the lattice with one-, two- and six-spin states is measured. The 1D-lattice depth was set to  $3E_R$ ,  $5E_R$ ,  $6E_R$ ,  $8E_R$ ,  $11E_R$  and  $14E_R$ . The results of this measurement are shown in figure 6.7. First, important aspects of the data are described. Numerical analysis will follow in the next section.

All measurements except  $11E_R$  and  $14E_R$  show a fast particle loss for the spin-mixtures at the beginning of the lifetime measurement. While for longer time scales some dynamics for the spin-polarized gas is visible only very moderate particle loss is observed. This is expected because tunneling and therefore particle loss is forbidden due to the Pauli principle.

The measurements for  $11E_R$  and  $14E_R$  show almost no difference in the loss rates for the three different spin configurations. This and the growth of ground-state populations suggest that the observed loss process is mainly due to radiative decay of the excited state (compare section 6.2.2).

The measurements further show that the initial particle number for different lattice depths is not stable. This makes it hard to compare absolute particle numbers. This effect is attributed to particle number and temperature fluctuations from day to day. Nevertheless, the relative particle number suggest that half of the particles are not lost at the end of the measurement.

### 6.2.4. Data Analysis

#### Loss-Coefficients and Initial Filling Fraction

From the data in figure 6.7 a particle number time evolution governed by at least two different time scales is observed: a fast loss process at the beginning and a slower loss process at longer times. Equation 6.8 is used and fitted to the first and to the second half of

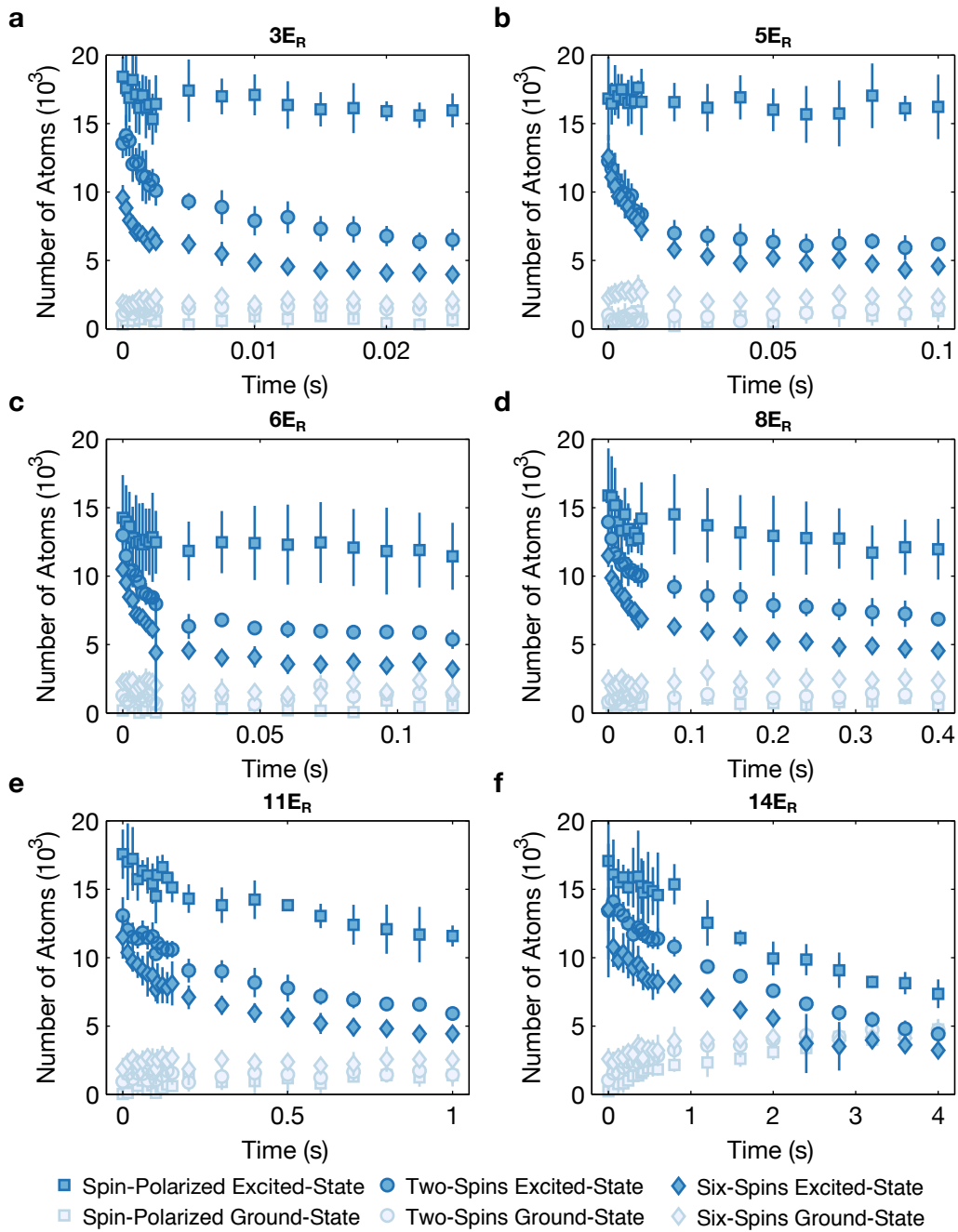


**Figure 6.7. | Lifetime of spin-mixtures for different 1D-lattice depths.** a-f show lifetime measurements for different 1D-lattice depths. For each lattice depth a spin polarized sample (square data points) as well as two and six spin mixtures are shown (round and diamond shaped data points). Note the different timescales.

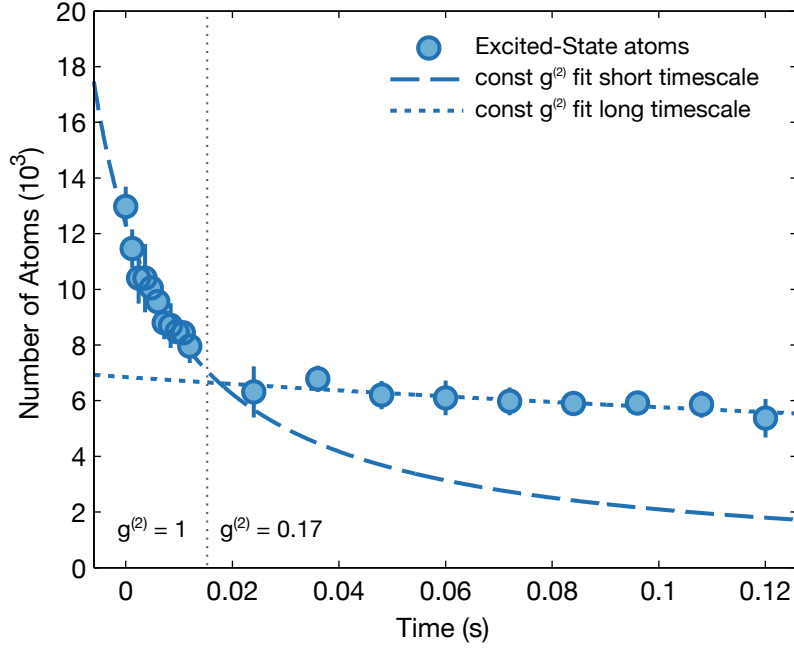


**Figure 6.8.** | Fit to the data for a two-spin mixture in a  $6E_R$  deep 1D-lattice. Shown is the lifetime measurements for a two-spin mixture with loss-rate fits to the head and the tail of the data. Similar fits have been performed for six-spin components and all other lattice depths.

the data. An example for these fits for one lattice depth and a  $N = 2$  spin state mixture is shown in figure 6.8. Similar fits have been performed for all data. The fit finds an optimal value for  $\kappa = 4q\Gamma_{\text{eff}}g^{(2)}\eta_0$ .

Equation 6.4 shows that the observed loss-rate is  $\sim J^2/U_{ee}$ . It is therefore intuitive to fit equation 6.6 to the extracted loss coefficients  $\kappa$ . The fit is allowed to find an optimal value for the product of the correlations function and initial filling  $g^{(2)}\eta_0$ . Assuming a Mott-insulator as the initial state the value of the correlation function is set to  $g^{(2)} = 1$ . This allows the extraction of the initial filling  $\eta_0$  [51].

The result of this fit is shown in figure 6.9 for a two- and six-spin mixture. The data points for  $11E_R$  and  $14E_R$  are omitted from the fit because the loss there is mainly due to the decay of excited-state atoms into the ground-state. This also means that measurements at deeper lattice depths will not help to gain more insight into the system. Further, the data point for  $6E_R$  is omitted because of stability problems of the experimental machine at the day the data was taken (including that data point affects the fitted filling only very slightly).



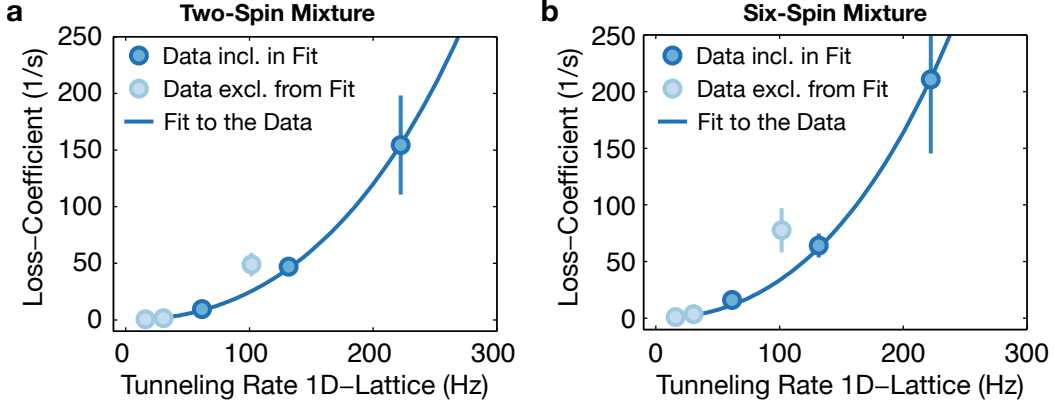


**Figure 6.9.** | **Extracted loss-coefficients  $\kappa$  for head of data.** **a** and **b** show the loss-coefficients  $\kappa$  extracted from the fits to the head of the loss-rate measurements. The solid line shows a single-parameter fit to the data. The light datapoints are excluded from the fit.

The fit yields:

$$\frac{\eta_{0,N}}{1/N} \begin{cases} N=2 & \frac{0.42 \pm 0.02}{1/N} \approx 84\% \pm 4\% \\ N=6 & \frac{0.14 \pm 0.01}{1/N} \approx 84\% \pm 6\% \end{cases} \quad (6.18)$$

where  $N$  is the number of spin states and  $\eta_{0,N}$  is the filling fraction for the two- or six-spin mixture. The filling fraction has been normalized to the case of one particle per lattice site. Note that  $\kappa_{N=6} = 4\kappa_{N=2}$  because in the six-spin case there are four more possible particles to scatter with. Besides determining the initial filling fraction the correct scaling of  $\kappa$  is confirmed:  $\kappa$  should scale with  $J^2/U_{ee}$  which is observed in figure 6.9.

### Nearest Neighbor Correlations

For longer timescales, a significant decrease in the loss rate is observed. For the slower loss, the loss-coefficient is extracted from a fit of equation 6.6 to the data points at the end of the time series. Again the extracted loss coefficients are plotted against  $J^2/U_{ee}$  which is shown in figure 6.10.

During the analysis of the loss coefficient for the head of the data a Mott insulator state and thus  $g^{(2)} = 1$  was assumed. For the tail of the data, the atoms had time to interact and  $g^{(2)}$  can start to deviate from unity. The fit to the tail yields the factor  $g^{(2)}\eta_0$ .  $\eta_0$  is used from the fit to the beginning of the time series and allows deducing  $g^{(2)}$  for the long timescales to:

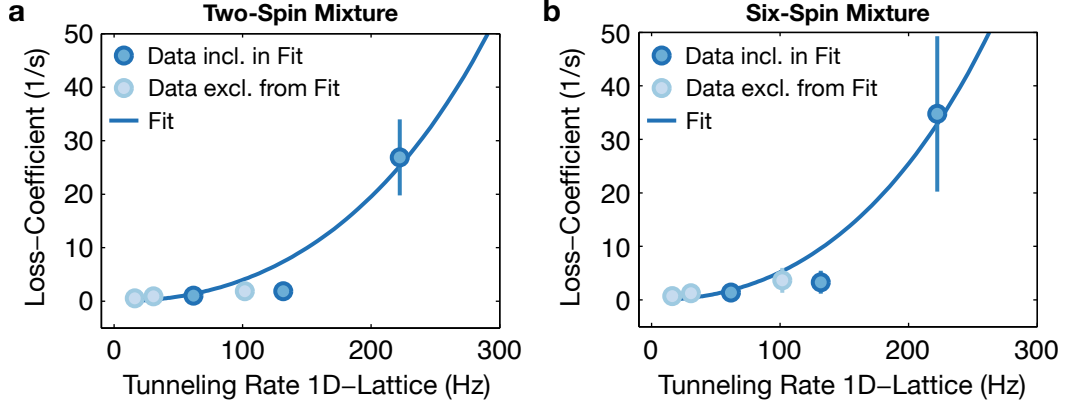


**Figure 6.10.** | **Extracted loss-coefficients  $\kappa$  from fit to tail of the data.** **a** and **b** show the loss-coefficients  $\kappa$  extracted from the fits to the tail of the loss-rate measurements. The solid line shows a single-parameter fit to the data. The light datapoints are excluded from the fit because.

$$\begin{aligned} g_{N=2}^{(2)} &= 0.17 \pm 0.07 \\ g_{N=6}^{(2)} &= 0.14 \pm 0.02 \end{aligned} \quad (6.19)$$

Note that the loss coefficients for the long timescales are very similar to the loss coefficient observed for the spin-polarized gas in the deep lattice (data points for lattice depths from  $5E_R$  to  $14E_R$ ). Only the loss coefficient for  $3E_R$  is significantly different indicating that loss-processes scaling with  $J^2/U_{ee}$  are observed. Further measurements at intermediate lattice depths are needed to confirm this.

### Remaining Atom Number

As a final analysis step, the atom number observed during the loss processes is analyzed. In figure 6.11 the ratio of  $N_0$  determined by the fit to the beginning of the loss sequences and the number of atoms at approximately two times the time constant of the fast loss is plotted.

No significant difference for the remaining number of atoms for the different lattice depths is observed. Further a slightly lower number of remaining atoms for the six-spin components mixture compared to two spins can be seen.

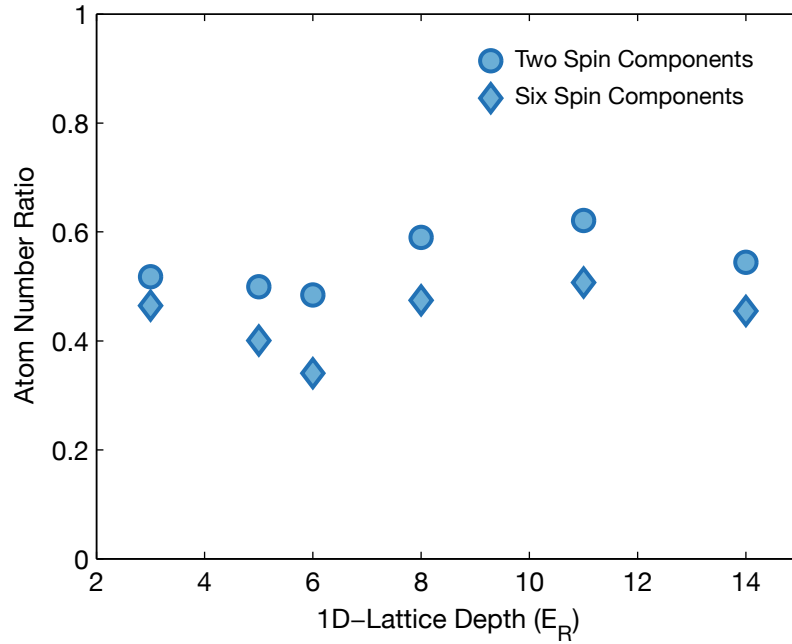


**Figure 6.11. | Remaining atoms after a loss sequence.** Plotted is the ratio of remaining atoms after approximately two times the time of the fast initial loss to the initial number of atoms extracted from the fit. The ratio is shown for different 1D-lattice depths.

### 6.2.5. Discussion

The loss sequences show two distinct characteristics: a strong suppression of atom loss after approximately half of the atoms are lost and a slightly lower number of remaining atoms for the six-spin state mixture.

The reduction in loss-rate can stem from different mechanisms: A suppression of losses is expected for a *thinning* of the sample. This means that due to the already occurred losses an atom needs to tunnel (multiple) times to find another partner with which it can interact. This explanation would allow concluding that a real reduction in  $g^{(2)}$  is observed as stated above. However, other mechanisms can also lead to a reduction of the loss-rate: due to the harmonic confinement by the lattice beams an energy offset between adjacent lattice sites exists which effectively reduces the tunneling rate and localize atoms which sit at the edge of the trap. While this will reduce the loss rate to some degree the atoms still can find loss-partners at the region where they are located. The reduction of loss rate due to the offset from site to site is on the order of 10% for the experiments conducted here. Another mechanism for a loss-rate reduction is the presence of ground state atoms which are present because of imperfections in the excited state preparation scheme. On the one hand, these

atoms have different interaction energies (potentially very large, see table 2.3) and at the same time will be lost from the trapping potentials with a lower rate compared to excited state - excited-state collisions. Thus it is possible that the ground-state atoms significantly reduce the observed loss rate. This effect needs further investigation in the future. Another potential mechanism for loss suppression is a severe spin imbalance which could suppress tunneling and losses due to the Pauli principle. This effect is unlikely because the initial spin mixture can be prepared very well and the remaining ground state atoms after excited state preparation give an upper bound for the amount of spin imbalance. While not completely understood it is probable that the thinning of the sample leads to the reduction of the loss-rate and therefore a reduction in the nearest-neighbor correlation function is observed. This assumption is supported by the fact that the tunneling rate along the 1D-tubes is comparable to  $\Gamma_{\text{eff}}$  which means that the redistribution rate of atoms has a significant effect on the loss.

The second observation, the lower number of remaining atoms for the six spin state mixture, can be explained in terms of the number of available atoms to scatter with. Because on average the six spin state mixture has four more partners to induce a loss the probability of formation of *spin domains* which shield atoms from a loss is significantly smaller. However, the difference in remaining atoms is small which means the effect if present at all, is very small and both spin-mixtures behave essentially the same. The fact that both mixtures behave essentially the same is a further sign that the reduction of the loss rate can be attributed to a reduction in nearest-neighbor loss partners.

Note that a similar reduction of the loss rate was also observed in [52, Supp. Material] but was explained due to the low number of particles per lattice tube which is not the case for the experiments described here.

### 6.3. Possibility of Loss-Measurements as a Probe for the Initial State

After the presentation of the data the question arises which information about the lossy fermionic system can be extracted from similar loss sequences. The Rey group showed that the combination of a lossy fermionic system with spin-independent interaction will lead to an entangled many-body state [55]. In the cited paper the system evolves into a state where Dicke-type spin entanglement is formed through the loss process. The correlations build up over time. It is possible to turn the argument around and ask if the loss-sequences could be used to determine the initial state of the system.

Assume a simple double-well potential with two fermions with opposite spin, a two body loss process, onsite interaction and tunneling between the wells. The spatial wave function

with is denoted by  $|\text{L}\rangle$  or  $|\text{R}\rangle$  for the left and right well and the spin degree of freedom is labeled by  $|\uparrow\rangle$  and  $|\downarrow\rangle$ . The states the system is able to occupy are then [136]:

$$\begin{aligned}
|\text{LR}\rangle^+ &= (|\text{LR}\rangle + |\text{RL}\rangle) \otimes (|\uparrow\downarrow\rangle - |\downarrow\uparrow\rangle) \\
|\text{LR}\rangle^- &= (|\text{LR}\rangle - |\text{RL}\rangle) \otimes (|\uparrow\downarrow\rangle + |\downarrow\uparrow\rangle) \\
|\text{LL}\rangle^+ &= |\text{LL}\rangle \otimes (|\uparrow\downarrow\rangle - |\downarrow\uparrow\rangle) \\
|\text{RR}\rangle^+ &= |\text{RR}\rangle \otimes (|\uparrow\downarrow\rangle - |\downarrow\uparrow\rangle)
\end{aligned} \tag{6.20}$$

Here  $\pm$  denote the symmetry of the spatial wavefunction. A two particle loss can only occur in states where both particles occupy the same well, i.e.  $|\text{LL}\rangle^+$  or  $|\text{RR}\rangle^+$ . When tunneling between the states is allowed the system will be in an arbitrary superposition of  $|\text{LR}\rangle^+$  and  $|\text{LR}\rangle^-$ . The spin wavefunction is in general conserved so that only the state  $|\text{LR}\rangle^+$  is coupled to  $|\text{LL}\rangle^+$  and  $|\text{RR}\rangle^+$ . Thus the symmetric part of the spatial wavefunction will decay through two body loss while  $|\text{LR}\rangle^-$  is conserved. Therefore, after some time the system will evolve into a symmetric spin state with average occupation given by the initial state. This is exactly the behavior which was investigated for a lattice chain and a many body system in [55].

This argument is now turned around: when the system is in one of the two states it will experience no loss (for  $|\text{LR}\rangle^-$ ) or a complete loss of all particles (for  $|\text{LR}\rangle^+$ ). The amount of atom loss observed is thus directly connected to the initial state of the system.

For a lattice system, the situation is more complex and more involved simulations are necessary to study a dissipative system with respect to the influence of the initial state on the loss dynamics which is beyond the scope of this thesis. One could hope that similar arguments as for the double well hold. A similar idea as presented here was formulated in [137].

## 6.4. Summary

This chapter showed experiments using a quantum gas of neutral, fermionic atoms subject to two-body losses in a 1D-lattice structure. The observed loss sequences show a strong initial loss which is quickly suppressed. From the first loss, the initial filling fraction of the lattice is extracted. For the cases of only two spin states as well as for six spin states a filling of 84% was extracted. The slower loss at the end of the loss sequences yields a value for the initial filling times the nearest neighbor correlation function  $g^{(2)}$ . Because the initial filling is known from the initial strong loss an effective reduction of  $\eta_0 g^{(2)}$  by a factor of five is observed. The number of remaining atoms is about 50% of the initial number of atoms while the six-spin mixture shows a small but consistent lower amount of remaining atoms.

The measurements presented here should be regarded of a proof of concept and a starting point for further studies. First, additional measurements should repeat the loss sequences presented here for all spin combinations offered by  $^{173}\text{Yb}$  (one spin state up to all six spin states). Here the most interesting questions is whether a consistent dependence of the remaining atom number on the number of spin states is shown. Another interesting tuning knob is the balance between the spin states and the influence of unbalanced mixtures which should influence the number of atoms remaining but the specific way this influence scales with the imbalance could allow extracting information about the formation of regions in the lattice which is shielded from losses because of the Pauli principle. Equally important the question whether the remaining ground-state atoms influence the observed dynamics needs to be clarified. Thus the measurements presented here should be repeated with forcefully removing the ground state atoms using a resonant laser pulse.

The second future measurement along those lines is the use of another isotope with similar two-body losses but significantly different onsite interaction.  $\text{Yb}^{171}$  is a perfect candidate for such experiments. It has a ground state s-wave scattering length of  $a_s = -4a_0$ . This interaction strength would result in a ratio  $\hbar\Gamma/U \approx 15$  which is well in the Zeno-isolator regime (compare with figure 6.4). The s-wave scattering length for the excited state is not known but one could hope that it is significantly different compared to  $^{173}\text{Yb}$ . Here again, the question of the influence of the number of spin state arises and whether a significantly different loss behavior is observed. A setup for the production of isotope mixtures is currently been set up and therefore both of the ideas for future measurements are feasible in the near future.

## 7. Summary and Outlook

In this thesis, the setup and characterization of a quantum gas machine capable of producing ultracold samples of bosonic and fermionic Ytterbium were presented. The experimental apparatus allows the cooling, trapping and detection of such samples in a triangular magic optical lattice which was specifically designed to enable the creation of atoms in the metastable state. Further, a new and robust preparation scheme for the creation of metastable state Ytterbium atoms based on a rapid adiabatic passage was implemented. This new method not only allows the production of excited state atoms but also allowed insights into the initial quantum state by analyzing the observed atom number dynamics during the transfer. The loading of meta-stable state atoms occupying different spin states into 1D-lattice tubes allowed the realization of a Fermi-Hubbard model with two-body losses. This model was used to study the particle number dynamics of a spin-polarized gas loaded into a deep optical lattice. From this measurement, it was found that the number of excited state atoms decays significantly faster than expected from the lifetime of a free atom. This effect is attributed to the influence of the lattice laser beams and a density loss between the excited state and ground state atoms. The same principle measurement was then used to study the particle number dynamics of a spin mixture in shallow 1D-lattice tubes. A fast initial two-body loss followed by a slower particle loss is observed. The reduction in loss-rate was attributed to an effective reduction in nearest-neighbor correlations.

The loss measurements presented in this thesis should be regarded as a starting point for the further investigation of dissipative Fermi-Hubbard systems. In particular, the open questions posed in the corresponding chapter are a great point to deepening the understanding of the system. One of the central questions, which could not be answered in this thesis, is whether the remaining ground state atoms influence the observed particle number dynamics. This question can be tackled by forcefully removing atoms using a resonant light pulse. One would need to check whether this light pulse results in additional heating of the excited state atoms. Additionally, the question remains if the slow loss rate observed at longer timescales can be described by a loss-rate which scales with  $J^2/U_{ee}$ . While the data suggests that this is indeed the case, more data at various intermediate 1D-lattice depths and additional averaging and measurements for longer timescales are necessary. Another major question is the influence of the number of occupied spin-states. This could be investigated with other spin-state mixtures and spin-imbalanced mixtures and the question is whether the occupied spin-states have an influence on the remaining number of atoms. This could hint at the buildup of spin correlations and the formation of a spin-domains reducing

the observed loss. Another very interesting question is what happens to the observed dynamics when the dominant energy scale is not given by the elastic interaction and if and how this affects the observed loss-rate reduction. This could be investigated using  $^{171}\text{Yb}$  which has a negligible s-wave scattering length in the ground-state. The scattering length for the excited-state is currently not known but one could hope that it is significantly different from the scattering length of  $^{173}\text{Yb}$ . This could allow accessing the Zeno-Effect dominated loss-regime. Because of the vanishing ground state scattering length direct evaporative cooling is not feasible but sympathetic cooling has been demonstrated. If the s-wave scattering length of the excited state is not low enough to reach the Zeno-dominated regime another path could be the use of a photoassociation resonance on the  $^1\text{S}_0 \leftrightarrow ^1\text{P}_1$  transition which would allow inducing onsite two-body losses in the ground state. A setup for addressing a photoassociation resonance is already implemented and the experimental setup is currently modified to allow the creation of quantum gases of  $^{171}\text{Yb}$ .

$^{171}\text{Yb}$  is also a key ingredient for the study of the Kondo-Lattice model (KLM) which is the second major modification to the experimental setup which is currently pursued. The KLM relies on the interaction of localized and mobile spins via an exchange interaction. Ytterbium in its excited state will play the role of immobile atoms while ground state atoms will play the role of mobile atoms. This setup is realized with a state-dependent optical 1D-lattice at  $\lambda = 660\text{ nm}$  which will complement the magic lattice currently in use. Because the KLM assumes no interaction between the mobile species,  $^{173}\text{Yb}$  with its nonnegligible s-wave scattering length is not well suited for studying the “pure” KLM. This is why the creation of  $^{171}\text{Yb}$  quantum gases is important not only for the loss measurements presented above. To implement the KLM two main questions remain and need to be studied in detail before specific phases of the KLM can be realized and detected: first, the  $^3\text{P}_0 \leftrightarrow ^1\text{S}_0$  interaction, elastic as well as inelastic, need to be characterized well to understand the limits of the simulated system. Second, ideally each lattice site is occupied by one excited state atom (“immobile spin”) while a variable ground state density is realized. This allows accessing the whole phase space. While the inelastic scattering properties can be measured with similar techniques as the loss measurements presented in this thesis, the preparation is in no way straightforward task. Here, the rapid adiabatic passage could be a helpful tool. One idea would be the creation of an ultracold two spin-mixture with enough particles to create as much doubly occupied lattice sites as possible. Afterward, a RAP is performed which is interrupted at the detuning where the probability in finding either  $|-\rangle$  or  $|+\rangle$  is large while  $|ee\rangle$  is still mostly unoccupied. If and how this works needs to be checked very carefully, especially with regard to long-term stability. When realized the KLM in an optical lattice not only allows to explore the theoretically well understood 1D-KLM but also opens up the possibility to study the KLM in higher dimensions. The tuning of the ground state atom density will open up the possibility to access the regime of longer range RKKY-interactions [32] where an interaction of the localized atoms among each other is mediated by the mobile atoms. Using  $^{173}\text{Yb}$  could answer the question how an interaction between the mobile species influences the dynamics of the system.



# Appendix A.

## Comparison of Lifetime Models

In section 6.2.2 a rate-equation model to describe the lifetime of  $^{173}\text{Yb}$  excited-state atoms in a deep optical lattice was introduced. The model described by equation 6.15 and equation 6.16 incorporated density dependent losses because of inelastic scattering between ground- and excited-state atoms and two different loss-rates for the excited-state. One loss-rate describes loss from the trap and the other one describes decay into the ground state.

Here the full lifetime-model is compared to three simpler models neglecting certain aspects of the full model. It will be shown that a model without density dependent losses is not able to capture the experimentally observed dynamics.

Our first model removes all density dependence from the full model and assumes that all excited state atoms decay into the ground-state. This model is called “single-e-Loss-Rate” and it is described by:

$$\begin{aligned}\frac{dN_e}{dt} &= -\gamma_e N_e \\ \frac{dN_g}{dt} &= -\gamma_g N_g + \gamma_e N_e\end{aligned}\tag{A.1}$$

In the second model the excited state is allowed to decay to the ground state as well as to the continuum (i.e. excited-state atoms are lost from the trap). In contrast to the full model it is not assumed that the background loss-rate (i.e.  $\gamma_g$  and  $\gamma$ ) is the same for the excited and the ground-state. The model is described by:

$$\begin{aligned}\frac{dN_e}{dt} &= -\gamma N_e - \gamma_e N_e \\ \frac{dN_g}{dt} &= -\gamma_g N_g + \gamma_e N_e\end{aligned}\tag{A.2}$$

By including a density term but removing the possibility for the excited-state atoms to be lost from the trap without first occupying the ground-state is called “density-only” and is given by:

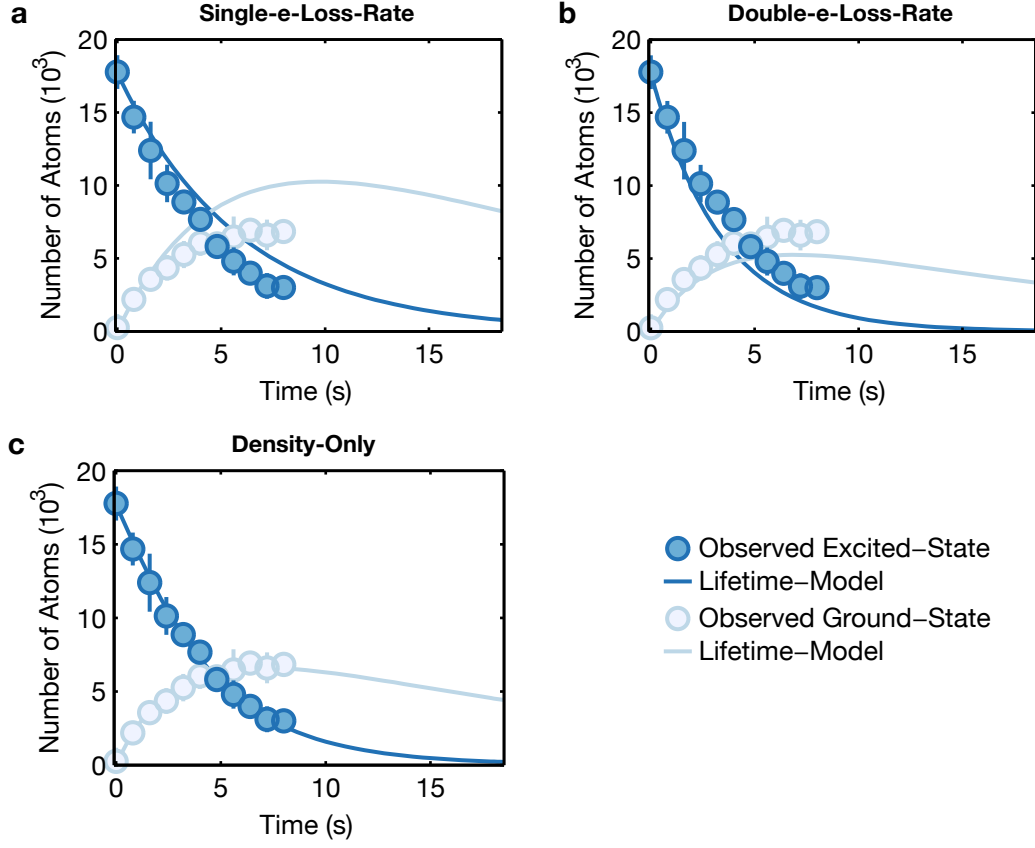


**Figure A.1. | Comparison of Lifetime Models.** **a** shows the simple lifetime-model without density dependent losses and with a single excited-state loss-rate. In **b** two different loss-rates for the excited state are allowed where one of them is coupled to the gain of atoms in the ground-state while the other losses atoms from the trap. **c** shows the lifetime-model with a simple density dependence.

$$\begin{aligned}\frac{dN_e}{dt} &= -\gamma_e N_e - \gamma_{eg} N_e N_g \\ \frac{dN_g}{dt} &= -\gamma_g N_g + \gamma_e N_e - \gamma_{eg} N_e N_g\end{aligned}\tag{A.3}$$

For each of the models fits to the experimental data are performed. The result is presented in figure A.1. From the figure it is obvious that loss-rate models without including two-body losses are not able to describe the observed experimental dynamics. While the “Double-e-Loss-Rate” model is better compared to the first model it still deviates significantly from the data. The density model resembles the data well and only by comparing the residual

errors of the third model and the full model a difference is found. In the following table the residual least-squares errors for the four models are shown:

$$\begin{aligned} E_{\text{SingleRate}} &= 77.62 \\ E_{\text{DoubleRate}} &= 6.72 \\ E_{\text{DensityOnly}} &= 1.59 \\ E_{\text{FullModel}} &= 0.96 \end{aligned} \tag{A.4}$$

This comparison shows that the full model indeed gives the best result in terms of least square error. However the difference between the “Density-Only”-model and the full-model is small. The important result from this appendix and section 6.2.2 is that density-dependent losses play a significant role in the lifetime of the excited-state even for a spin-polarized Fermi-gas.



## Appendix B.

# Rapid Adiabatic Passage Interaction Hamiltonian

In chapter 5 the rapid adiabatic passage (RAP) process for a doubly occupied lattice site was simulated. The Hamiltonian  $\hat{H}(t)$  used for the simulation consists of an interatomic interaction term, an atom-light interaction term, a linear Zeeman-term and the electronic term. Details can be found in [57]. The complete interaction Hamiltonian for the states  $|gg\rangle$ ,  $|ee\rangle$ ,  $|+\rangle$  and  $|-\rangle$  is then written in the rotating wave approximation (RWA) as:

$$\hat{H}(t) = \begin{bmatrix} U_{gg} + \Delta(t)/2 + Z_g & 0 & \sqrt{2}/4 (\Omega_{\uparrow} + \Omega_{\downarrow}) & \sqrt{2}/4 (\Omega_{\uparrow} - \Omega_{\downarrow}) \\ 0 & U_{ee} + \Delta(t)/2 + Z_e & \sqrt{2}/4 (\Omega_{\uparrow} + \Omega_{\downarrow}) & \sqrt{2}/4 (\Omega_{\uparrow} - \Omega_{\downarrow}) \\ \sqrt{2}/4 (\Omega_{\uparrow} + \Omega_{\downarrow}) & \sqrt{2}/4 (\Omega_{\uparrow} + \Omega_{\downarrow}) & U_{eg}^+ + Z_+ & Z_- \\ \sqrt{2}/4 (\Omega_{\uparrow} - \Omega_{\downarrow}) & \sqrt{2}/4 (\Omega_{\uparrow} - \Omega_{\downarrow}) & Z_- & U_{eg}^- + Z_+ \end{bmatrix} \quad (\text{B.1})$$

All energies are assumed to be given in Hz.  $\Omega_{\uparrow/\downarrow}$  is the spin state dependent Rabi frequency depending on the particular  $m_F$  transition.  $Z_{g/e} = Z_{g/e,\uparrow} + Z_{g/e,\downarrow}$  are the total Zeeman shifts for two atoms in the ground or excited state and  $Z_{\pm} = 1/2 (\pm Z_{g,\uparrow} + Z_{g,\downarrow} + Z_{e,\uparrow} \pm Z_{e,\downarrow})$ . The onsite interaction is given by  $U_{gg}$ ,  $U_{ee}$ ,  $U_{eg}^+$  and  $U_{eg}^-$  for the various electronic configurations.  $\Delta(t)$  is the laser detuning.

The hamiltonian is numerically solved with a third order Runge-Kutta method. Convergence of the method is checked by varying the time step.



# Bibliography

- [1] A. Montina: “Exponential complexity and ontological theories of quantum mechanics”, *Phys. Rev. A* **77**, 022104 (2008).
- [2] J. Quintanilla and C. Hooley: “The strong-correlations puzzle”, *Physics World* **22** (06), 32 (2009).
- [3] H. Tsunetsugu, M. Sigrist and K. Ueda: “The ground-state phase diagram of the one-dimensional Kondo lattice model”, *Rev. Mod. Phys.* **69**, 809–864 (1997).
- [4] D. Jaksch, C. Bruder, J. I. Cirac, C. W. Gardiner and P. Zoller: “Cold Bosonic Atoms in Optical Lattices”, *Phys. Rev. Lett.* **81**, 3108–3111 (1998).
- [5] D. Jaksch and P. Zoller: “The cold atom Hubbard toolbox”, *Annals of Physics* **315** (1), 52 – 79 (2005), special Issue.
- [6] J. Hubbard: “Electron Correlations in Narrow Energy Bands”, *Proceedings of the Royal Society of London A: Mathematical, Physical and Engineering Sciences* **276** (1365), 238–257 (1963).
- [7] M. Greiner, O. Mandel, T. Esslinger, T. W. Hansch and I. Bloch: “Quantum phase transition from a superfluid to a Mott insulator in a gas of ultracold atoms”, *Nature* **415** (6867), 39–44 (2002).
- [8] R. Jordens, N. Strohmaier, K. Gunter, H. Moritz and T. Esslinger: “A Mott insulator of fermionic atoms in an optical lattice”, *Nature* **455** (7210), 204–207 (2008).
- [9] U. Schneider, L. Hackermüller, S. Will, T. Best, I. Bloch, T. A. Costi, R. W. Helmes, D. Rasch and A. Rosch: “Metallic and Insulating Phases of Repulsively Interacting Fermions in a 3D Optical Lattice”, *Science* **322** (5907), 1520–1525 (2008).
- [10] W. S. Bakr, J. I. Gillen, A. Peng, S. Fölling and M. Greiner: “A quantum gas microscope for detecting single atoms in a Hubbard-regime optical lattice”, *Nature* **462** (7269), 74–77 (2009).
- [11] J. F. Sherson, C. Weitenberg, M. Endres, M. Cheneau, I. Bloch and S. Kuhr: “Single-atom-resolved fluorescence imaging of an atomic Mott insulator”, *Nature* **467** (7311), 68–72 (2010).

- 
- [12] M. F. Parsons, F. Huber, A. Mazurenko, C. S. Chiu, W. Setiawan, K. Wooley-Brown, S. Blatt and M. Greiner: “Site-Resolved Imaging of Fermionic  ${}^6\text{Li}$  in an Optical Lattice”, *Phys. Rev. Lett.* **114**, 213002 (2015).
- [13] L. W. Cheuk, M. A. Nichols, M. Okan, T. Gersdorf, V. V. Ramasesh, W. S. Bakr, T. Lompe and M. W. Zwierlein: “Quantum-Gas Microscope for Fermionic Atoms”, *Phys. Rev. Lett.* **114**, 193001 (2015).
- [14] B. Zimmermann, T. Müller, J. Meineke, T. Esslinger and H. Moritz: “High-resolution imaging of ultracold fermions in microscopically tailored optical potentials”, *New Journal of Physics* **13** (4), 043007 (2011).
- [15] E. Haller, J. Hudson, A. Kelly, D. A. Cotta, B. Peaudecerf, G. D. Bruce and S. Kuhr: “Single-atom imaging of fermions in a quantum-gas microscope”, *Nat Phys* **11** (9), 738–742 (2015).
- [16] M. Endres, H. Bernien, A. Keesling, H. Levine, E. R. Anschuetz, A. Krajenbrink, C. Senko, V. Vuletic, M. Greiner and M. D. Lukin: “Cold Matter Assembled Atom-by-Atom”, arXiv preprint arXiv:1607.03044 (2016).
- [17] M. F. Parsons, A. Mazurenko, C. S. Chiu, G. Ji, D. Greif and M. Greiner: “Site-resolved observations of antiferromagnetic correlations in the Hubbard model”, arXiv preprint arXiv:1605.02704 (2016).
- [18] R. Islam, R. Ma, P. M. Preiss, M. Eric Tai, A. Lukin, M. Rispoli and M. Greiner: “Measuring entanglement entropy in a quantum many-body system”, *Nature* **528** (7580), 77–83 (2015).
- [19] C. Becker, P. Soltan-Panahi, J. Kronjäger, S. Dörscher, K. Bongs and K. Sengstock: “Ultracold quantum gases in triangular optical lattices”, *New Journal of Physics* **12** (6), 065025 (2010).
- [20] L. Tarruell, D. Greif, T. Uehlinger, G. Jotzu and T. Esslinger: “Creating, moving and merging Dirac points with a Fermi gas in a tunable honeycomb lattice”, *Nature* **483** (7389), 302–305 (2012).
- [21] S. Taie, H. Ozawa, T. Ichinose, T. Nishio, S. Nakajima and Y. Takahashi: “Coherent driving and freezing of bosonic matter wave in an optical Lieb lattice”, *Science Advances* **1** (10) (2015).
- [22] G. Jotzu, M. Messer, R. Desbuquois, M. Lebrat, T. Uehlinger, D. Greif and T. Esslinger: “Experimental realization of the topological Haldane model with ultracold fermions”, *Nature* **515** (7526), 237–240 (2014).
- [23] N. Fläschner, B. Rem, M. Tarnowski, D. Vogel, D.-S. Lühmann, K. Sengstock and C. Weitenberg: “Experimental reconstruction of the Berry curvature in a Floquet Bloch band”, *Science* **352** (6289), 1091–1094 (2016).



- [24] J. Struck, M. Weinberg, C. Olschlager, P. Windpassinger, J. Simonet, K. Sengstock, R. Hoppner, P. Hauke, A. Eckardt, M. Lewenstein and L. Mathey: “Engineering Ising-XY spin-models in a triangular lattice using tunable artificial gauge fields”, *Nat Phys* **9** (11), 738–743 (2013).
- [25] T. Kock, M. Ölschläger, A. Ewerbeck, W.-M. Huang, L. Mathey and A. Hemmerich: “Observing Chiral Superfluid Order by Matter-Wave Interference”, *Phys. Rev. Lett.* **114**, 115301 (2015).
- [26] K. Aikawa, A. Frisch, M. Mark, S. Baier, A. Rietzler, R. Grimm and F. Ferlaino: “Bose-Einstein Condensation of Erbium”, *Phys. Rev. Lett.* **108**, 210401 (2012).
- [27] M. Lu, N. Q. Burdick, S. H. Youn and B. L. Lev: “Strongly Dipolar Bose-Einstein Condensate of Dysprosium”, *Phys. Rev. Lett.* **107**, 190401 (2011).
- [28] Y. Takasu, K. Maki, K. Komori, T. Takano, K. Honda, M. Kumakura, T. Yabuzaki and Y. Takahashi: “Spin-Singlet Bose-Einstein Condensation of Two-Electron Atoms”, *Phys. Rev. Lett.* **91**, 040404 (2003).
- [29] S. Stellmer, M. K. Tey, B. Huang, R. Grimm and F. Schreck: “Bose-Einstein Condensation of Strontium”, *Phys. Rev. Lett.* **103**, 200401 (2009).
- [30] P. Halder, C.-Y. Yang and A. Hemmerich: “Alternative route to Bose-Einstein condensation of two-electron atoms”, *Phys. Rev. A* **85**, 031603 (2012).
- [31] N. Hinkley, J. A. Sherman, N. B. Phillips, M. Schioppo, N. D. Lemke, K. Beloy, M. Pizzocaro, C. W. Oates and A. D. Ludlow: “An Atomic Clock with 10–18 Instability”, *Science* **341** (6151), 1215–1218 (2013).
- [32] A. V. Gorshkov, M. Hermele, V. Gurarie, C. Xu, P. S. Julienne, J. Ye, P. Zoller, E. Demler, M. D. Lukin and A. M. Rey: “Two-orbital SU(N) magnetism with ultracold alkaline-earth atoms”, *Nat Phys* **6** (4), 289–295 (2010).
- [33] M. Foss-Feig, M. Hermele and A. M. Rey: “Probing the Kondo lattice model with alkaline-earth-metal atoms”, *Phys. Rev. A* **81**, 051603 (2010).
- [34] F. Scazza, C. Hofrichter, M. Hofer, P. C. De Groot, I. Bloch and S. Fölling: “Observation of two-orbital spin-exchange interactions with ultracold SU(N)-symmetric fermions”, *Nat. Phys.* **10** (10), 779–784 (2014).
- [35] G. Cappellini, M. Mancini, G. Pagano, P. Lombardi, L. Livi, M. Siciliani de Cumis, P. Cancio, M. Pizzocaro, D. Calonico, F. Levi, C. Sias, J. Catani, M. Inguscio and L. Fallani: “Direct Observation of Coherent Interorbital Spin-Exchange Dynamics”, *Phys. Rev. Lett.* **113**, 120402 (2014).
- [36] R. Zhang, Y. Cheng, H. Zhai and P. Zhang: “Orbital Feshbach Resonance in Alkali-Earth Atoms”, *Phys. Rev. Lett.* **115**, 135301 (2015).

- 
- [37] M. Höfer, L. Riegger, F. Scazza, C. Hofrichter, D. R. Fernandes, M. M. Parish, J. Levinsen, I. Bloch and S. Fölling: “Observation of an Orbital Interaction-Induced Feshbach Resonance in  $^{173}\text{Yb}$ ”, *Phys. Rev. Lett.* **115**, 265302 (2015).
- [38] G. Pagano, M. Mancini, G. Cappellini, L. Livi, C. Sias, J. Catani, M. Inguscio and L. Fallani: “Strongly Interacting Gas of Two-Electron Fermions at an Orbital Feshbach Resonance”, *Phys. Rev. Lett.* **115**, 265301 (2015).
- [39] F. Gerbier and J. Dalibard: “Gauge fields for ultracold atoms in optical superlattices”, *New Journal of Physics* **12** (3), 033007 (2010).
- [40] B. Song, C. He, S. Zhang, Y. Zou, E. Hacıyev, W. Huang, X.-J. Liu and G.-B. Jo: “Spin-orbit coupled two-electron Fermi gases of ytterbium atoms”, arXiv:1608.00478v1 [cond-mat.quant-gas] (2016).
- [41] M. Lahrz, M. Lemeshko, K. Sengstock, C. Becker and L. Mathey: “Detecting quadrupole interactions in ultracold Fermi gases”, *Phys. Rev. A* **89**, 043616 (2014).
- [42] M. Mancini, G. Pagano, G. Cappellini, L. Livi, M. Rider, J. Catani, C. Sias, P. Zoller, M. Inguscio, M. Dalmonte and L. Fallani: “Observation of chiral edge states with neutral fermions in synthetic Hall ribbons”, *Science* **349** (6255), 1510–1513 (2015).
- [43] A. J. Daley, M. M. Boyd, J. Ye and P. Zoller: “Quantum Computing with Alkaline-Earth-Metal Atoms”, *Phys. Rev. Lett.* **101**, 170504 (2008).
- [44] P. W. Shor: “Scheme for reducing decoherence in quantum computer memory”, *Phys. Rev. A* **52**, R2493–R2496 (1995).
- [45] V. Privman: “Decoherence in quantum computing”, in “Proceedings of the winter international symposium on Information and communication technologies”, Trinity College Dublin (2004).
- [46] *Decoherence and Quantum Computing*, pages 293–328, Springer Berlin Heidelberg, Berlin, Heidelberg (2007), ISBN 978-3-540-35775-9.
- [47] W. M. Itano, D. J. Heinzen, J. J. Bollinger and D. J. Wineland: “Quantum Zeno effect”, *Phys. Rev. A* **41**, 2295–2300 (1990).
- [48] B. Misra and E. C. G. Sudarshan: “The Zeno’s paradox in quantum theory”, *Journal of Mathematical Physics* **18** (4), 756–763 (1977).
- [49] N. Syassen, D. M. Bauer, M. Lettner, T. Volz, D. Dietze, J. J. García-Ripoll, J. I. Cirac, G. Rempe and S. Dürr: “Strong Dissipation Inhibits Losses and Induces Correlations in Cold Molecular Gases”, *Science* **320** (5881), 1329–1331 (2008).

- [50] J. J. García-Ripoll, S. Dürr, N. Syassen, D. M. Bauer, M. Lettner, G. Rempe and J. I. Cirac: “Dissipation-induced hard-core boson gas in an optical lattice”, *New Journal of Physics* **11** (1), 013053 (2009).
- [51] B. Yan, S. A. Moses, B. Gadway, J. P. Covey, K. R. A. Hazzard, A. M. Rey, D. S. Jin and J. Ye: “Observation of dipolar spin-exchange interactions with lattice-confined polar molecules”, *Nature* **501** (7468), 521–525 (2013).
- [52] B. Zhu, B. Gadway, M. Foss-Feig, J. Schachenmayer, M. L. Wall, K. R. A. Hazzard, B. Yan, S. A. Moses, J. P. Covey, D. S. Jin, J. Ye, M. Holland and A. M. Rey: “Suppressing the Loss of Ultracold Molecules Via the Continuous Quantum Zeno Effect”, *Phys. Rev. Lett.* **112**, 070404 (2014).
- [53] Y. S. Patil, S. Chakram and M. Vengalattore: “Measurement-Induced Localization of an Ultracold Lattice Gas”, *Phys. Rev. Lett.* **115**, 140402 (2015).
- [54] G. Barontini, R. Labouvie, F. Stubenrauch, A. Vogler, V. Guarrera and H. Ott: “Controlling the Dynamics of an Open Many-Body Quantum System with Localized Dissipation”, *Phys. Rev. Lett.* **110**, 035302 (2013).
- [55] M. Foss-Feig, A. J. Daley, J. K. Thompson and A. M. Rey: “Steady-State Many-Body Entanglement of Hot Reactive Fermions”, *Phys. Rev. Lett.* **109**, 230501 (2012).
- [56] F. Verstraete, M. M. Wolf and J. Ignacio Cirac: “Quantum computation and quantum-state engineering driven by dissipation”, *Nat Phys* **5** (9), 633–636 (2009).
- [57] A. Thobe: “Ultracold Yb Gases with Control over Spin and Orbital Degrees of Freedom”, Ph.D. thesis, University of Hamburg (2014).
- [58] S. E. Dörscher: “Creation of ytterbium quantum gases with a compact 2D-/3D-MOT setup”, Ph.D. thesis, University of Hamburg (2013).
- [59] F. Scazza: “Probing SU(N)-symmetric orbital interactions with ytterbium Fermi gases in optical lattices”, Ph.D. thesis, University of Munich (2015).
- [60] M. Takamoto, F.-L. Hong, R. Higashi and H. Katori: “An optical lattice clock”, *Nature* **435** (7040), 321–324 (2005).
- [61] J. Dalibard, F. Gerbier, G. Juzeliūnas and P. Öhberg: “*Colloquium* : Artificial gauge potentials for neutral atoms”, *Rev. Mod. Phys.* **83**, 1523–1543 (2011).
- [62] K. Enomoto, K. Kasa, M. Kitagawa and Y. Takahashi: “Optical Feshbach Resonance Using the Intercombination Transition”, *Phys. Rev. Lett.* **101**, 203201 (2008).
- [63] M. M. Boyd, T. Zelevinsky, A. D. Ludlow, S. Blatt, T. Zanon-Willette, S. M. Foreman and J. Ye: “Nuclear spin effects in optical lattice clocks”, *Phys. Rev. A* **76**, 022510 (2007).

- 
- [64] G. Audi, A. Wapstra and C. Thibault: “The Ame2003 atomic mass evaluation: (II). Tables, graphs and references”, Nuclear Physics A **729** (1), 337 – 676 (2003).
- [65] T. Fukuhara, S. Sugawa and Y. Takahashi: “Bose-Einstein condensation of an ytterbium isotope”, Phys. Rev. A **76**, 051604 (2007).
- [66] Y. Takasu and Y. Takahashi: “Quantum Degenerate Gases of Ytterbium Atoms”, Journal of the Physical Society of Japan **78** (1), 012001 (2009).
- [67] T. Fukuhara, S. Sugawa, Y. Takasu and Y. Takahashi: “All-optical formation of quantum degenerate mixtures”, Phys. Rev. A **79**, 021601 (2009).
- [68] S. Taie, Y. Takasu, S. Sugawa, R. Yamazaki, T. Tsujimoto, R. Murakami and Y. Takahashi: “Realization of a  $SU(2) \times SU(6)$  System of Fermions in a Cold Atomic Gas”, Phys. Rev. Lett. **105**, 190401 (2010).
- [69] Y. Takasu, K. Komori, K. Honda, M. Kumakura, T. Yabuzaki and Y. Takahashi: “Photoassociation Spectroscopy of Laser-Cooled Ytterbium Atoms”, Phys. Rev. Lett. **93**, 123202 (2004).
- [70] D. A. Steck: “Rubidium 87 D line data”, (2001).
- [71] H. J. Metcalf and P. Straten: *Laser cooling and trapping of neutral atoms*, Springer NY (1999).
- [72] W. Ketterle, D. Durfee and D. Stamper-Kurn: “Making, probing and understanding Bose-Einstein condensates”, arXiv preprint cond-mat/9904034 **5** (1999).
- [73] C. J. Foot: *Atomic physics*, Oxford University Press (2005).
- [74] T. Kuwamoto, K. Honda, Y. Takahashi and T. Yabuzaki: “Magneto-optical trapping of Yb atoms using an intercombination transition”, Phys. Rev. A **60**, R745–R748 (1999).
- [75] A. V. Taichenachev, V. I. Yudin, C. W. Oates, C. W. Hoyt, Z. W. Barber and L. Hollberg: “Magnetic Field-Induced Spectroscopy of Forbidden Optical Transitions with Application to Lattice-Based Optical Atomic Clocks”, Phys. Rev. Lett. **96**, 083001 (2006).
- [76] S. G. Porsev and A. Derevianko: “Hyperfine quenching of the metastable  $^3P_{0,2}$  states in divalent atoms”, Phys. Rev. A **69**, 042506 (2004).
- [77] B. H. Bransden and C. J. Joachain: *Physics of atoms and molecules*, Pearson Education India (2003).
- [78] S. G. Porsev, A. Derevianko and E. N. Fortson: “Possibility of an optical clock using the  $6^1S_0 \rightarrow 6^3P_0^o$  transition in  $^{171,173}\text{Yb}$  atoms held in an optical lattice”, Phys. Rev. A **69**, 021403 (2004).

- [79] A. D. Ludlow, N. D. Lemke, J. A. Sherman, C. W. Oates, G. Quéméner, J. von Stecher and A. M. Rey: “Cold-collision-shift cancellation and inelastic scattering in a Yb optical lattice clock”, *Phys. Rev. A* **84**, 052724 (2011).
- [80] M. Kitagawa, K. Enomoto, K. Kasa, Y. Takahashi, R. Ciuryło, P. Naidon and P. S. Julienne: “Two-color photoassociation spectroscopy of ytterbium atoms and the precise determinations of *s*-wave scattering lengths”, *Phys. Rev. A* **77**, 012719 (2008).
- [81] M. Egorov, B. Opanchuk, P. Drummond, B. V. Hall, P. Hannaford and A. I. Sidorov: “Measurement of *s*-wave scattering lengths in a two-component Bose-Einstein condensate”, *Phys. Rev. A* **87**, 053614 (2013).
- [82] N. D. Lemke, J. von Stecher, J. A. Sherman, A. M. Rey, C. W. Oates and A. D. Ludlow: “*p*-Wave Cold Collisions in an Optical Lattice Clock”, *Phys. Rev. Lett.* **107**, 103902 (2011).
- [83] A. Traverso, R. Chakraborty, Y. N. Martinez de Escobar, P. G. Mickelson, S. B. Nagel, M. Yan and T. C. Killian: “Inelastic and elastic collision rates for triplet states of ultracold strontium”, *Phys. Rev. A* **79**, 060702 (2009).
- [84] J. F. Kelly, M. Harris and A. Gallagher: “Collision energy pooling for  $\text{Sr}(5^3P_J)+\text{Sr}(5^3J_r) \rightarrow \text{Sr}(6^{3,1}S)+\text{Sr}(5^1S)$ ”, *Phys. Rev. A* **38**, 1225–1229 (1988).
- [85] R. Santra, K. V. Christ and C. H. Greene: “Properties of metastable alkaline-earth-metal atoms calculated using an accurate effective core potential”, *Phys. Rev. A* **69**, 042510 (2004).
- [86] E. Czuchaj, M. Krośnicki and H. Stoll: “Valence ab initio calculation of the potential energy curves for the  $\text{Sr}_2$  dimer”, *Chemical Physics Letters* **371** (3–4), 401 – 409 (2003).
- [87] S. Kotochigova: “Relativistic electronic structure of the  $\text{Sr}_2$  molecule”, *The Journal of Chemical Physics* **128** (2), 024303 (2008).
- [88] N. Boutassetta, A. R. Allouche and M. Aubert-Frécon: “Theoretical study of the electronic structure of the  $\text{Sr}_2$  molecule”, *Phys. Rev. A* **53**, 3845–3852 (1996).
- [89] M. Bishof, M. J. Martin, M. D. Swallows, C. Benko, Y. Lin, G. Quéméner, A. M. Rey and J. Ye: “Inelastic collisions and density-dependent excitation suppression in a  $^{87}\text{Sr}$  optical lattice clock”, *Phys. Rev. A* **84**, 052716 (2011).
- [90] D. Hansen and A. Hemmerich: “Observation of Multichannel Collisions of Cold Metastable Calcium Atoms”, *Phys. Rev. Lett.* **96**, 073003 (2006).
- [91] Y. Wang and M. Dolg: “Pseudopotential study of the ground and excited states of  $\text{Yb}_2$ ”, *Theoretical Chemistry Accounts* **100** (1), 124–133 (1998).

- 
- [92] A. Yamaguchi, S. Uetake, D. Hashimoto, J. M. Doyle and Y. Takahashi: “Inelastic Collisions in Optically Trapped Ultracold Metastable Ytterbium”, *Phys. Rev. Lett.* **101**, 233002 (2008).
- [93] R. Grimm, M. Weidemüller and Y. B. Ovchinnikov: “Optical dipole traps for neutral atoms”, arXiv preprint physics/9902072 (1999).
- [94] V. A. Dzuba and A. Derevianko: “Dynamic polarizabilities and related properties of clock states of the ytterbium atom”, *Journal of Physics B: Atomic, Molecular and Optical Physics* **43** (7), 074011 (2010).
- [95] Z. W. Barber, J. E. Stalnaker, N. D. Lemke, N. Poli, C. W. Oates, T. M. Fortier, S. A. Diddams, L. Hollberg, C. W. Hoyt, A. V. Taichenachev and V. I. Yudin: “Optical Lattice Induced Light Shifts in an Yb Atomic Clock”, *Phys. Rev. Lett.* **100**, 103002 (2008).
- [96] S. Dörscher, A. Thobe, B. Hundt, A. Kochanke, R. Le Targat, P. Windpassinger, C. Becker and K. Sengstock: “Creation of quantum-degenerate gases of ytterbium in a compact 2D-/3D-magneto-optical trap setup”, *Review of Scientific Instruments* **84** (4), 043109 (2013).
- [97] T. Pyragius: “Developing and building an absorption imaging system for Ultracold Atoms”, ArXiv e-prints (2012).
- [98] T. Sobottke: “Design und Realisierung eines hochauflösenden Detektionssystems für Ytterbium-Quantengase”, Bachelor Thesis (2014).
- [99] C. M. Sparrow: “On Spectroscopic Resolving Power”, *Astrophysical Journal* **44**, 76 (1916).
- [100] S. Fölling, A. Widera, T. Müller, F. Gerbier and I. Bloch: “Formation of Spatial Shell Structure in the Superfluid to Mott Insulator Transition”, *Phys. Rev. Lett.* **97**, 060403 (2006).
- [101] L. Viverit, C. Menotti, T. Calarco and A. Smerzi: “Efficient and Robust Initialization of a Qubit Register with Fermionic Atoms”, *Phys. Rev. Lett.* **93**, 110401 (2004).
- [102] A. J. Olson, R. J. Niffenegger and Y. P. Chen: “Optimizing the efficiency of evaporative cooling in optical dipole traps”, *Phys. Rev. A* **87**, 053613 (2013).
- [103] T. Fukuhara, Y. Takasu, M. Kumakura and Y. Takahashi: “Degenerate Fermi Gases of Ytterbium”, *Phys. Rev. Lett.* **98**, 030401 (2007).
- [104] B. DeMarco and D. S. Jin: “Onset of Fermi Degeneracy in a Trapped Atomic Gas”, *Science* **285** (5434), 1703–1706 (1999).

- [105] E. L. Surkov, J. T. M. Walraven and G. V. Shlyapnikov: “Collisionless motion and evaporative cooling of atoms in magnetic traps”, *Phys. Rev. A* **53**, 3403–3408 (1996).
- [106] P. W. H. Pinkse, A. Mosk, M. Weidemüller, M. W. Reynolds, T. W. Hijmans and J. T. M. Walraven: “One-dimensional evaporative cooling of magnetically trapped atomic hydrogen”, *Phys. Rev. A* **57**, 4747–4760 (1998).
- [107] C. J. Pethick and H. Smith: *Bose-Einstein condensation in dilute gases*, Cambridge university press (2002).
- [108] T. Sleator, T. Pfau, V. Balykin, O. Carnal and J. Mlynek: “Experimental demonstration of the optical Stern-Gerlach effect”, *Phys. Rev. Lett.* **68**, 1996–1999 (1992).
- [109] S. Stellmer, R. Grimm and F. Schreck: “Detection and manipulation of nuclear spin states in fermionic strontium”, *Phys. Rev. A* **84**, 043611 (2011).
- [110] S. Taie, R. Yamazaki, S. Sugawa and Y. Takahashi: “An SU(6) Mott insulator of an atomic Fermi gas realized by large-spin Pomeranchuk cooling”, *Nat Phys* **8** (11), 825–830 (2012).
- [111] M. Köhl, H. Moritz, T. Stöferle, K. Günter and T. Esslinger: “Fermionic Atoms in a Three Dimensional Optical Lattice: Observing Fermi Surfaces, Dynamics, and Interactions”, *Phys. Rev. Lett.* **94**, 080403 (2005).
- [112] I. Bloch: “Ultracold quantum gases in optical lattices”, *Nat Phys* **1** (1), 23–30 (2005).
- [113] J. Struck, C. Ölschläger, R. Le Targat, P. Soltan-Panahi, A. Eckardt, M. Lewenstein, P. Windpassinger and K. Sengstock: “Quantum Simulation of Frustrated Classical Magnetism in Triangular Optical Lattices”, *Science* **333** (6045), 996–999 (2011).
- [114] N. I. Petersen: “Aufbau und Charakterisierung eines optischen Dreiecksgitters für Ytterbium”, Master’s thesis, University of Hamburg (2014).
- [115] C. Becker: “Multi component Bose-Einstein condensates”, Ph.D. thesis, University of Hamburg (2008).
- [116] J. Eschner, G. Morigi, F. Schmidt-Kaler and R. Blatt: “Laser cooling of trapped ions”, *J. Opt. Soc. Am. B* **20** (5), 1003–1015 (2003).
- [117] J. Pu and H. Zhang: “Intensity distribution of Gaussian beams focused by a lens with spherical aberration”, *Optics Communications* **151** (4–6), 331 – 338 (1998).
- [118] T. A. Savard, K. M. O’Hara and J. E. Thomas: “Laser-noise-induced heating in far-off resonance optical traps”, *Phys. Rev. A* **56**, R1095–R1098 (1997).
- [119] C. Kollath, A. Iucci, I. P. McCulloch and T. Giamarchi: “Modulation spectroscopy with ultracold fermions in an optical lattice”, *Phys. Rev. A* **74**, 041604 (2006).

- 
- [120] B. Hundt: “Momentum-Resolved Optical Lattice Modulation Spectroscopy on Bose-Fermi Mixtures”, Master’s thesis, University of Hamburg (2011).
- [121] J. Heinze: “From higher bands to higher spins: Ultracold fermions in novel regimes”, Ph.D. thesis, University of Hamburg (2013).
- [122] D. Leibfried, R. Blatt, C. Monroe and D. Wineland: “Quantum dynamics of single trapped ions”, *Rev. Mod. Phys.* **75**, 281–324 (2003).
- [123] J. Silva-Valencia and A. M. C. Souza: “Entanglement of alkaline-earth-metal fermionic atoms confined in optical lattices”, *Phys. Rev. A* **85**, 033612 (2012).
- [124] M. Foss-Feig, M. Hermele, V. Gurarie and A. M. Rey: “Heavy fermions in an optical lattice”, *Phys. Rev. A* **82**, 053624 (2010).
- [125] N. V. Vitanov, T. Halfmann, B. W. Shore and K. Bergmann: “Laser-Induced Population Transfer by Adiabatic Passage Techniques”, *Annual Review of Physical Chemistry* **52** (1), 763–809 (2001), pMID: 11326080.
- [126] J. W. Cho, H.-g. Lee, S. Lee, J. Ahn, W.-K. Lee, D.-H. Yu, S. K. Lee and C. Y. Park: “Optical repumping of triplet- $P$  states enhances magneto-optical trapping of ytterbium atoms”, *Phys. Rev. A* **85**, 035401 (2012).
- [127] M. Notcutt, L.-S. Ma, J. Ye and J. L. Hall: “Simple and compact 1-Hz laser system via an improved mounting configuration of a reference cavity”, *Opt. Lett.* **30** (14), 1815–1817 (2005).
- [128] E. D. Black: “An introduction to Pound–Drever–Hall laser frequency stabilization”, *American Journal of Physics* **69** (1), 79–87 (2001).
- [129] B. W. Shore: “Coherent manipulations of atoms using laser light”, *Acta Phys. Slovaca* **58** (3), 243–486 (2008).
- [130] S. A. Malinovskaya: “Optimal coherence via adiabatic following”, *Optics Communications* **282** (17), 3527–3529 (2009).
- [131] L. Kouwenhoven and L. Glazman: “Revival of the Kondo effect”, *Physics world* **14** (1), 33 (2001).
- [132] H. Tsunetsugu, M. Sigrist and K. Ueda: “The ground-state phase diagram of the one-dimensional Kondo lattice model”, *Reviews of Modern Physics* **69** (3), 809 (1997).
- [133] C. Gardiner and P. Zoller: *Quantum noise: a handbook of Markovian and non-Markovian quantum stochastic methods with applications to quantum optics*, volume 56, Springer Science & Business Media (2004).



- [134] C. Gardiner and P. Zoller: *The Quantum World of Ultra-Cold Atoms and Light Book I: Foundations of Quantum Optics*, Imperial College Press (2014).
- [135] J. Simonet: “Optical traps for Ultracold Metastable Helium atoms.”, Ph.D. thesis, Université Pierre et Marie Curie, Paris (2011).
- [136] S. Murmann, A. Bergschneider, V. M. Klinkhamer, G. Zürn, T. Lompe and S. Jochim: “Two Fermions in a Double Well: Exploring a Fundamental Building Block of the Hubbard Model”, *Phys. Rev. Lett.* **114**, 080402 (2015).
- [137] S. K. Baur and E. J. Mueller: “Two-body recombination in a quantum-mechanical lattice gas: Entropy generation and probing of short-range magnetic correlations”, *Phys. Rev. A* **82**, 023626 (2010).



---

## Danksagung

Eine Promotion ist ohne einen großen Kreis an unterstützenden Menschen unmöglich. Ich möchte bei allen, die im Großen wie im Kleinen zum Gelingen dieser Arbeit beigetragen haben ganz herzlich bedanken und werde die Unterstützung, die ich durch euch erfahren habe, nicht vergessen. Ein paar Leute möchte ich im Folgenden besonders erwähnen.

Zuallererst möchte ich mich bei Klaus Sengstock bedanken. Deine Motivation, deine Unermüdlichkeit und nicht zuletzt das Vertrauen, welches Du mir entgegengebracht hast, war außergewöhnlich. Die Bedingungen, unter denen an ILP und ZOQ Forschung stattfinden kann, sind in großem Maße dein Verdienst und das beinhaltet insbesondere auch die Art und Weise, wie miteinander umgegangen wird.

Ganz besonders freue ich mich, mich bei Christoph Becker bedanken zu dürfen. Du hast mich seit meiner Diplomarbeit immer und in allen Situationen unterstützt und meinen Werdegang begleitet. Deine ehrliche und fröhliche Art, dein Engagement und deine Physik-Neugier war motivierend und inspirierend und nicht zuletzt der Grund für meine Promotion.

Meinen beiden "Junior"-Doktoranden, André Kochanke und Thomas Ponath, möchte ich von ganzem Herzen für die großartige Zeit, in und außerhalb des Instituts, danken. Durch eure entspannte und gleichzeitig engagierte Art, waren auch schwierige Situationen erträglich und ich kann gar nicht beginnen aufzuzählen, wofür ich euch sonst noch alles dankbar bin. Ohne meine Buddys hätte ich diese Promotion nicht abgeschlossen. Tausend Dank!

Zu großem Dank bin ich auch meinen beiden "Senior"-Doktoranden verpflichtet: Alexander Thobe und Sören Dörscher. Eure nette Aufnahme in das Team und eure unglaubliche Geduld in (wiederholter) Beantwortung jeder meiner Fragen waren bemerkenswert und haben meinen Einstieg in das Projekt erst ermöglicht.

Für das große Engagement und die tolle Stimmung möchte ich mich bei allen Master- und BachelorstudentenInnen bedanken: Benjamin Abeln, Anna Skottke, Niels Petersen, Torben Sobottke, Lukas Heinze und David Perconte. Ihr ward und seid eine Bereicherung für die gesamte Arbeitsgruppe und es war mir eine Freude mit euch zu arbeiten.

Ein großer Dank geht auch die gute Seele des Projekts: Janina Dahms. Du hast mich und uns in den vielen Jahren immer durch deine fröhliche, direkte Art unterstützt und uns daran erinnert, was eigentlich wichtig ist. Danke!

Nicht zuletzt möchte ich mich herzlichst bei der gesamten Forschungsgruppe Sengstock und allen MitarbeiterInnen des ILP und ZOQ bedanken. Ohne die engagierte, freundliche und hilfsbereite Zusammenarbeit aller Beteiligten wären diese beiden Institute nicht das was sie sind.

Ein Dank aus tiefstem Herzen geht an meine gesamte Familie und alle Freunde: ohne euch und eure Unterstützung wäre diese Arbeit nicht geschrieben worden. Danke!